Adaptive Power Control as a Fade Countermeasure
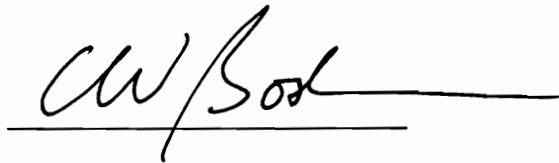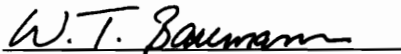## on Satellite Links

by

Dennis G. Sweeney

Dissertation submitted to the Faculty of the
Virginia Polytechnic Institute and State University
in partial fulfillment of the requirements for the degree of

Doctor of Philosophy

in

Electrical Engineering

APPROVED:

Dr. C. W. Bostian, Chairman

Dr. W. Baumann   Dr. G. Brown

Dr. W. Kohler   Dr. T. Pratt

January 1993
Blacksburg, Virginia

Adaptive Power Control as a Fade Countermeasure
on Satellite Links
by
Dennis G. Sweeney

(Abstract)

Satellite systems in the 20/30 GHz band are very susceptible to outages due to rain-induced fades. In order to reduce the impact of these fades, it has been proposed that the power of the uplink station transmitter be adjusted during the fade to compensate.

This dissertation will explore some of the issues involved in implementing this uplink power control (ULPC). Fade slope is examined as a parameter to predict signal strength during a fade. A fade slope model based on fade physics is presented, but it strongly suggests that fade slope is not an appropriate parameter for ULPC.

Real time scaling of attenuation from the downlink to the uplink shows more promise for ULPC. Differences in drop size distributions during a rain storm will result is different scaling factors. If the downlink attenuation is limited to 6 dB at 20 GHz, real time scaling can be accomplished. A scaling type ULPC algorithm driven by downlink attenuation is tested on 66 hours of OLYMPUS 20/30 GHz fade data. A similar algorithm driven by uplink attenuation is tested and the performance of the two algorithms is presented and compared.

Acknowledgements

I am particularly indebted to Dr. Charles W. Bostian. My association with him goes back to the early 1970's when he was a new Ph.D. and teacher. He encouraged my independent study and pressed the limits of my engineering knowledge. In the years after my undergraduate graduation, he was my continuing contact with Virginia Tech and was always eager to share his research projects. When the opportunity came to for me to return to graduate school, he found academic and financial support for me. He has given me education far beyond the classroom. He has gifted me with a wider view of engineering through his encouragement and support of publication and travel, and he has guided me in my own desire to be a teacher. He has been a mentor in the best sense of that word.

I would like to thank all the committee members. Dr. Pratt directed my Masters work and shared his keen insight into the right questions to ask and the clearest way to present them. Dr. Brown gave me the perspective of electromagnetics and a good experimental mind. Dr. Kohler was my voice of the larger university and generously helped me with the mathematical problems I encountered along the way. Dr. Baumann guided me through the world of parameter identification and gave me a new perspective on the adaptive control problem.

I would also like to thank Dr. W. L. Stutzman and Dr. J. C. McKeeman who managed the OLYMPUS and ACTS programs. Dr. Stutzman was one of my first teachers, and no I didn't waste my life as he once feared! Thanks also go to Dr. W. Stephenson and the Electrical Engineering department for supporting my desire to teach.

Many thanks to those of the Satellite Communications Group: fellow graduate students, engineering, and support staff. You have been a lot of fun and a lot of help. Thanks to all of you who helped me steer my way through late night exams, computer glitches, and all night rainstorms!

Finally, I would like to thank my parents who encouraged my early interest in electrical and mechanical gizmos: my mother who tolerated me when I learned how to take things apart long before I could put them back together again, and my father who taught me that engineering is a process of thought, not just a body of knowledge. And, I would like to thank all those radio amateurs who introduced me to the wonderful world of radio.

TABLE OF CONTENTS

LIST OF FIGURES

LIST OF TABLES

CHAPTER 1: INTRODUCTION

1.1 SATELLITE SYSTEMS

1.1.1 Satellite Systems and the Need for Fade Countermeasures

At the present time, the bulk of commercial satellite traffic is carried in the 6/4 GHz satellite allocation. The need for greater capacity has pushed satellite system designers to go to the 14/12 GHz allocation and there is an additional, but largely unused, allocation at 30/20 GHz. These two allocations together offer 3000 MHz of bandwidth and freedom from terrestrial interference sources since the 14/12 GHz and the 30/20 GHz allocations are not shared with terrestrial microwave systems. Two major experimental programs to explore the potential of 30/20 GHz are under way. One is the OLYMPUS program sponsored by the European Space Agency (ESA) [1][2] and the other is the Advanced Communications Technology Satellite (ACTS) which is supported by NASA [3]. There is also a 20/30 GHz research effort involving the ITALSAT F1.

Unfortunately a major drawback to the use of these higher frequencies is rain attenuation. At 6/4 GHz, the effects of rain attenuation are small and can be easily overcome by built in system margins. However, the additional transmitter power required to operate a 14/12 GHz or 30/20 GHz system with a fixed margin is prohibitively large. Figure 1.1-1 shows a typical rain fade measured on the OLYMPUS - Blacksburg, VA, USA path at 12.5, 20 and 30 GHz. It is clear that the fading problem becomes more severe as the frequency increases.

1.1.2 VSAT's and Small Margin Terminals

The problem of rain induced fades can be overcome with site diversity, but site diversity is expensive since it requires two complete earth stations and a link to connect them together. Site diversity also makes Very Small Aperture Terminals (VSATs) less attractive since the VSAT concept utilizes a small

1

inexpensive earth terminal which can be placed almost anywhere. The simplicity and small size of VSAT systems means that they are low margin systems. Fixed margins of 3 dB are envisioned. This makes them even more susceptible to rain fades.

12, 20, and 30 GHz Attenuation
Nov. 5,6, 1990 2300 − 0200 UT 10 sec Avg
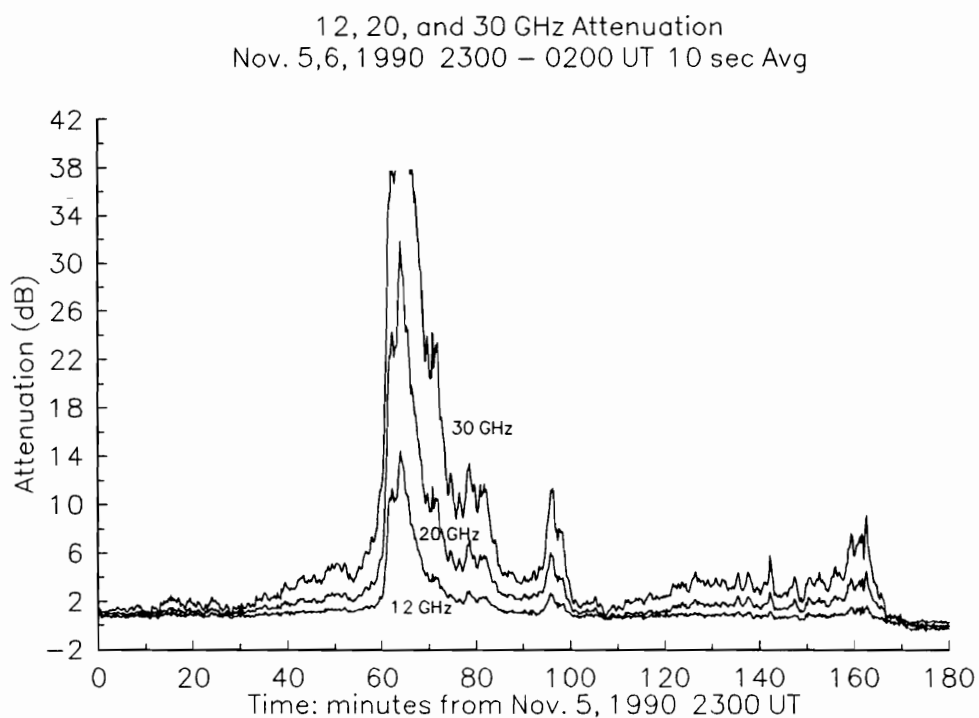
Figure 1.1-1: Fade measured on the OLYMPUS - Blacksburg link on November 5-6 1990 at 12.5, 20 and 30 GHz.

1.2 ADAPTIVE CONTROL AS A FADE COUNTER MEASURE

1.2.1 Allocating System Resources

Even if it were possible to supply the necessary fixed margin, it would be unneeded during the majority of the satellite's lifetime. The extra margin would only be needed a few hours a year during deep fades. It is highly desirable from a system stand point to allocate resources, such as transmitter power, only to those stations which have an immediate need to overcome a fade and only for as long as that need exists.

Some kind of adaptive control could allocate system resources on a need basis.

1.2.2 Different Types of Adaptive Control

A number of adaptive techniques have been suggested to deal with this problem. They fall into two major categories, the first being some kind of adaptive power control such as an AGC loop. This power control could be applied to the uplink, the downlink, or both. A second type of fade countermeasure is resource sharing such as time reserved in a TDMA frame, or data rate adjustments which change the energy per bit. A third type of adaptive control would switch to a lower frequency channel which is unfaded. These channels would be held in reserve in the event that the higher frequency channel experiences a debilitating fade. The lower frequency allocations are already heavily loaded and terminals to exploit this frequency diversity are complex. Such a system is unattractive.

This research is primarily concerned with adaptive power control as a fade countermeasure. Ince [4] was one of the first to propose adaptive power control as a fade countermeasure. He simulated three types systems: constant terminal power (CTP) which has no adaptive control, constant satellite power sharing (CSP), and adaptive satellite power sharing (ASP). Ince described ASP for two different types of satellite systems, one with a hard limiting transponder and another with a linear transponder.

3

With constant terminal power (CTP), each terminal is allocated a power level which does not change. This is fixed margin system. In the constant satellite power sharing (CSP) case, each terminal is adjusted so that the received power at the satellite is constant. This is uplink power control (ULPC) and it can counteract uplink fades only. With adaptive satellite power sharing (ASP), the ground terminal power is adjusted so that some system parameter such as signal to noise ratio or bit error rate is held constant. ASP is a combination of ULPC and downlink power control (DLPC) because the ground terminal can be adjusted to change its share of the satellite power. In a hard limiting system with multiple users, ASP is a complex task.

1.3 RESEARCH PROGRAM OUTLINE

While the Ince paper suggests that the concept of power control as a fade countermeasure has been contemplated for some time, the implementation of power control has been slower in coming. The function of this dissertation is to explore some of the questions that must be addressed in order to implement a power control scheme. Particular attention will be paid to constant satellite power sharing or ULPC because it is currently being considered for VSAT applications.

Chapter 1 of this dissertation is a brief introduction to the concept of adaptive power control and a brief overview of the OLYMPUS experiment at Virginia Tech. The OLYMPUS experiment is important because simultaneously recorded 20 and 30 GHz beacon signal strength data from OLYMPUS will be used to test the power control algorithms presented. Chapter 2 catalogs and evaluates the known power control algorithms and experiments. The majority of what has been reported involves CSP or uplink power control. This is understandable because the uplink is generally higher in frequency than downlink and thus more fade prone. In addition, the uplink can be controlled entirely by the ground station without intervention from the satellite's central control system if CSP type control is implemented. This simplicity is attractive for use with VSAT systems.

4

Chapter 3 will explore fade slope as a parameter that might be useful in driving a power control algorithm. Fade slope is evaluated by calculating the rate at which the First Fresnel zone volume fills with rain. Attenuation is related to how much water is in the volume, and fade slope is determined by rate at which the volume fills with water. The work described in Chapter 3 suggests that fade slope will not be useful for a power control scheme; nevertheless it is useful for understanding fade dynamics and the work presented here appears to be the first attempt to define an analytic basis for fade slope [5].

Chapter 4 investigates real time frequency scaling of attenuation, and it presents two ULPC schemes which employ frequency scaling. One scheme scales attenuation at the downlink to estimate or predict uplink attenuation, and the other utilizes an uplink beacon to predict uplink attenuation. The limits on dynamic control range are explored, and the two ULPC schemes are applied to a number of selected fade events measured at 20 and 30 GHz on the Blacksburg to OLYMPUS path. The performance of each algorithm is evaluated, and the two schemes are compared.

The uplink beacon scheme has seen renewed interest and a frequency allocation for such beacons was made at WARC-92 [6]. The work described in Chapter 4 shows that uplink beacon driven ULPC offers higher performance than ULPC driven from scaled downlink attenuation. Of course such a scheme requires an additional receiver at 30 GHz and the cost of this receiver must be weighed against the improved performance.

Chapter 5 describes some directions for additional research such as radiometer driven power control. Non-linear frequency scaling and neural net control is also investigated. Chapter 5 outlines some possibilities for additional experiment programs.

1.4 OLYMPUS EXPERIMENT

The launch of the ESA OLYMPUS satellite in July of 1989 offered an opportunity to collect data which would permit testing of power control algorithms on fade data measured at 20 and 30 GHz. In addition to 30/20 GHz transponders, OLYMPUS carries beacons at nominally 12.5 GHz (12.502 GHz), 20 GHz (19.771 GHz) and 30 GHz (29.656 GHz) [1]. As viewed from the equator the 12.5 and 30 GHz beacons are vertically polarized. The 20 GHz beacon is polarization switched between horizontal and vertical at 933 Hz. All three beacons are derived from a common master oscillator. This unique feature permits phase or frequency locking to the less fade prone 12.5 GHz beacon and synchronously detecting the 20 and 30 GHz beacon signals.

In August of 1990, the Satellite Communications Group at Virginia Tech began an experiment program which exploits the unique beacon frequency relationship to simultaneously measure the signal strength of the 12.5, 20, and 30 GHz OLYMPUS beacons at Blacksburg, VA, USA [7][8][9]. As viewed from Blacksburg, OLYMPUS is seen at an elevation angle of 14.5°.

This experiment is intended to produce attenuation statistics for 12.5, 20, and 30 GHz on the path, and to investigate frequency scaling, fade slope, and duration. A study of short baseline (< 100 m) diversity at 20 and 30 GHz is also included. The work presented here is part of the OLYMPUS experiment program.

The Virginia Tech earth station consists of four receiving terminals. The 20 and 30 GHz terminals have 1.5 m (5 ft) and 1.2 m (4 ft) antennas, respectively. The 12.5 GHz terminal uses a 3.6 m (12 ft) antenna. All the antennas are prime focus paraboloids. The 20 and 30 GHz terminals have VSAT sized antennas. A second 20/30 GHz terminal is part of a short base line diversity experiment. Figure 1.4-1 is a block diagram of the system.

The 12.5 GHz receiver can measure a fade up to 18 dB. Beyond this point it looses frequency lock. Because of the frequency lock at 12.5 GHz and the beacon frequency relationship, the 20 and 30 GHz receivers can measure down to their
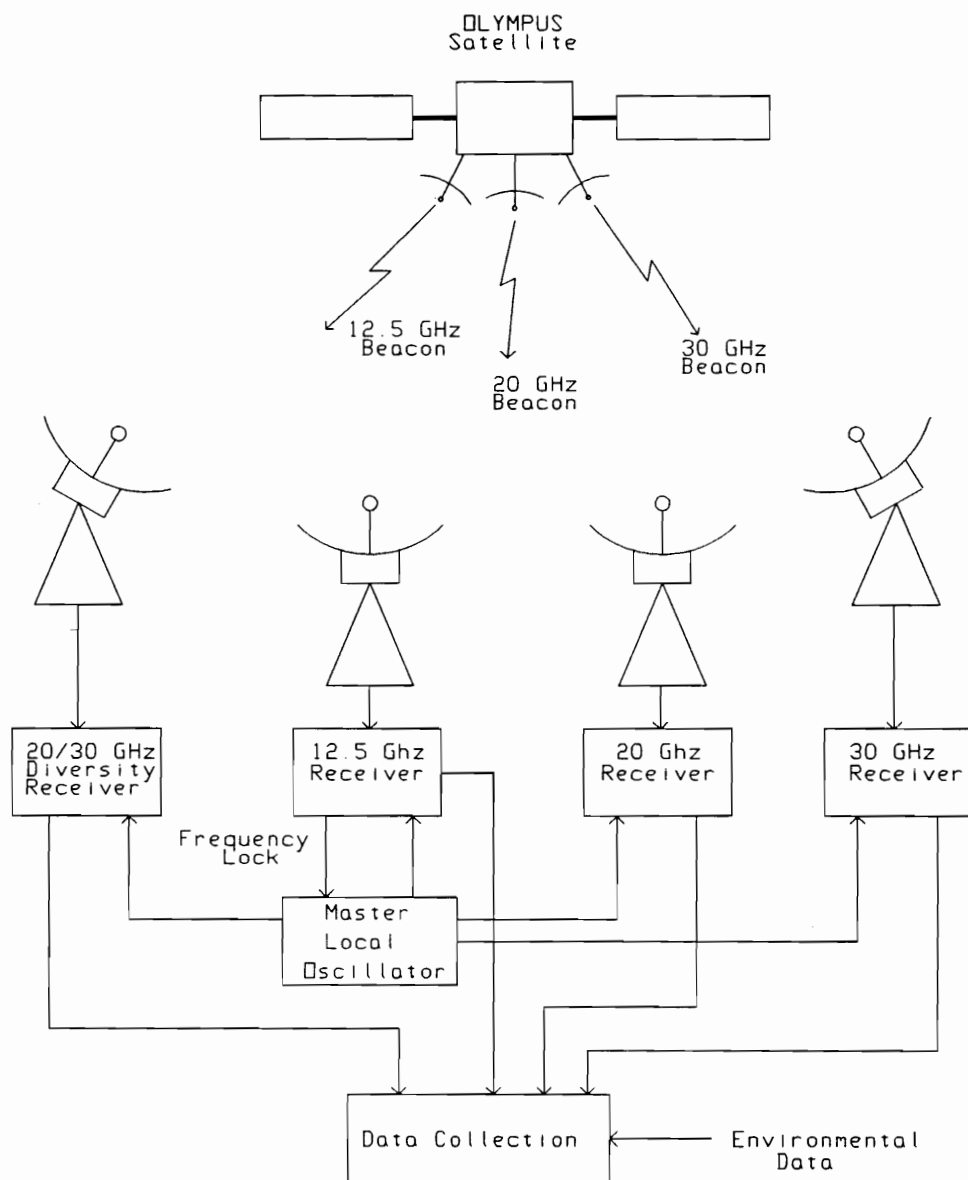
Figure 1.4-1: Block diagram of Virginia Tech OLYMPUS experiment.

respective noise floors. They can measure a fade of 38-40 dB. Each receiver has a measurement resolution of 0.05 dB. [10] The signal strength output from each beacon receiver is passed through a 3 Hz lowpass filter and result is sampled and recorded at a 10 samples per second rate.

The 3 Hz lowpass filter sets the ultimate receiver noise bandwidth and it insures the the Nyquist sampling criterion is met for the data sampling. Environmental data such as air temperature and wind speed and direction are also recorded.

1.5 REFERENCES

[1] OLYMPUS Users Guide: UG-6-1 Part 1: Propagation Package, European Space Research and Technology Center, Noordwijk, Netherlands, Issue 3, March, 1989.

[2] Dinwiddy, S.E., Ed, L-Sat Users Guide: UG-6-1 Part 4: 20/30 GHz Communications Package, European Space Research and Technology Center, Noordwijk, Netherlands, Issue 23, July, 1983.

[3] Lowry, Peter A., System Handbook: Advanced Communications Technology Satellite, NASA Lewis Research Center, Cleveland, Ohio, NASA document number TM-101460.

[4] Ince, A. N., D. W. Brown, and J. A. Midgley, "Power Control Algorithms for Satellite Communications Systems," IEEE Transactions on Communications, COM-24, Feb. 1976, pp. 267-275.

[5] Sweeney, Dennis G. and Charles W. Bostian, "The Dynamics of Rain-Induced Fades," IEEE Transactions on Antennas and Propagation, Vol. 40, No. 3, March 1992, pp. 275-278.

[6]   Flock, W. L. and E. K. Smith, "WARC 92 and Some Thoughts as to its Impact on the NASA Propagation Program," and A. O. Heyward, "Allocations by the 1992 World Administrative Radio Conference," Proceedings of the Sixteen NASA Propagation Experimenters Meeting (NAPEX XVI) and the Advanced Communications Technology Satellite (ACTS) Propagation Studies Miniworkshop, Houston, Texas, May 29-30, 1992, pp. 116-131.

[7]   Bostian, C.W., W.L. Stutzman, T. Pratt, J.C. McKeeman, and T.S. Rappaport, "Communications and Propagation Experiments for the OLYMPUS and ACTS Satellites," Proceedings of the International Communications Conference (ICC89), Boston, Mass, June 1989, pp. 1578-1581.

[8]   Davarian, F. and T. Pratt, "OLYMPUS Propagation and Communications Experiments in the U.S.," Proceedings of the OLYMPUS Utilization Conference, Vienna, Austria, April 12-15, 1989.

[9]   Pratt, T., W. Stutzman, J. McKeeman, C. Bostian, "Propagation Experiments with the OLYMPUS Satellite," Proceedings of the IEEE Global Telecommunications Conference (GLOBCOM), San Diego, CA, December 2-5, 1990, pp. 302.4.1-302.4.3.

[10] Stutzman Warren L., et al., "Communications and Propagation Experiment Using the OLYMPUS Spacecraft: Report on the First Year of Data Collection," Virginia Tech Report EESATCOM 91-4, JPL Contract #958435, October 1991, p. 34.

CHAPTER 2: REPORTED POWER CONTROL EXPERIMENTS AND ALGORITHMS

2.1 JAPANESE TESTS

2.1.1 BSE Open-Loop Power Control Experiment

One of the earliest unlink power control (ULPC) tests was reported by Yamamoto [1] in 1982. It was an open loop system implemented on the Japanese Broadcasting Satellite for Experimental Purposes (BSE). Figure 2.1-1 is a block diagram of the system.
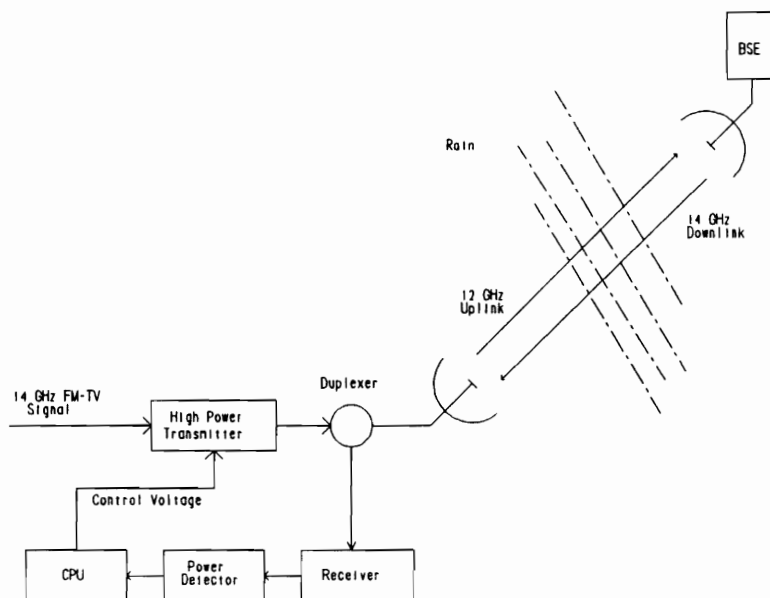
Figure 2.1-1: Block Diagram of ULPC system used by Yamamoto [1].

The output power of the BSE satellite was kept constant by an automatic level controller on board the satellite and fades were measured on the 12 GHz downlink. Thus any change in the 12 GHz downlink signal strength could be attributed to a fade. The resulting downlink attenuation was used to predict the uplink attenuation, $y(nT + \triangle)$, according to the algorithm:

$$y(nT + \triangle) = (A)\ f[X(nT), X((n-1)T),\ ...\ , X((n-k+1)T)] \qquad (2.1\text{-}1)$$

where

$A = (F_u/F_d)^{1.7}$: F_u and F_d are the up and downlink frequencies, respectively.

T: sampling interval.

$\triangle$: time delay due to control operation.

$X(iT)$: sampled value of downlink attenuation in dB at time iT.

$f[\cdot]$: downlink attenuation in dB at $(nT + \triangle)$ estimated by the least squares method with a quadratic function of time.

k: number of sampled data values $X(iT)$ used for the least squares fit.

For the reported experiment, $T = 1$ sec., $k = 10$, $\triangle = 0.3$ sec., and $A =$ 1.4. The output power of the uplink transmitter was only adjusted every two seconds because of data transfer limitations in the control unit. The uplink signal strength at the satellite was telemetered back to the ground for analysis. The uplink signal strength at the satellite should remain constant if the ULPC system worked properly.

Yamamoto claims that he was able to maintain the uplink signal strength constant within 0.5 dB RMS and 1.5 dB peak for fades up to 14 dB. He reports that the errors in control were due to variations in the frequency scaling ratio and to the slowness of his control system because it made a correction only every 2 seconds. He also observed scintillations due to atmospheric turbulence up to 2.3 dB peak to peak on the uplink. Yamamoto's system was too slow to collect for these scintillations.

2.1.2 CS (SAKURA) Satellite Open Loop Test

Open loop tests were done on the 30/20 GHz Japanese CS satellite by Kosaka [2]. CS was launched in December 1977 by the Japanese Ministry of Post and Telecommunications with the help of Nippon Telegraph and Telephone Public Corporation (NTT). CS was designed as a test satellite to serve Japanese domestic telecommunication needs and it is notable because it was the first satellite to carry 30/20 GHz transponders.

These tests scaled the downlink attenuation by a factor of 2 in order to obtain an estimate for uplink attenuation. Kosaka noted that the actual scaling value varied from the chosen factor of 2. This resulted in control errors, but no numerical measure of error was reported.

The open loop power control experiments were part of a larger test program which investigated a number of fade countermeasures: uplink power control using both open loop and closed loop techniques, up/downlink power control, site diversity, and frequency band switching. The test program ended late in 1985.

2.1.3 CS satellite Closed Loop Tests

Closed loop tests were conducted by Egami [3][4] on the CS satellite. Figure 2.1-2 shows Egami's closed loop power control system. Station A transmits to station B which monitors the link quality, in this case carrier to noise ratio (C/N). Bit error rate (BER) could be monitored in a digital system. The measured value of C/N is telemetered back to station A via the satellite's telemetry path shown in Figure 2.1-2. This value of C/N is compared with the desired C/N. If it greater than the desired, the uplink transmitter power is reduced, or if is less than the desired, the transmitter power is increased. In practice, the integral of the difference is used. This assures that the transmitting power converges to a steady state value from any initial value:

$$p_A = -K_1 \int_t (C/N_{A \rightarrow B} - C/N_{req})d\tau + p_o \qquad (2.1\text{-}2)$$

where

p_A: station A's transmitter power t: time

$C/N_{A \rightarrow B}$: C/N measured on the A to B path C/N_{req}: C/N required

K_1: loop gain p_o: constant

Notice that at steady state the system will operate with the minimum power necessary to maintain the desired C/N. In a multiple access system, each user is essentially operating with zero margin. With an uplink fade, the earth station transmitter is increased so that the received power at the satellite is equal to the received power under clear air conditions. The satellite transmit power is unaffected.

A downlink fade can also be compensated for with an increase in earth station power. In this case the increase in earth station power produces an increase in the satellite transmitter power allocated to that user. Since all the other users are operating with zero margin, some of the extra margin in the system is now allocated to the station experiencing the fade. The extra margin in the system is a power pool that is made available to those stations which need assistance in overcoming a fade. Variations in received C/N less than 0.3 dB for fades up to 9 dB were reported [4] with this system.

It was assumed that the variations in the link attenuation did not have high frequency components greater than the reciprocal of the round trip delay time of 0.3 sec. Without some type of band limiting, the system maybe unstable. The potential for instability is one of the disadvantages of a closed loop system. The integration described in (2.1-2) was used to band limit the system. Egami reports using a 5 second integration time [4].
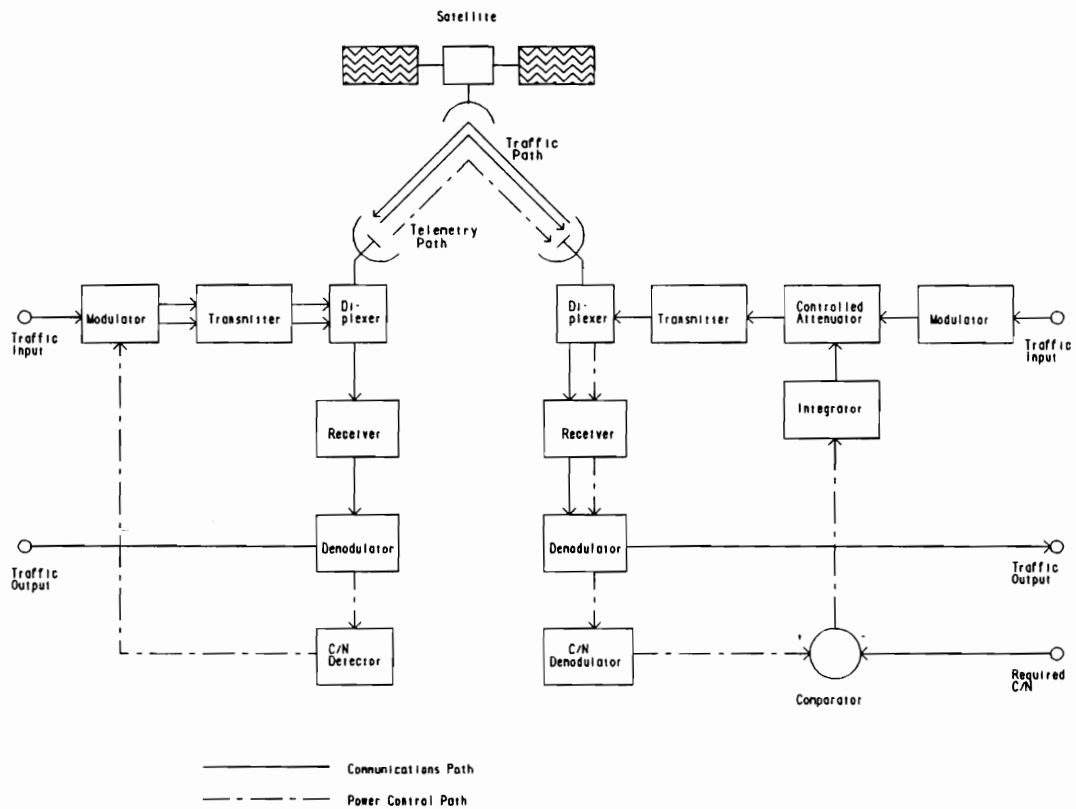
Figure 2.1-2: Closed loop adaptive control system used by Egami [3].

2.2 COMSAT EXPERIMENT

2.2.1 Description of Comsat Experiment

Comsat conducted extensive experiments with ULPC during the winter of 1986/1987 and during the late summer of 1987 at their Clarksburg, Maryland laboratories [5]. These experiments were conducted at 14/11 GHz on the INTELSAT-V (F-3) satellite located at 307° E longitude. The antenna elevation angle from Clarksburg to the satellite was 38.1°.

The winter '86/'87 series of experiments utilized a loop-back scheme. Figure 2.2-1 is a simplified block diagram of this system. A pilot tone was uplinked to the satellite at 14 GHz and it was looped-back through the satellite transponder to the same ground station on the 11 GHz downlink. In addition, the satellite carried an 11.2 GHz downlink beacon. Downlink attenuation was obtained from the signal strength of this beacon and the ULPC controller scaled the downlink attenuation to the uplink. This estimate of uplink attenuation was used to adjust the uplink pilot transmitter AGC amplifier in Figure 2.2-1 to compensate for the uplink fade. The same 4.5 meter antenna was used for all three signals.

The receiver gains were set so that the beacon receiver and the loop-back receiver outputs were equal during clear sky conditions. If the fade compensation was correct, there would be no change in the relative beacon and the loop-back pilot receiver outputs. This is due to the fact that the pilot and the beacon on the downlink experience the same attenuation. Any relative difference in the receiver outputs would represent an error in control. The system was real time, analog, and there were no thresholds for system engagement.

This system was capable of quite impressive performance as can be seen in Figure 2.2-2. Comsat reported all their results in graphical form and no data were given for RMS or peak error.
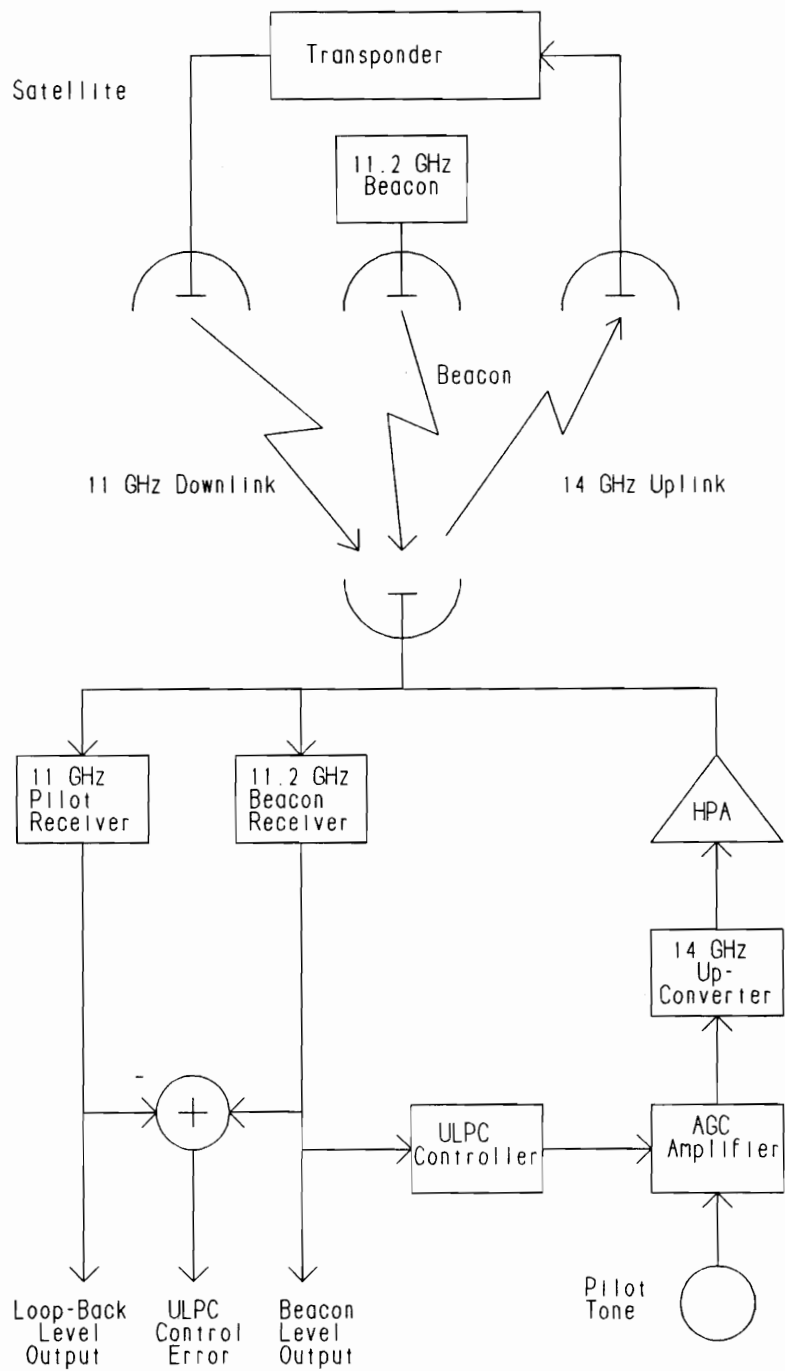
Figure 2.2-1: Simplified block diagram of Comsat loop-back ULPC scheme [5].
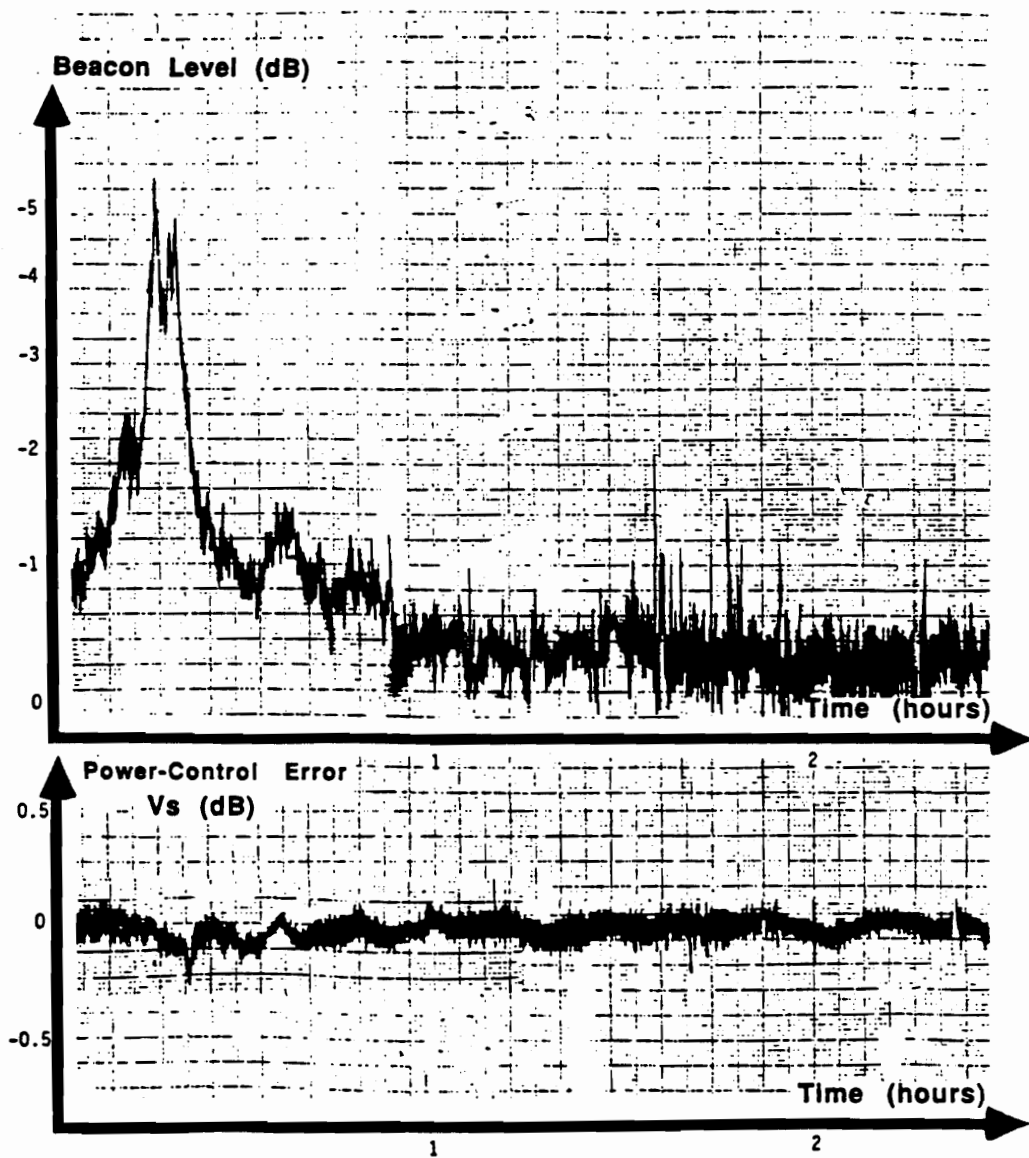
Figure 2.2-2: Loop-back ULPC system response during a high rain rate event as recorded on December 21, 1986 [5].

The summer 1987 tests employed the same satellite in a cross-strapped configuration. Pilot tones were uplinked at 14 GHz, cross-strapped to 4 GHz and then downlinked. The effect of attenuation and diurnal variations on the 4 GHz downlink was estimated to be less than 0.5 dB and so they were ignored. Any change in the 4 GHz downlink could then be directly attributed to a 14 GHz uplink fade. As in the loop-back system, attenuation on the 11.2 GHz downlink beacon was scaled to control one of the 14 GHz uplink tones. In addition, a 14 GHz radiometer measured sky temperature and estimated uplink attenuation. This radiometer estimate of uplink attenuation controlled a second 14 GHz uplink pilot tone. If the control system correctly compensated for the uplink fade, the cross-strapped downlink signal would remain constant. Figure 2.2-3 is a simplified block diagram of this system. Figure 2.2-4 is an example of beacon driven ULPC for the cross-strapped system.

The 11.2 GHz beacon receiver and the 14 GHz uplink shared a common 4.5 meter antenna; however the radiometer was located 27 meters away and it used a 1.6 meter antenna. Due to the different antenna size and location, the radiometer did not "see" the same volume as the uplink antenna and there was no assurance that the radiometer "looked" exactly at the satellite.

2.2.2 Real Time Frequency Scaling of Attenuation in the Comsat Experiment

Comsat used a frequency scaling factor of 1.5. This is slightly less than the statistical scaling factor of f^2 which yields 1.62. Comsat investigated the actual real time scale factor, and their measurements show a decease in the scaling factor as attenuation increased. They also noticed a nonlinear retrace at the beginning and end of some events. One such event is shown in Figure 2.2-5.

The Comsat investigators observed that these phenomena were possibly due to differences in drop size distributions but they did not pursue this insight. In addition they noted large variations in the scale factor at attenuations less then 1 dB. This is consistent with Allnutt [6]. Comsat concluded that the power control errors due to a change in the scaling factor would be minimal and they could be ignored. Comsat plotted the scaling factor verses attenuation for small

drops, average rain, and thunderstorm rain using the technique in [7] and [8]. They concluded that the scale factor for average rain was approximately 1.65 which is very close to the f^2 factor of 1.62.

Comsat considered the effects of other sources of attenuation, specifically gaseous attenuation and scintillations. The results of their investigation are shown in Table 2.2-1 below.

Comsat finally settled on scale factor of 1.5 for the actual experiment. The gaseous attenuation scaled by this factor and it was very close to the scaling factor for rain.

Table 2.2-1: Attenuations at 14/11 GHz considered in the Comsat ULPC experiment [5].

Attenuation Type	Normal Magnitude (dB) (20° El)	Freq Dependence of 14/11 GHz Ratio	Fading Dynamics	Fade Duration
Gaseous	0.1-0.5	Variable [≈ 1.5]	-	-
Scintillation	≤ 2	$f^{7/12}$ [≈ 1.15]	Spectrum: ≤ 0.3 Hz	≤ 1.5 s for 1 dB fade
Rain/Cloud	0-30+	$\approx f^2$ [≈ 1.6]	Rate: ≤ 0.2dB/s	1 - 20 minutes @ 5 dB fade

Figure 2.2-3: Simplified block diagram of cross-strap system [5].
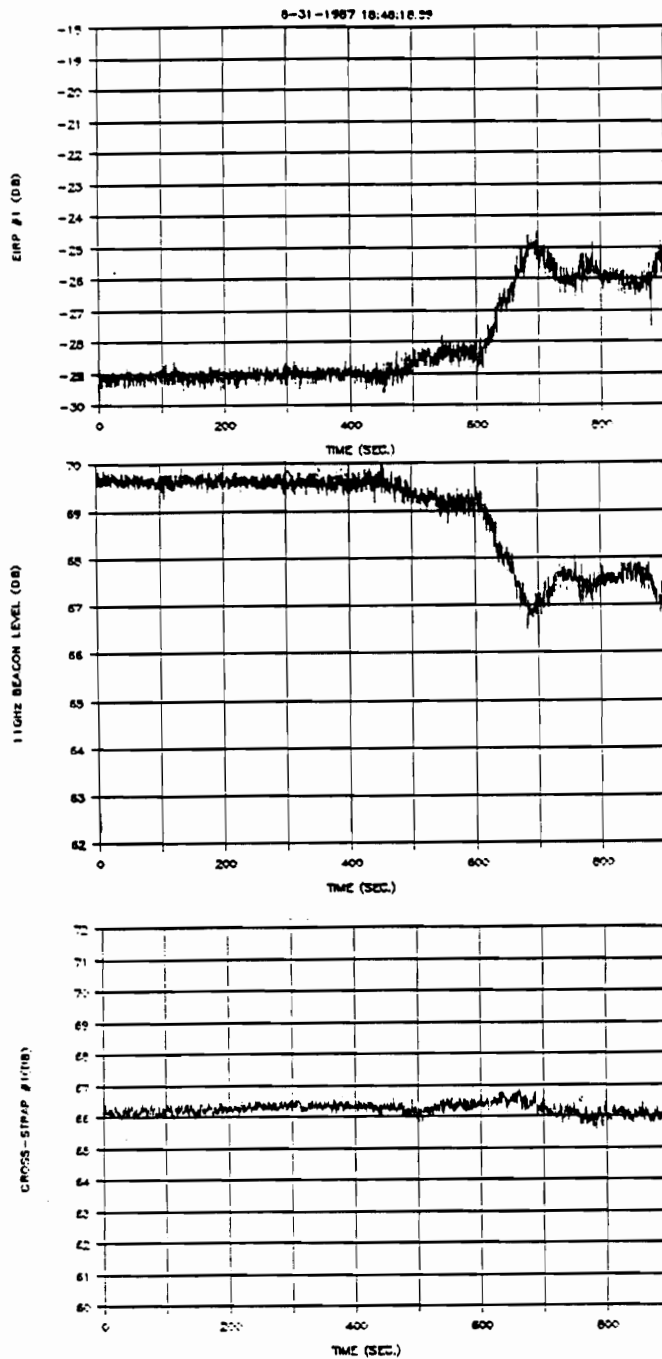
Figure 2.2-4: Performance of Comsat cross-strapped system. Cross-strap #1 is the received signal at the satellite. It should remain constant due to ULPC. EIRP #1 is the pilot tone transmitter power and the 11 GHz beacon level is received signal strength during the fade [5].
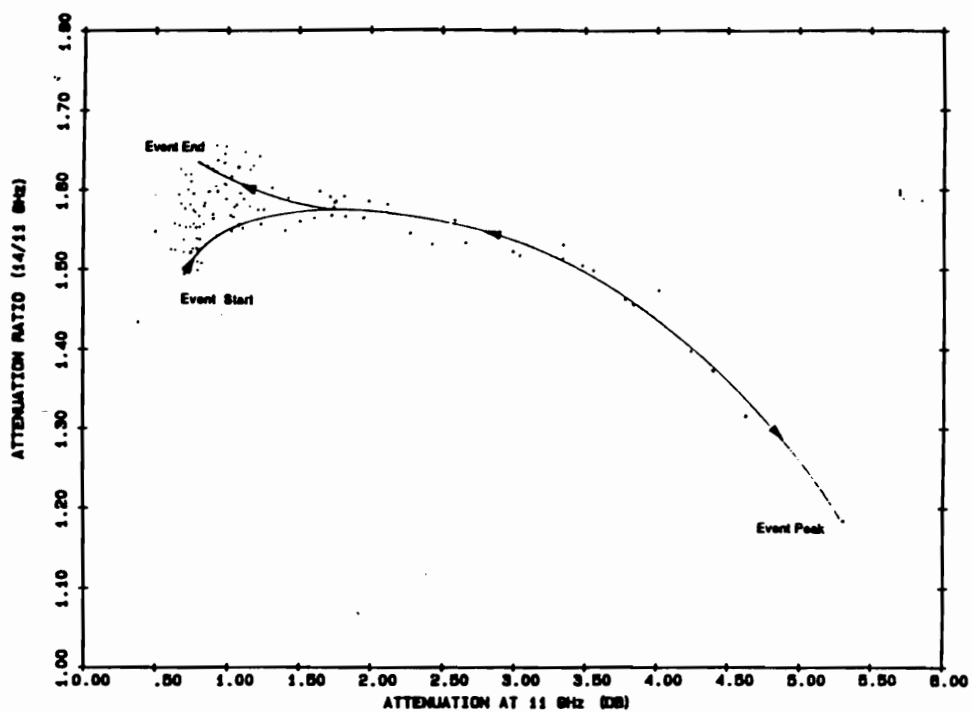
Figure 2.2-5: 14/11 GHz scale factor plotted versus 11 GHz attenuation for the event in December 21, 1986 event in Figure 2.2-2 [5].

22

2.2.3 Performance of the Comsat Experiments

Comsat concluded that the loop-back system could compensate fades up to approximately 7.5 dB with errors less than ±0.5 dB. In addition the beacon monitoring cross-strap system worked well, generally compensating for fades with RMS errors less than 1 dB. They also found that their pilot driven systems could follow scintillations.

The radiometer controlled system did not perform as well as the pilot controlled systems. Comsat speculated that differences in antenna pointing and observed volume between the radiometer and the satellite ground station antennas was the reason.

Their data showed that the average fade scaling factor was approximately 1.6, very close to the f^2 ratio of 1.62. They also concluded that the scaling ratio of 1.5 that was actually used did not introduce significant error over the 7.5 dB control range implemented in their experiments.

2.2.4 Continuing Comsat Work

Subsequent work by Comsat has refined their algorithm [9]. Since fades occur for only a small percentage of a year, Comsat claims that it is possible to automatically set the clear sky reference level with reasonable accuracy. They assumed that changes in the reference clear sky level will occur much more slowly than propagation induced changes. However, cloud and water vapor attenuation cannot easily be distinguished from changes in the clear sky signal level, but Comsat assumed that at Ku-band frequencies these effects were small enough to ignore.

The mean and the standard deviation of the measured downlink beacon level are used to set the clear sky level. If these two quantities are within pre-set limits, clear sky is assumed. For rain events that last for more than a few hours, the base line level from the previous day is used to correct the clear sky reference. The clear sky level is subtracted from the measured beacon level and what

remains are the propagation impairments. Figure 2.2-6 is a block diagram of Comsat's improved algorithm.

Tropospheric scintillation is separated from the fade by a 20 second running average filter. Comsat assumed that the scintillations are largely symmetric about the mean level and that the scintillation spectrum is limited to frequencies below 2 Hz. The 20 second running average filter introduces a 10 second delay so a predictor similar to the baseline predictor is used to obtain the rain fade level. This predictor uses 30 samples spanning a period of 10 minutes.

Comsat now separates the rain fade from the scintillations. The rain fade on the down link, A_{dR}, is scaled to obtain the uplink attenuation, A_{uR}:

$$A_{uR} = A_{dR}(f_u/f_d)^2 \quad \text{(dB)} \tag{2.2-1}$$

where f_u and f_d are the up and downlink frequencies, respectively. The scintillations are scaled by:

$$S_u = S_d(f_u/f_d)^{7/12} \quad \text{(dB)} \tag{2.2-2}$$

were S_u and S_d are the scintillation levels at the up and downlink frequencies. The estimated uplink attenuation, L_u, is obtained by adding the scaled uplink attenuation due to rain and the scaled uplink scintillations:

$$L_u = A_{uR} + S_u \quad \text{(dB)} \tag{2.2-3}$$

Figure 2.2-7 shows the process of separating the fade event into rain fade and scintillations. Figure 2.2-8 is a plot of an uplink fade and the power control error using this system. Comsat reports that the control accuracy is better the ± 2 dB for this 17 dB fade with significant scintillation.
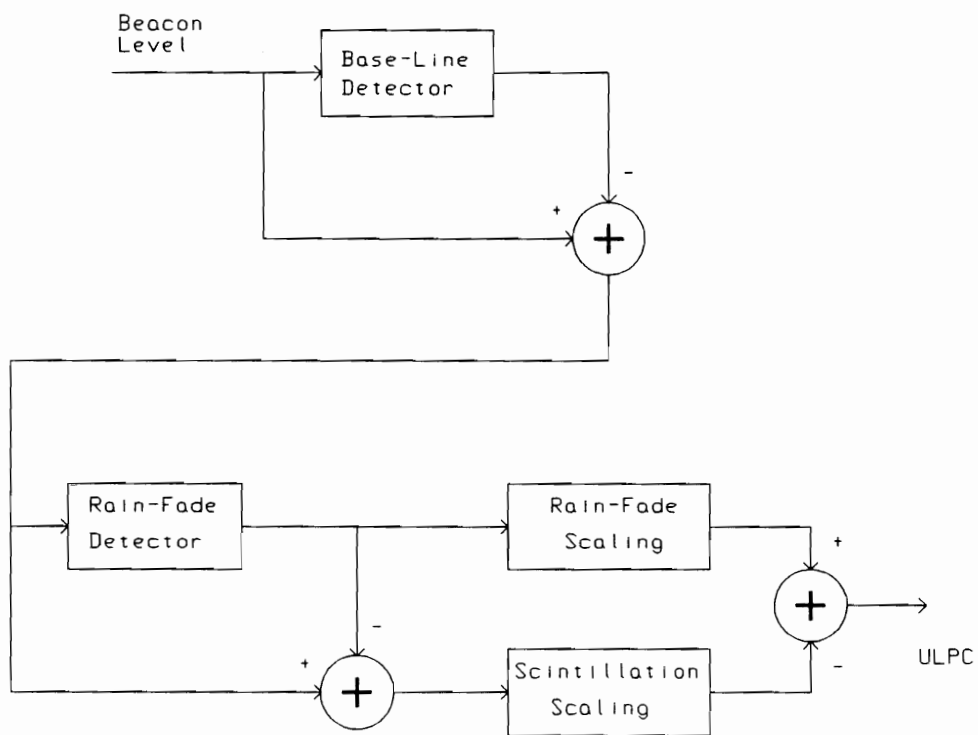
Figure 2.2-6: Comsat ULPC algorithm [9].
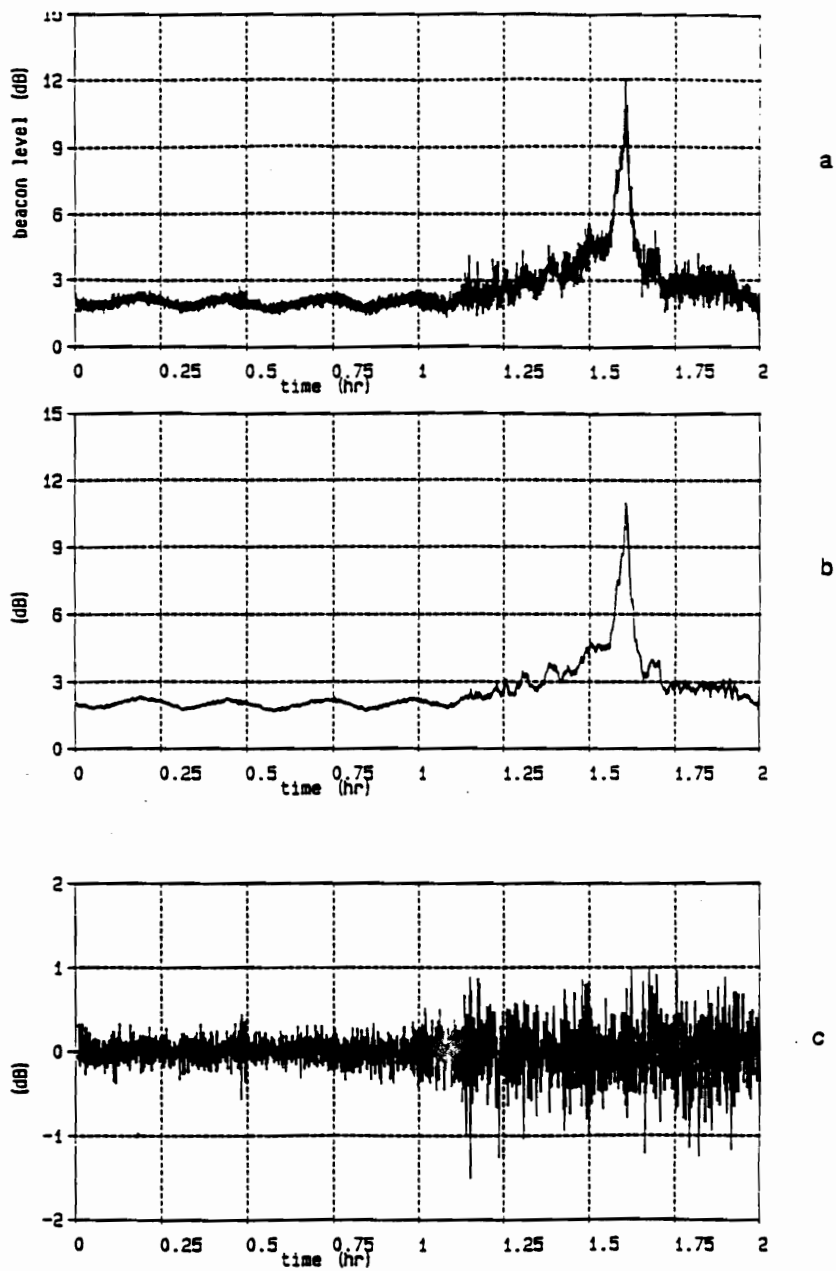
Figure 2.2-7: Separation of beacon level into rain fade and scintillations.
a. beacon level, b. rain fade, c. scintillations (a-b). No event date given [9].
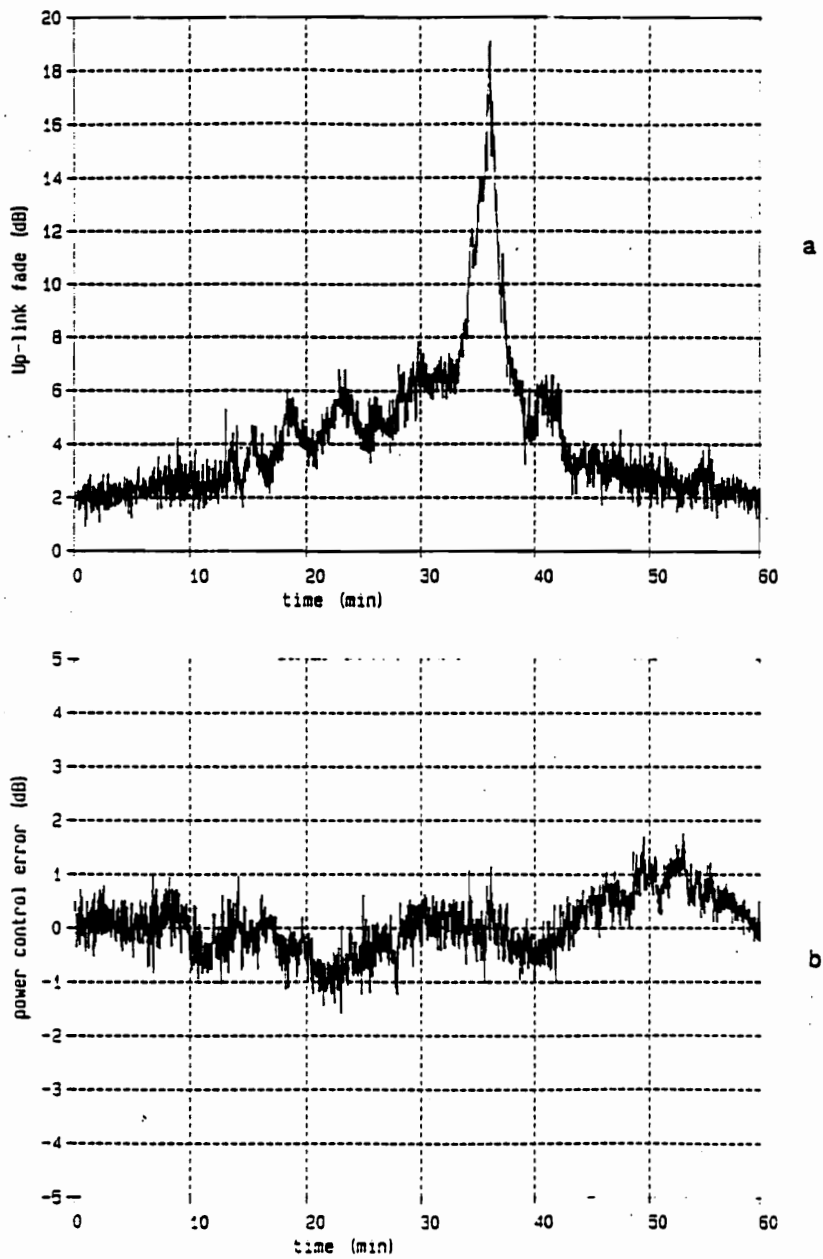
Figure 2.2-8: Improved Comsat ULPC algorithm.
a. uplink fade, b. power control error. No event date given [9].

2.3 THE MANNING DYNAMIC FADE MODEL

2.3.1 Maseng and Bakken Stochastic Dynamic Fade Model

Robert Manning [10][11] has taken a different approach to the problem. Manning begins with an assumed mathematical model for the fade mechanism. This is a "top down" method rather than the "bottom up" experimental approach used by Comsat. His approach is based on a stochastic dynamic rain attenuation model proposed by Maseng and Bakken [12]. Maseng and Bakken assumed that the rain fade process could be described as a first order Markov process. This means that in a discrete sampled system the present value of attenuation is some function of the last sample value and a random variable driven by a stochastic input process.

Maseng and Bakken model the temporal evolution of the link attenuation $A(t)$ using the parameter $x_A(t)$ which is given by:

$$\frac{dx_A}{dt} = -\gamma x_A + \sqrt{(2\gamma)}\, \xi(t) \qquad x_A(t) = \frac{lnA(t) - ln(L\Gamma_m)}{\sigma_{ln\Gamma}} \qquad (2.3\text{-}1)$$

where $A(t)$ is the link attenuation, L is the path length, $\xi(t)$ defines a white noise process where $\langle\xi(t)\rangle = 0$ and $\langle\xi(t_1)\xi(t_2)\rangle = \delta(t_1 - t_2)$. Γ_m is the mean specific attenuation in dB/L, and $\sigma_{ln\Gamma}$ is the standard deviation of the log of the specific attenuation. These last two parameters are obtained from location specific attenuation statistics. Maseng and Bakken assume that attenuation is lognormal, and that the fade slope increases with attenuation. The x_A variable is the result. Maseng and Bakken state that these assumptions agree with the reported observations of [13] and [14]. These assumptions are necessary in order to obtain a tractable solution for the nonlinear filtering problem presented by (2.3-1).

It is useful to note that (2.3-1) forms a system consisting of a low pass filter driving an exponential amplifier as shown in Figure 2.3-1:
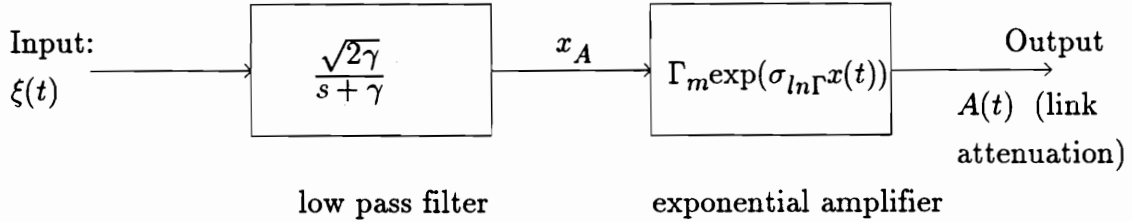
Figure 2.3-1:   Maseng and Bakken stochastic dynamic model for rain
attenuation.

2.3.2 Manning's Extension of the Maseng and Bakken Model

Maseng and Bakken note that (2.3-1) holds only for short paths. Manning
extends their work [10] by noting that there is an averaging effect which occurs
on longer paths. This extension results in a two-component Markov model, and
the resulting second order system is very similar to the system shown in Figure
2.3-1. The second order system adds an additional low pass filter prior to the
exponential amplifier to account for the long path averaging effects.

The solution for a such a multi-component nonlinear model is very difficult to
obtain. A number of simplifying assumptions are required in order to obtain an
ultimate solution. The first assumption is that the temporal variations along the
path can be described by an exponential correlation function. This results in a
smoothed random process $\zeta(t)$ given by:

$$\zeta(t) = \frac{1}{T_s} \int_{-\infty}^{t} \exp(\frac{t' - t}{T_s}) \xi(t') dt' \qquad (2.3\text{-}2)$$

where T_s is the averaging time. Differentiation of (2.3-2) with respect to t yields
a second differential equation:

$$\frac{d\zeta}{dt} = -\gamma_s \zeta + \gamma_s \xi(t) \qquad (2.3\text{-}3)$$

where $\gamma_s = (T_s)^{-1}$. This smoothed process given by (2.3-2) is used to drive the attenuation process:

$$\frac{dx_A}{dt} = \gamma x_A + \sqrt{2\gamma}\ \zeta(t), \quad x_A = \frac{\ln A(t) - \ln A_m}{\sigma_{\ln A}} \tag{2.3-4}$$

where A_m is the median link attenuation and $\sigma_{\ln A}$ is the standard deviation of the the log of attenuation. Both of these parameters are location specific and they can be obtained from rain statistics for the specified location [10]. The result is that (2.3-3) and (2.3-4) form a two component Markov process given by:

$$\frac{dX}{dt} = AX + G\xi \tag{2.3-5}$$

where

$$X = \begin{bmatrix} x_A \\ \zeta \end{bmatrix} \quad A = \begin{bmatrix} -\gamma & \sqrt{2\gamma} \\ 0 & -\gamma_s \end{bmatrix} \quad G = \begin{bmatrix} 0 \\ \gamma_s \end{bmatrix}$$

Now Manning is presented with the task of solving this nonlinear system. He cannot solve this system directly so he makes a simplification [10]. He compares the form of the solution for (2.3-5) with a simpler first order system given by:

$$\frac{dx_A}{dt} = -\gamma_s x_A + \sqrt{2\gamma_s}\ \xi(t) \tag{2.3-6}$$

that he can solve. From this comparison and from path geometry information, he concludes that:

$$\exp\left(-\frac{\gamma_1}{\gamma_s}\right) + \exp\left(-\frac{\gamma_2}{\gamma_s}\right) = \exp(-1) \tag{2.3-7}$$

with

$$\gamma_2 = \gamma_1\left(1 + \frac{2\ L\ \cos\Theta}{\pi\ R_C}\right)^{-1/2} \quad \text{and} \quad \gamma_1 = \frac{2\nu}{\pi R_C} \simeq 0.1336\ \text{min}^{-1}$$

where $R_C = 4$ km is the characteristic rain cell radius, L is the path length, ν

= 14 m/s is the characteristic speed of the rain cell, and Θ is the path elevation angle.

Choosing $L = 4$ km and $\Theta = 14°$, which are typical of the Blacksburg to OLYMPUS path, (2.3-7) results in $\gamma_s = 0.0696$ min^{-1} or $\gamma_s = 0.00112$ sec^{-1}. Equation (2.3-6) now becomes:

$$\frac{dx_A}{dt} = -0.00112 \ x_A + 0.0464 \ \xi(t) \tag{2.3-8}$$

This represents a single pole low pass filter with a 3 dB bandwidth of approximately 0.011 Hz.

2.3.3 Manning's Model Applied to Adaptive Power Control

Manning then turns to the measurement problem [11]: given the attenuation measurement $A_{obs}(t)$ at consecutive sampling times t_i, it is desired to obtain an estimate of the actual link attenuation $A^*(t_i) = A[x_A^*(t_i)]$. The $A_{obs}(t_i)$ measurement can come from a beacon or downlink signal strength measurement and the estimate $A^*(t_i)$ can be used to drive the power control. Note that $A^*(t_i)$ is an attenuation estimate and it must be frequency scaled if the measured signal is at a different frequency from that of the controlled uplink. The measurement $A_{obs}(t_i)$ is given by

$$A_{obs}(t_i) = A[x_A(t_i)] + n(t_i), \quad A[x_A(t_i)] \equiv A_m[\sigma_{lnA} \ x_A(t_i)] \tag{2.3-9}$$

where A_m and σ_{lnA} are given in (2.3-4) above. In addition, $n(t_i)$ is white noise characterized by $\langle n(t_i) \rangle = 0$ and $\langle n(t_i)n(t_j) \rangle = \sigma_n^2 \delta(t_i - t_j)$. Manning describes $n(t_i)$ as the measurement "noise." This can arise from measurement hardware inaccuracies or fluctuations in the frequency scaling ratio if scaling is used.

Manning's optimal estimate is given by [11]:

$$x_A^*(t_i) = \Phi_i x_A^*(t_i - 1) + \sigma_{x_A}^*(t_i) a(t_i) \tag{2.3-10}$$

where

$$\Phi_i \equiv \exp[-\gamma_s(t_i - t_{i-1})] \qquad (2.3\text{-}11)$$

which is the temporal transition coefficient and

$$\sigma_{x_A}^*(t_i) \equiv \left(K^{-1}(t_i) - b(t_i)\right)^{-1} \qquad (2.3\text{-}12)$$

which is the error variance of the optimal estimate. Finally $a(t_i)$, $b(t_i)$, and $K(t_i)$ are given by:

$$a(t_i) = \left(\frac{\sigma_{lnA}}{\sigma_n^2}\right) A[\hat{x}(t_i)]\big(A_{obs}(t_i) - A[\hat{x}(t_i)]\big) \qquad (2.3\text{-}13)$$

$$\hat{x}_A(t_i) = \Phi x_A^*(t_{i-1})$$

$$b(t_i) = \left(\frac{\sigma_{lnA}^2}{\sigma_n^2}\right) A[\hat{x}(t_i)]\big(A_{obs}(t_i) - 2A[\hat{x}(t_i)]\big)$$

$$K(t_i) = 1 + \Phi_i^2\big(\sigma_{x_A}^*(t_{i-1}) - 1\big)$$

Equation (3.2-10) is a recursive difference equation that represents a simple single pole Infinite Impulse Response (IIR) low pass filter [15]. It is driven by the last estimate, $x_A^*(t_{i-1})$ and something proportional to the present observation, $A_{obs}(t_i)$. $A[x_A^*(t_i)] \equiv A_m \exp[\sigma_{lnA} x_A^*(t_i)]$ converts $x_A^*(t_i)$ to attenuation.

2.3.4 Evaluation of the Manning's Dynamic Fade Model

In their paper, Maseng and Bakken [12] are very circumspect about the validity of their model. They raise the question as to whether or not the data they considered were adequate to validate the model for the intended purpose. They suggest that additional work based on the physics of rain storms or observed

rainrate and attenuation is in order. Subsequent work in this area suggests that some of the assumptions made by Maseng and Bakken may not be valid. Bottomley [16] implemented the Maseng and Bakken model and tested it with attenuation data measured at 11.6 GHz on the 10.7° elevation angle path between Blacksburg, VA USA and the SIRIO satellite. These measurements were made in 1980 and 1981. He found that model performance could be improved by driving it with a non-Gaussian input process. He also found that the rain attenuation process is nonstationary. The implication is that model parameters are a function of attenuation level.

While statistics of fade [13] and fade slope [17] have been shown to be lognormally distributed, instantaneous fade slope is not proportional to attenuation. This is shown in Chapter 3 of this dissertation. Thus the lognormal assumption is also in doubt.

One of the limitations of the Maseng and Bakken model is that it has no mechanism for a transition from periods of no rain to rain. The statistics that drive the model are derived from rain periods only. The assumption that the measurement and scaling "noise" are white may not be reasonable. Chapter 4 of this dissertation suggests that the scaling factor is a non-linear function of attenuation level and Bottomley's work hints at this as well. The model does not deal with water vapor and oxygen attenuation or receiver drift, none of which are zero mean.

Due to the model's complexity, Manning makes a number of simplifications and assumptions in order to obtain a solution. The model has yet to be tested with actual data so it is unknown what impact these simplifications and assumptions have on model performance.

The structure of Manning's model given by (2.3-10) is that of simple lowpass filter. It has two parameters which permit the choice of a "gain" which is the scaling factor and a "bandwidth" which defines some amount of smoothing. This structure is explored in some depth in Chapter 4.

2.4 ADDITIONAL ADAPTIVE CONTROL ALGORITHMS

2.4.1 Fade Dynamics

Monitoring the rate of change or fade slope, possibly conditioned on attenuation level, has been widely suggested as method for driving a fade countermeasure [17][18][19][20]. An algorithm driven by attenuation and fade slope could be used to predict the attenuation at some future time. This is of particular interest in systems that are centrally arbitrated and that have to deal with transmission and decision delays. Systems that change data rates and require resynchronization at the new rate would also benefit.

There appears to be good statistical evidence that the fade slope is log-normally distributed [13][17]. An example of this is shown in Figure 2.4-1. This suggests that there is a multiplicative effect that is related to fade depth.

Although widely suggested, no evidence has been found for an operational algorithm employing fade slope. The question is: does the proportionality that appears in the statistics hold in real time? Chapter 3 is an in depth look at this question [21].
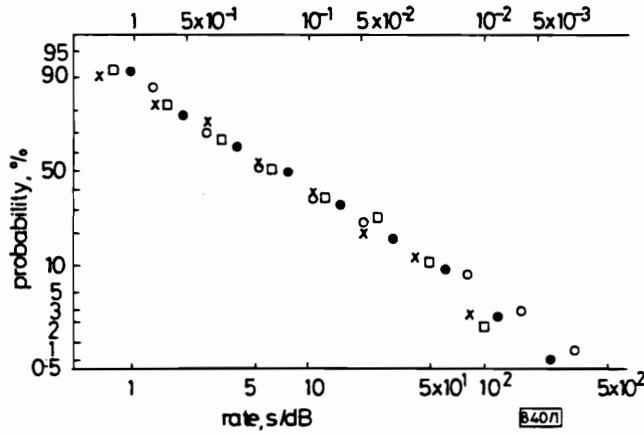
Probability $P(x < x_o)$ for rates in dB/s; $P(x \geq x_o)$ for rates in s/dB

ΔS values: o 1.5 dB   • 2.0 dB   □ 2.5 dB   × 3.0 dB

Figure 2.4-1: Conditional average values of positive rate in dB/s (right y-scale) and in s/dB (left y-scale), against conditional fade threshold S (x-scale) for indicated values of ΔS, i.e. $S < \text{fade} \leq S + \Delta S$ as reported by Matricciani [17].

2.4.2 NASA ACTS

The NASA Advanced Communications Technology Satellite (ACTS) program has spurred a renewed interest in the adaptive power control problem. ACTS is equipped with a 30 GHz uplink and a 20 GHz downlink so fade countermeasures are particularly important. The work of Manning described above is part of this interest.

Levitt [22] proposed a rain compensation algorithm (RCA) for the ACTS mobile terminal (AMT). Levitt's RCA adjusts data transmission rate rather than transmitter power as a fade countermeasure. The AMT modulation has DBPSK (differential binary phase shift keying) modulation with a (7, 1/2) convolution code, and the signal to noise ratio (SNR) required to achieve the specified BER

35

of 10^{-3} is 6.5 dB. The link margin, μ, is the difference in dB between the received SNR and the required minimum SNR:

$$\mu = \left(\frac{C}{N_o}\right) - 10 \, \log(R_b) - 6.5 \qquad (2.4\text{-}1)$$

where (C/N_o) is the received SNR in dB-Hz and R_b is the bit rate in bits per second (bps). The bit rate can be reduced to maintain μ positive as C/N_o degrades.

It is possible to select a data transmission rate of 9.6, 4.8 or 2.4 kbps with AMT. Given the system parameters of the AMT, it is uplink limited. With a link margin of 3 dB, an uplink fade of up to 2.15 dB can be tolerated at 9.6 kbps. The 4.8 kbps data rate can handle fades up to 5.17 dB, and acceptable link performance is guaranteed with 2.4 kbps in fades up to 8.17 dB.

While the choice of data rate can be under software control which is easier to implement than transmitter power adjustment, it is still necessary to identify and measure the fade. Levitt suggests that either Manning's model or a scaling algorithm like that of Comsat's could be employed for this purpose.

2.4.3 Direct Inter-establishment Experiment (DICE)

DICE is a proposed satellite video conferencing system to be used with ESA's OLYMPUS satellite. It is to employ a flexible video codec to reduce data throughput during periods of fading [22]. The codec is a combination of modem and processor which acts as direct sequence spread spectrum transceiver. Direct sequence spread spectrum is used because the data rate can be adjusted without altering the bandwidth of the transmitted signal and a change in data rate does not require resynchronization. The modem has a soft decision output which can be used to determine the level of fade and the data throughput is adjusted to compensate for the fade.

The unique feature in the DICE system is that the fade is determined in the decision process and system operation is totally under software control. This

fade countermeasure requires no interface with either receiver or transmitter electronics. This proposed system essentially monitors signal to noise ratio.

2.5 SUMMARY

It appears that open loop attenuation driven ULPC systems have generated the most interest. They are simple to implement and are inherently stable. It also appears that Comsat has done the most work toward implementing such a system. Comsat has published very little of their work and what is referenced here was somewhat difficult to obtain. One has to wonder if they haven't already solved the problem and perhaps they just aren't saying!

The success of any fade countermeasure depends on it ability to estimate a fade accurately. The stochastic model of Manning is elegant but as of yet untested. It appears that the largest body of actual experimental work involves signal strength measurement and scaling.

2.6 REFERENCES

[1] Yamamoto, Minoru, Hajime Fukuchi, and Makoto Takeuchi, "Up-Link Power Control Experiment," IEEE Transactions on Broadcasting, Vol. BC-28, No. 4, December 1982, pp. 157-159.

[2] Kosaka, K. Y. Suzuki, and I. Nishiyama, "Japan's CS(Sakura) Communications Satellite Experiments. Part VI-E: Communications Experiments: Experiments on Measures Against Rain Attenuation," IEEE Transactions on Aerospace and Electronic Systems, Vol. AES-22, May 1986, pp. 302-309.

[3] Egami, Shunichiro, "Individual Closed-Loop Satellite Access Power Control System Using Overall Satellite Link Quality Level," IEEE Transactions on Communications, Vol. COM-30, No. 7, July 1982, pp. 1806-1808.

[4] Egami, Shunichiro, "Closed-Loop Transmitting Power Control System for K-band Satellite Communications," <u>IEEE</u> <u>Transactions</u> <u>on</u> <u>Aerospace</u> <u>and</u> <u>Electronic Systems,</u> Vol. AES-19, No. 4, July 1983, pp. 577-584.

[5] Lin, K.T., C. Zaks, and D.V. Rogers, <u>Ku-Band</u> <u>Up-Link</u> <u>Power</u> <u>Control</u> <u>Development,</u> Comsat Technical Memorandum CL-13-87, November 12, 1987.

[6] Allnutt, J.E, <u>Satellite-to-Ground</u> <u>Radiowave</u> <u>Propagation,</u> IEE Electomagnetic Waves Series 29, Peter Peregrinus Ltd, London, 1989, pp. 220-223.

[7] Olsen, R.L., D.V. Rogers, and D.B. Hodge, "The aR^b Relation in the calculation of Rain Attenuation," <u>IEEE</u> <u>Transactions</u> <u>on</u> <u>Antennas</u> <u>and</u> <u>Propagation,</u> Vol. AP-26, 1978, pp. 318-329.

[8] D.B. Hodge, "Frequency Scaling of Rain Attenuation," <u>IEEE</u> <u>Transaction</u> <u>on</u> <u>Antennas</u> <u>and</u> <u>Propagation,</u> Vol. AP-25, 1977, pp. 446-447.

[9] Dissanayake, Asoka and Chaim Zaks, "Up-link Power Control Developments at Comsat Laboratories," Comsat Technical Note, STD/92-005, February, 1992.

[10] Manning, Robert M., "A Unified Statistical Rain Attenuation Model for Communication Link Fade Predictions and Optimal Stochastic Fade Control Design Using a Location Dependent Rain Statistics Database," <u>International</u> <u>Journal</u> <u>of</u> <u>Satellite</u> <u>Communications,</u> Vol. 8, 1990, pp. 11-30.

[11] Manning, Robert M., "A Stochastic Rain Fade Control Algorithm for Satellite Link Power Via the ACTS Rain Attenuation Model and Nonlinear Markov Filtering Theory," private correspondence with Dr. Warren L. Stutzman, April 1991.

[12] Maseng, Torleiv and Petter M. Bakken, "A Stochastic Dynamic Model of Rain Attenuation," <u>IEEE</u> <u>Transactions</u> <u>on</u> <u>Communications.,</u> Vol. COM-29, No. 5, May 1981, pp. 660-669.

[13]   Lin, S. H., "Statistical Behavior of Rain Attenuation,"   Bell System Technical Journal, Vol. 52, No. 4, April 1973, pp. 557-581.

[14]   Lin, S. H., "More on Rain Rate Distributions and Extreme Value Statistics," Bell System Technical Journal, Vol. 54, July/Aug. 1975, pp. 1052-1086.

[15] Jackson, Leland B. Digital Filters and Signal Processing, Kluwer Academic Publishers, Boston, MA, 1986, p. 31.

[16]   Bottomley, Gregory, E., "Modeling the Dynamic Behavior of Rain Attenuation," M.S Thesis, Department of Electrical Engineering, Virginia Polytechnic Institute and State University, 1985.

[17] Matricciani, E., "Rate of Change of Signal Attenuation From SIRIO at 11.6 GHz," Electronics Letters, Vol.17, No. 3, 5 February 1981, pp. 139-141.

[18] Dintelmann, F., "Analysis of 11 GHz Slant Path Fade Duration and Fade Slope," Electronics Letters, Vol. 17, No. 7, 2 April 1981, pp. 267-268.

[19]   Nackoney, O.G., and D. Davidson, "Results of 11.7 GHz CTS Rain Attenuation Measurements at Waltham, Massachusetts," Radio Science, Vol. 17, No. 6, Nov.-Dec. 1982, pp. 1435-1442.

[20] OLYMPUS Users Guide: UG-6-1 Part 1: Propagation Package, European Space Research and Technology Center, Noordwijk, Netherlands, Issue 3, March 1983, Section 7.4.3 "Rate of Change", p 127.

[21] Sweeney, Dennis G. and Charles W. Bostian, "The Dynamics of Rain-Induced Fades," IEEE Transactions on Antennas and Propagation, Vol. AP-40, No. 3, March 1992, pp. 275-278.

[22]   Levitt, Barry K., "Rain Compensation Algorithm for ACTS Mobile Terminal," IEEE Journal on Selected Areas in Communications, Vol. 10, No. 2, February 1992, pp. 358-363.

[23]   Tomlinson, M. and C.D. Huges, "Fade Countermeasure Techniques Employed in the DICE Experiment," Proceedings of the Olympus Utilization Conference, Vienna, Austria, 12-14 April 1989, pp. 117-124.

CHAPTER 3: FADE DYNAMICS

3.1 INTRODUCTION

Following the line of reasoning described in Section 2.4.1, an adaptive power control algorithm driven by fade slope and fade depth was investigated. The first issue that needed to be addressed was to find a relationship between fade slope and fade depth. This work produced some interesting and unexpected results!

Matricciani [1] and Dintelmann [2] have proposed that higher fade slopes are associated with higher attenuations and thus higher rain rates, but efforts to find a consistent relationship between fade slope and attenuation in experimental data have not been particularly successful. The work of Matricciani [3][4] suggests that this inability to connect attenuation and fade slope lies with higher-order effects and measurement difficulties rather than with the basic physics of the problem.

By applying an analysis published a number of years ago by Ruthroff [5], we can show from the physics of problem that there is no unique relationship between fade slope and rain rate, and thus none between fade slope and attenuation. Ruthroff calculates the path attenuation on a terrestrial radio link by developing an expression for fade slope and then taking its time integral. His approach gives useful physical insight into what controls the fade slope and it will be outlined here. While this fade slope model will be evaluated for a terrestrial radio path, the path geometry could be modified to apply to a satellite slant path.

This analysis shows that fade slope is strongly influenced by the velocity with which the rain falls. Hence fade slope is controlled by micrometeorological factors, such as wind and storm movement, as well as rainrate. In addition, the physics of the problem shows that the fade slope reaches its maximum when the first Fresnel zone is half filled with rain, where as the attenuation maximum is reached when the zone is completely filled.

41

3.2 FADE SLOPE

3.2.1 Fade Slope from First Fresnel Zone Filling

Consider a radio path with an isotropic antenna at each end. It can be shown that half of the energy that reaches the receiving antenna passes through the volume, V, defined by the first Fresnel Zone [6]. In practice, first Fresnel Zone terrain clearance is adequate to approximate free space for terrestrial paths [6], so the path can approximated by considering only the first Fresnel Zone. The first Fresnel zone is a prolate ellipsoid of revolution and it is shown in Figure 3.2-1. The path attenuation is related to how much water is in the volume, but the rate at which the attenuation changes is related to how fast this volume fills.

Let the volume be filled with a uniform distribution of N_D spherical water drops of diameter D centimeters, so the portion of the volume filled with water is given by the dimensionless parameter rain density, ρ_D :

$$\rho_D = \tfrac{\pi}{6} N_D D^3 \qquad\qquad (3.2\text{-}1)$$

This leads to the rain rate as:

$$R_D = \rho_D v_D \qquad\qquad (3.2\text{-}2)$$

where v_D is the drop velocity. The rain direction is defined by the direction of the drop velocity, so it is possible to write the rain rate as a vector quantity:

$$\vec{R} = \rho_D \vec{v}_D \qquad\qquad (3.2\text{-}3)$$

The attenuation on the path is proportional to the rain density and it is given by:

$$A_d = k(\lambda, D) L \rho_D \quad \text{(dB)} \qquad\qquad (3.2\text{-}4)$$

where $k(\lambda, D)$ is a function of the wavelength, the drop diameter, and the

dielectric constant of water. L is the path length. As the volume fills with rain, the rain density, ρ_D, in the volume will vary with time and space, and (3.2-4) may be modified to accommodate this change in density:

$$A_D = k(\lambda, D)\frac{L}{V} \int\limits_V \rho_D(x, y, x, t)dV \tag{3.2-5}$$

Assuming that there are no rain sources or sinks in the volume, any water that falls into the volume must eventually fall out of it. This fact can be expressed as a hydrodynamic continuity equation:

$$\vec{\nabla} \cdot (\rho_D \, \vec{v}_D) + \frac{\partial \rho_D}{\partial t} = 0 \tag{3.2-6}$$

This hydrodynamic continuity is easy to envision for a terrestrial path since the storm usually forms above the path. On a satellite slant path, the radio beam is more likely to intersect the storm with part of the Fresnel volume above the storm and part below it. In this case (3.2-5) should be integrated over only that part of the volume that is between the top of storm or the freezing layer and the bottom of the rain as it falls. It is also possible for the rain to evaporate before it reaches the ground. This could be accommodated by a dynamic geometry as well.

Substituting (3.2-6) into (3.2-5) gives an expression for the rate of change of attenuation:

$$\frac{dA_D(t)}{dt} = k(\lambda, D) \, \frac{L}{V} \int\limits_V [-\, \vec{\nabla} \cdot (\rho_D \, \vec{v}_D) \,] \, dV \tag{3.2-7}$$

Applying the divergence theorem, (3.2-7) can be converted into an integral over the exterior surface S of the first Fresnel Zone with $\rho_D \, \vec{v}_D$ written as the vector rain rate $\vec{R}$:

$$\frac{dA_D(t)}{dt} = k(\lambda, D) \, \frac{L}{V} \int\limits_S [-\, \vec{R} \cdot \vec{N} \,] \, dA \tag{3.2-8}$$

$\vec{N}$ is an outward pointing normal to the surface and dA is the projected differential area. At this point Ruthroff integrates (3.2-8) over time to obtain
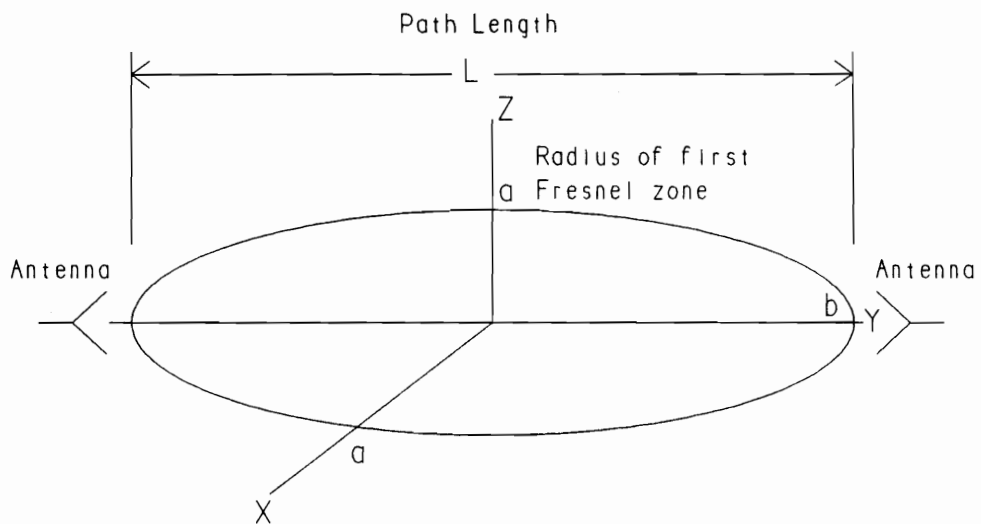
Figure 3.2-1: The first Fresnel zone.
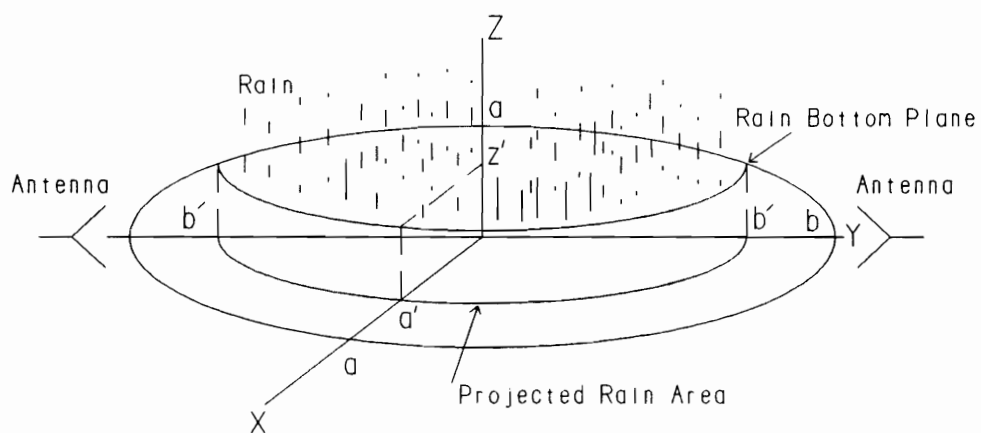
Figure 3.2-2: Intersection of rain and the first Fresnel zone.

the path attenuation; however, (3.2-8) is the desired expression for fade slope.

3.2-2 Evaluating Fade Slope

In order to evaluate (3.2-8), it will be assumed that the rain is a step function and the plane that defines the bottom of the rain is parallel to the path axis. This step function assumption is not necessarily a realistic description of an actual storm, but it is useful for setting an upper limit for the fade slope.

For a short terrestrial path this plane falls parallel to the ground as shown in Figure 3.2-2, thus $\vec{R} = -R\hat{k}$ where $\hat{k}$ is the unit vector parallel to the z axis. This permits reducing (3.2-8) to:

$$\frac{dA_D(t)}{dt} = k(\lambda, D) \left(\frac{L}{V}\right) R \int_S dA \tag{3.2-9}$$

All that must be done to evaluate (3.2-9) is to determine the area of the surface projected on the x-y plane by the intersection of the rain bottom plane and the first Fresnel Zone volume. This is an elliptical surface defined by the minor axis a' and major axis b' as shown in Figure 3.2-2. Notice that this area grows with time if the rain plane is above the x-y plane. Rain is only falling into the volume and the rate of change for the fade slope is positive. As the rain bottom plane falls below the x-y plane, rain begins to fall out the bottom of the volume while it continues to fall in from the top. The fade slope then decreases even though the attenuation continues to grow until the volume is completely filled with rain.

The minor and major axis, a' and b', of the projected surface can be found in terms of the point z' where the rain bottom plane intersects the z axis as shown in Figure 3.2-2. This intersection is a function of time and the velocity at which the rain bottom plane falls. The points z', a', and b' are given by:

$$z' = a - tv_D$$

$$a' = \sqrt{a - z'^2}$$

$$b' = b\sqrt{1 - \frac{z'^2}{a^2}} \qquad\qquad (3.2\text{-}10)$$

where a is $\sqrt{\lambda L}$, the radius of the first Fresnel zone, L is the path length, b is $L/2$, v_D is the drop velocity, and t is the time. Since the projected elliptic surface and the volume of the ellipsoid of rotation have closed form solutions, (3.2-9) can now easily be evaluated:

$$\frac{dA_D(t)}{dt} = 1.5 \; k(\lambda, D) \; R \left(\tfrac{b}{a}\right)\left(1 - \frac{[a - tv_D]^2}{a^2}\right) \qquad\qquad (3.2\text{-}11)$$

The $k(\lambda, D)$ factor can be evaluated using the work of Medhurst [7]; however, a more convenient method is to recognize that, in (3.2-4), $k(\lambda, D)\rho_D$ is the specific attenuation in dB/km. This attenuation is given by the familiar αR^β relationship tabulated in Olsen, Rogers, and Hodge [8]. So using αR^β and solving (3.2-2) for ρ_D, $k(\lambda, D)$ becomes:

$$k(\lambda, D) = \frac{(\alpha R^\beta)v_D}{R} \qquad\qquad (3.2\text{-}12)$$

Thus it is possible to evaluate the fade slope in terms of rain rate and drop velocity:

$$\frac{dA_D(t)}{dt} = 1.5 \times 10^{-3}(\alpha R^\beta) \; v_D \left(\tfrac{b}{a}\right)\left(1 - \frac{[a - tv_D]^2}{a^2}\right) \quad (\text{dB/sec}) \qquad (3.2\text{-}13)$$

where αR^β is in dB/km and v_D is in m/sec. Using the αR^β relation relaxes the requirement of uniform drop size assumed at the beginning of this analysis. It is possible to use any one of the many drop size distributions in (3.2-13). Since drops of different sizes travel at different velocities, the drop velocity v_D should be interpreted as a weighted average of the drop velocities rather than the velocity of individual drops. This interpretation makes the rain step function assumption somewhat unrealistic since the larger drops tend to fall with greater velocity. The step function assumption is still useful in placing an upper bound

on the fade slope.

Drop terminal velocities given by Medhurst [7] range from about 2 to 9 m/s for drop sizes from 0.05 to 0.7 cm. In the absence of data on storm movement, velocities in this range were used as a starting point in evaluating (3.2-13).

3.3 RESULTS AND CONCLUSIONS

3.3-1 Fade Slope Analysis Results

Using α and β at $\lambda = 1.5$ cm for a Marshal and Palmer drop size distribution (M-P DSD), attenuation and fade slope were evaluated for a 4.0 km path with a given rainrate and several different rain velocities. Attenuation, the time integral of the fade slope, is plotted in Figure 3.3-1 and fade slope is plotted in Figure 3.3-2. The path attenuation obtained from the time integral is identical to attenuation obtained by evaluating $\alpha R^{\beta} L$ for the path, so (3.2-13) agrees with Ruthroff's analysis and it gives self consistent results. Figure 3.3-1 shows that once a rain rate is chosen the ultimate attenuation is determined and rain velocity becomes a parameter.

Figure 3.3-2 shows that fade slope is very sensitive to the choice of the velocity parameter. From (3.2-13) it can be seen that fade slope is approximately proportional to rain rate because β is close to unity. This explains the log normal distribution found by Matricciani [1]. The fade slope also varies with the third power of velocity. The model predicts that the fade slope is much more sensitive to velocity than to rainrate. Rain velocity is strongly related to the character of the storm so it will be difficult to assign a unique real time fade slope for each rainrate.

Figure 3.3-2 also shows that fade slope reaches a maximum in the middle of the fade. Due to the nature of the Fresnel zone filling, the minimum value for fade slope occurs just at the beginning of the fade and when the attenuation reaches its maximum. Thus fade slope is not proportional to real time attenuation. This
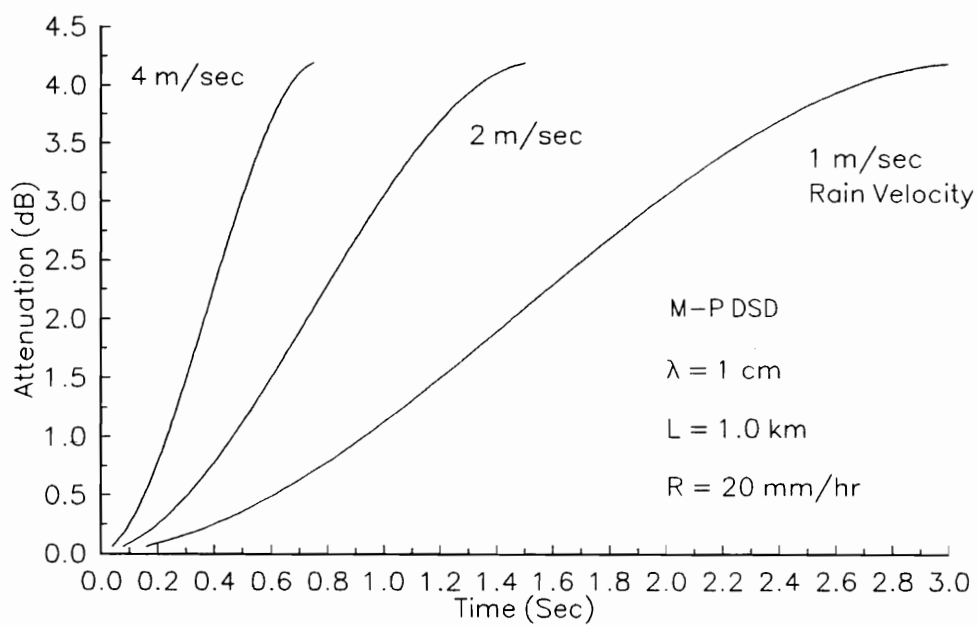
Figure 3.3-1: Attenuation versus time for rain velocities of 1, 2, and 4 meters/second.
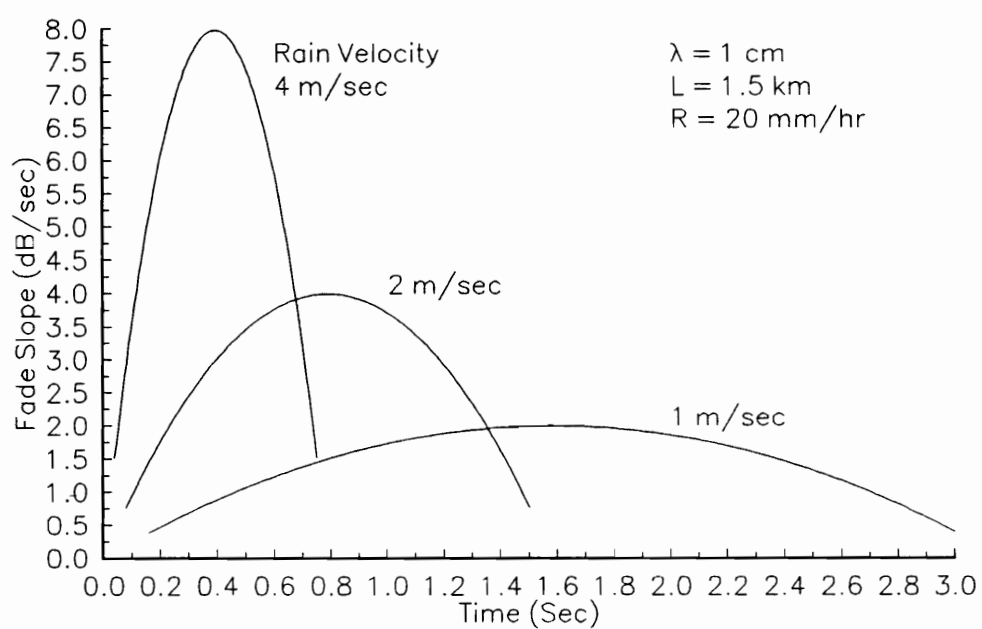
Figure 3.3-2: Fade slope versus time for rain velocities of 1, 2, and 4 meters/second.

phenomenon can be seen clearly on the leading edge of the measured fade shown in Figure 3.3-3. The fade and fade slope in Figure 3.3-3 were measured at 20 GHz on slant path from Blacksburg, VA to the OLYMPUS satellite. This is one of the most intense events observed in the measurement period from August 1990 through May 1991.
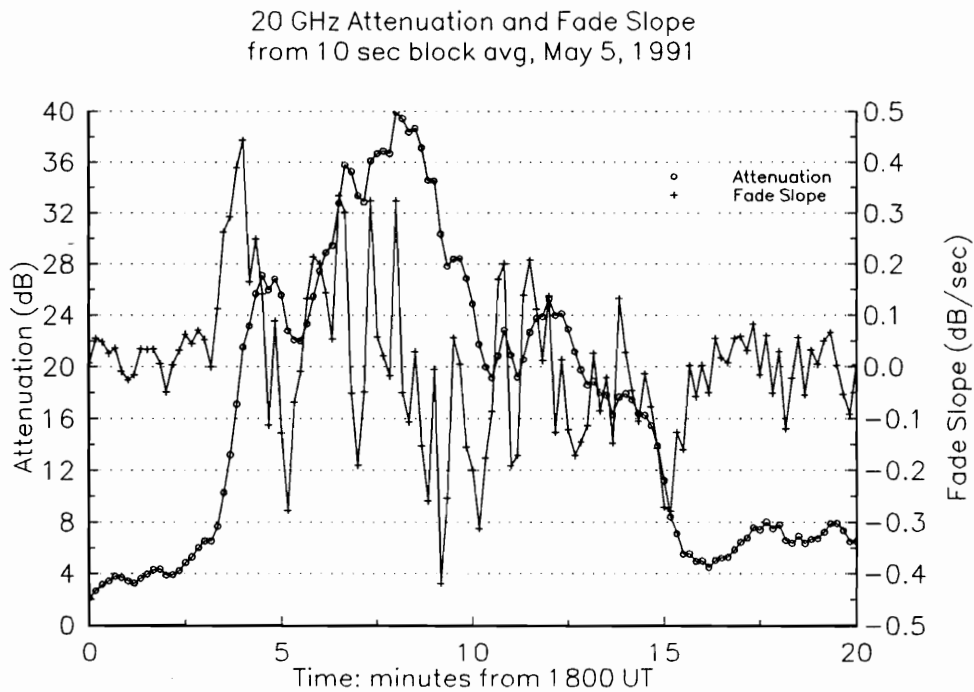
Figure 3.3-3: 20 GHz attenuation and fade slope measured on 14° elevation OLYMPUS earth-space path from Blacksburg, VA on May 5, 1991. This event began about 1800 UTC (1300 local time).

Data for this event were taken at a 10 Hz rate in a 3 Hz detection bandwidth as described in Section 1.5. One hundred samples were averaged to produce the 10 second block averages used to plot attenuation. The fade slope was calculated by taking the difference between successive 10 second averages and dividing by 10 to obtain fade slope in dB/sec.

As expected, the choice of a fixed rainrate and storm velocities on the order of drop velocities produces fade slopes that are higher than those observed in Figure 3.3-3, but the simple step function assumed in this analysis gives useful insight into physics of fade slope. In a real storm, fade dynamics will depend on many factors, such as the change in rainrate as the storm evolves, winds, storm movement, as well as rain velocity. A complete model requires realistic time functions for storm movement and changes in rainrate, but that is beyond the scope of this analysis.

3.3-2 Fade Slope as an Adaptive Power Control Parameter

The results of this effort to find a relationship between fade slope and fade depth produced some interesting results. The fade slope plotted in Figure 3.3-2 is an parabolic function centered about the maximum value of the slope. This was an unexpected result. After contemplating the physics and the mathematics, this result seems fairly obvious but it came initially as a surprise! The relationship between real time fade slope and fade depth does not have the proportionality that appears in the statistical relationship between them and while intuitively attractive, it does not appear that fade slope can be used to drive an adaptive control algorithm.

Additional work on a fade slope algorithm was terminated after this analysis and attention was turned to frequency scaling algorithms. Frequency scaling has potentially the same limitation as fade slope. Is the real time scaling ratio consistent enough with the statistical scaling ratio to use it to drive an adaptive power control algorithm?

3.4 REFERENCES

[1] Matricciani, E., "Rate of change of signal attenuation from SIRIO at 11.6 GHz," Electronics Letters, Vol. 17, No. 3, 5 February 1981, pp. 139-141.

[2] Dintelmann, F., "Analysis of 11 GHz slant path fade duration and fade slope," Electronics Letters, Vol. 17, No. 7, 18 February 1981, pp. 267-268.

[3] Matricciani, E., "Effects of filtering on statistics of rain-induced fade durations," Electronics Letters, Vol. 18, No. 6, 18 March 1982, pp 253-255.

[4] Matricciani, E., "Effects of filtering on rate of change of rain-induced attenuation," Electronics Letters, Vol. 18, No. 11, 27 May 1982, pp. 447-448.

[5] Ruthroff, C.L., "Rain attenuation and radio path design," Bell System Technical Journal, Vol. 49, January 1970, pp. 121-135.

[6] Livingston, Donald C., The Physics of Microwave Propagation, Prentice-Hall, Englewood Cliffs, NJ, 1970, pp. 43-53.

[7] Medhurst, R. G., "Rainfall attenuation of centimeter waves: comparison of theory and measurement," IEEE Transactions on Antennas and Propagation, Vol. AP-13, No. 4, July 1965, pp. 550-564.

[8] Olsen, R.L, D. V. Rogers, and D. B. Hodge, "The aR^b relation in the calculation of rain attenuation," IEEE Transactions on Antennas and Propagation, Vol. AP-26, No. 2, March 1978, pp. 318-328.

CHAPTER 4: UPLINK POWER CONTROL USING FREQUENCY SCALING

4.1 INTRODUCTION

The Japanese and Comsat tests reported in Sections 2.1 and 2.2 successfully employed frequency scaling for ULPC. A simple fade countermeasure would be to measure the downlink attenuation and scale it by some appropriate factor in order to estimate the uplink attenuation. This value for uplink attenuation can then be used to control uplink transmitter power or adaptive coding. In order to implement a successful control algorithm, it is necessary to know the instantaneous ratio between attenuations at the uplink and downlink frequencies. Both the Comsat and Japanese tests reported that this ratio is not a constant but neither addressed its variability.

A number of scaling relationships have been proposed to scale long term attenuation statistics [1][2]. Each has its own applicability and limitations, but these relations are intended for scaling attenuation statistics and not real time scaling. We undertook a study to compare the ratio used to scale statistics with the measured real time ratio. The real time ratios were calculated from 10 second average attenuation values. While this is not exactly real time, the averages were necessary in order to remove the effects of the scintillation. The results of this study suggest that statistical scaling ratios are usable for instantaneous scaling, if certain limitations are observed, even though there is no real time deterministic relationship between 20 and 30 GHz attenuation.

Once we determined that scaling is a viable method for ULPC, we tested it on a number of selected fade events recorded on the OLYMPUS - Blacksburg, VA USA path at 20 and 30 GHz. These fades were observed between November of 1990 and May of 1991.

A simple difference equation ULPC algorithm, one similar in form to that proposed by Manning and described in Section 2.3, was applied to each event. Optimum scaling and smoothing filter values were obtained by minimizing the

squared error for each event. In addition, a time weighted average scaling ratio and smoothing filter were obtained for the entire data set. Both the optimum and the average values were used to drive the ULPC algorithm for each event and their performance was evaluated.

Since ACTS will be equipped with a 30 GHz uplink beacon, an ULPC algorithm driven by OLYMPUS 30 GHz beacon data was also implemented. Optimum and average values of scaling and filtering were obtained and the performance of this algorithm was compared with the algorithm driven by scaled downlink attenuation.

4.2 STUDY OF REAL TIME FREQUENCY SCALING

4.2.1 Real Time and Statistical Scaling Ratios and Scaling Ratio Hysteresis

A number of frequency scaling relations are available for scaling long term attenuation statistics [1][2]. All of these scaling relations produce a single valued scaling factor. The Boithias relation is non-linear [1] and it produces a scaling factor that is a function of attenuation level, but none of the various relations explain the unusual hysteresis effect in the scaling ratio that has been observed during some events [3]. For an example of this effect, see Figure 4.2-1.

Each of the scaling relations proposed in [1] and [2] has its own claim of validity and accuracy. For our study of real time scaling, the scaling ratio given by the CCIR method [2] was used as a standard of comparison. It is easy to calculate and widely used. It is given by:

$$\frac{A_2}{A_1} = \frac{\phi(f_2)}{\phi(f_1)} \qquad \text{where} \quad \phi(f) = \frac{f^{1.72}}{1 + 3 \times 10^{-7} f^{3.44}} \qquad (4.2\text{-}1)$$

where A_2 and A_1 are the attenuations in dB at frequencies f_2 and f_1 in GHz, respectively.

The CCIR method results in a scaling ratio of approximately 1.97 for $A(30$ GHz$)/A(20$ GHz$)$ for the 30/20 GHz OLYMPUS beacons. For a description of these beacons and the Virginia Tech receiving system, see Section 1.5. The attenuation data used for this study were recorded at a 10 Hz sample rate and then 100 samples were averaged to obtain the 10 second block averages used in the plots. This is equivalent to filtering the data with a 0.044 Hz lowpass filter.

Examination of a number of events shows that the ratio of 30 GHz to 20 GHz attenuation changes during some events. Figure 4.2-2 shows an intense thunderstorm event that occurred at Virginia Tech on November 5-6, 1990. Note that the attenuation plot is limited to approximately 38 dB by the beacon receiver's dynamic range. Figure 4.2-1 shows 30 GHz attenuation plotted against 20 GHz attenuation for this event with the CCIR scaling ratio plotted as a straight line. This plot forms a "loop." That part of the event prior to the attenuation maximum, denoted by the +'s in Figure 4.2-1, has a scaling ratio much less than the scaling ratio predicted by the CCIR relation and it forms the lower half of the loop. The upper side of the loop is formed by that part of the event, plotted with o's in Figure 4.2-1, that was measured after the attenuation maximum. The data more closely follow the CCIR relation for this part of the event.

4.2.2 Drop Size Distributions and Attenuation

We suggest a change in the drop size distribution (DSD) during the event as an explanation for this scaling behavior. Thunderstorm rains tend to have more large drops than uniform stratiform rains with the same rainrate, and different DSD's will produce different attenuations for the same rainrate. To test this hypothesis, we calculated specific attenuation using $\alpha = aR^b$, where α is the specific attenuation (dB/km) and R is the rainrate (mm/h), as tabulated in [4]. Coefficients a and b at 20 and 30 GHz were chosen for a Marshall-Palmer (MP) drop size distribution and for the "Thunderstorm" distribution (J-T) of Joss [5]. The MP distribution describes a uniform rain while the J-T distribution more closely describes a heavy "thunderstorm" rain.

30 vs 20 GHz Attenuation
Nov 5-6, 1990 2300-0100 UTC 10 sec avg
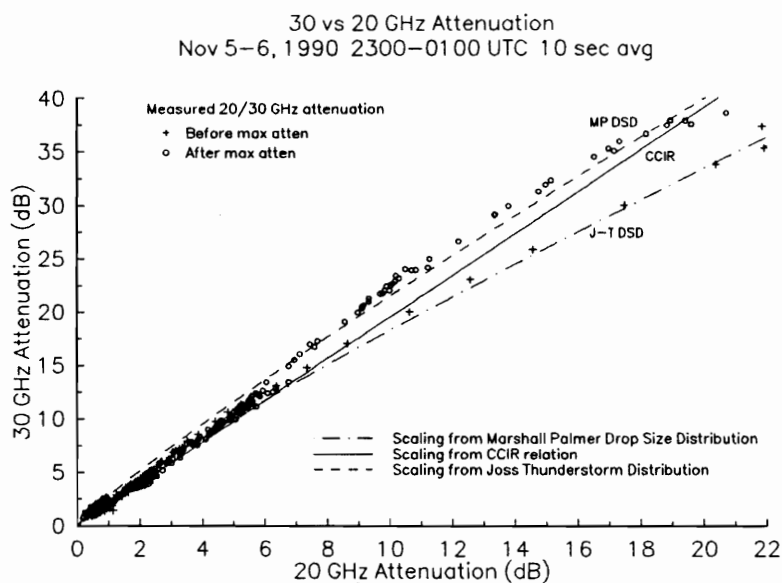
Figure 4.2-1: November 5-6, 1990 30 GHz versus 20 GHz attenuation plotted with various scaling relations.

20 and 30 GHz Attenuation
Nov. 5-6, 1990 2300-0100 UTC 10 sec avg
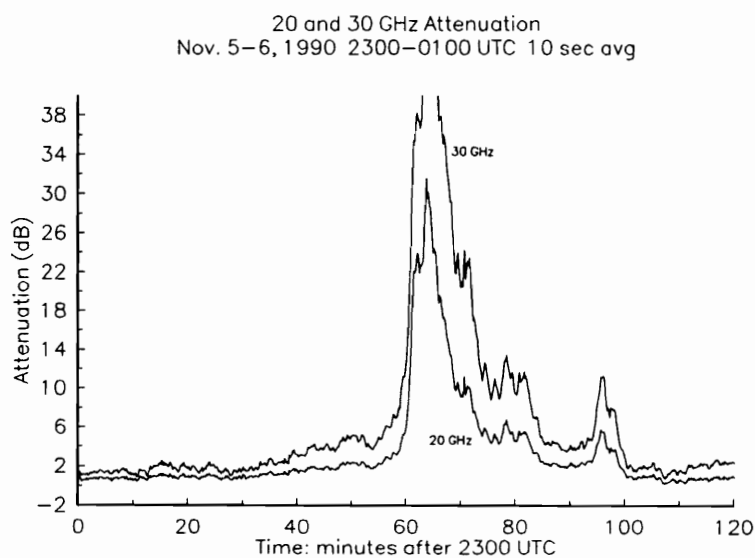
Figure 4.2-2: November 5-6, 1990 20 GHz and 30 GHz attenuation. The 30 GHz attenuation is limited to approximately 40 dB due to receiver dynamics.

Attenuation at 30 GHz versus 20 GHz for a mean path length of 4 km using these two distributions is plotted with the November 5-6, 1990 event in Figure 4.2-1. The J-T DSD attenuation produces a scaling ratio less than the CCIR value. It fits the leading portion of this event while the MP DSD is a better fit for the trailing portion of the event. At lower attenuation levels, the two distributions predict scaling ratios that are very close to that of the CCIR relation. Thus, it is reasonable to expect little difference at the beginning and end of the event when the attenuation is low. In an actual event there will be a gradual change in the drop size distribution as the event evolves, and for high attenuation events, this difference can be great enough to produce the observed "loop" or hysteresis effect in the scaling ratio.

The actual drop size distribution can vary greatly from event-to-event. There may also be large place-to-place variations. Specific attenuation obtained from radar reflectivity measurements exhibits a wide variation. Battan lists sixty-nine different relationships reported by researchers from all over the world from 1947 to 1970 [6]! This variation is evident in the May 6, 1991 event plotted in Figure 4.2-3 and Figure 4.2-4. This event was the result of a very intense thunderstorm and the hysteresis effect is again observed. The reduction in scaling factor, however, is much greater than that predicted by the Joss DSD; nevertheless the low attenuation portion of the event still follows CCIR scaling relation.

The CCIR relation holds well during these intense events when the attenuation is less than approximately 6 dB at 20 GHz. Figure 4.2-5 is the 30 GHz versus 20 GHz attenuation for the November 5-6, 1990 event for 20 GHz attenuation less than 6 dB. It is difficult to distinguish the beginning and the end of the event as shown in Figure 4.2-5.

This hysteresis effect was not observed in less intense events. Figure 4.2-6 shows an event that is typical for a widespread stratiform rain with a peak 20 GHz attenuation of about 4 dB. Figure 4.2-7 shows 30 GHz attenuation versus 20 GHz attenuation for this event, and the majority of the event falls between the CCIR relation and the MP-DSD as plotted in Figure 4.2-7.

20 and 30 GHz Attenuation
May 6, 1991 1700–1900 UTC 10 sec avg
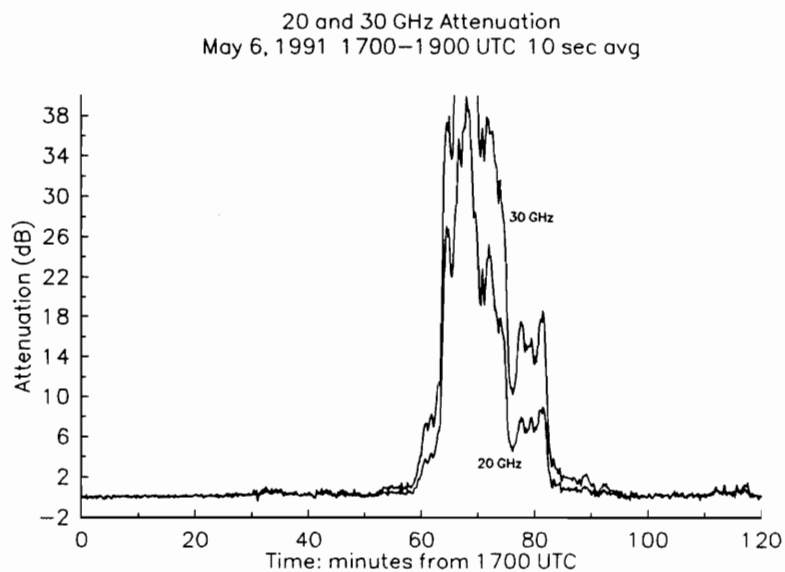
Figure 4.2-3: May 6, 1991 20 GHz and 30 GHz attenuation.

30 vs 20 GHz Attenuation
May 6, 1991 1700–1900 UTC 10 sec avg
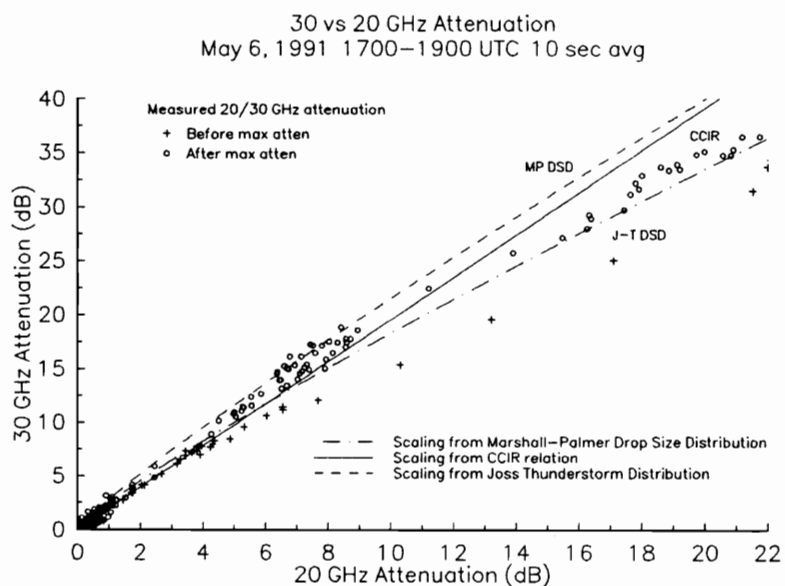
Figure 4.2-4: May 6, 1991 20 GHz versus 30 GHz attenuation
plotted with various scaling relations.

30 vs 20 GHz Attenuation
Nov 5–6, 1990 2300–0100 UTC 10 sec avg
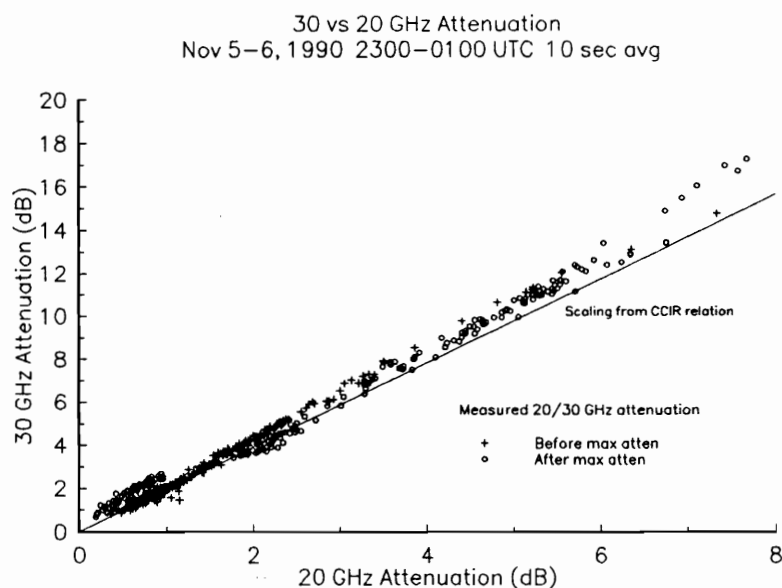
Figure 4.2-5: November 5-6, 1990 30 GHz versus 20 GHz attenuation for 20 GHz attenuation less than 6 dB.

20 and 30 GHz Attenuation
May 21, 1991 0700–0900 UTC 10 sec avg
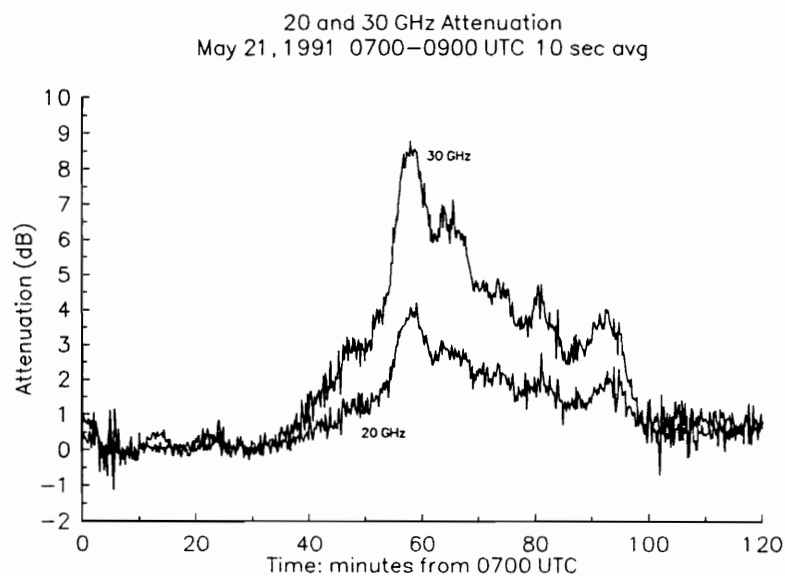
Figure 4.2-6: May 21, 1991 20 GHz and 30 GHz attenuation.
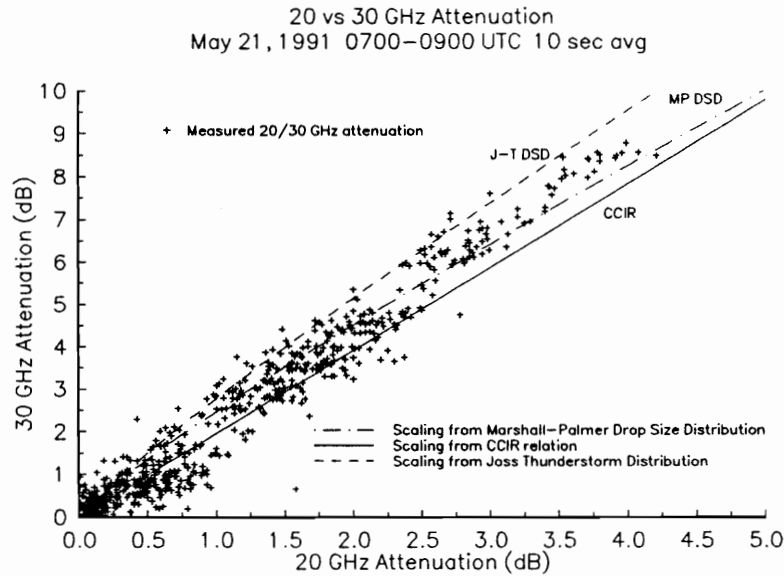
Figure 4.2-7: May 21, 1991 20 GHz versus 30 GHz attenuation. The solid line is the scaling predicted by the CCIR scaling relation.

4.2-3 Scaling Ratio Implications for ULPC

Differences in drop size distributions that occur during the evolution of a rainstorm can produce different scaling ratios that depart from simple scaling relations such as the CCIR relation. This departure occurs at higher attenuation levels and it is associated with heavy "thunderstorm" type rain. As a result, for attenuations above 6-8 dB at 20 GHz, it is not possible to obtain a single value for the scaling ratio. This complicates the use of a simple scaling relation to drive a fade countermeasure. This effect does not appear at lower attenuation levels so a simple scaling law controller could be implemented successfully at these attenuation levels. Since a 6 dB fade at 20 GHz is equivalent to an approximately 12 dB fade at 30 GHz and most proposed fade countermeasures can only compensate for about 10 dB of uplink fade at 30 GHz, a simple attenuation scaling controller could be implemented for ULPC at 30 GHz if the dynamic range is limited to approximately 10 dB.

60

4.3 OTHER ATTENUATION EFFECTS

4.3.1 Attenuation Due to Water Vapor and Atmospheric gases

In addition to rain induced attenuation, there is attenuation due to atmospheric gases, water vapor, and scintillations that must be considered. Using the CCIR algorithm [7], the attenuation due to atmospheric gases, predominately oxygen, in clear air from Blacksburg to OLYMPUS was calculated as 0.42 dB at 30 GHz and 0.23 dB at 20 GHz. The gaseous attenuation at 20 and 30 GHz scales at a ratio of 1.77. This is close to the rain attenuation scaling ratio of approximately 1.97.

This attenuation is a function of temperature and atmospheric pressure. While these may change during a storm, the resulting change in gaseous attenuation during the storm is expected to be relatively small, so the power control error introduced by ignoring this change in attenuation is small.

The attenuation introduced by water vapor is a more serious problem since it is larger in magnitude than the oxygen attenuation, and it is actually less at 30 GHz than at 20 GHz. Attenuation due to water vapor is predominantly a function of humidity and temperature, both of which are likely to change during a storm. Using the method outlined in [7], the water vapor attenuation on the Blacksburg to OLYMPUS path was estimated for a temperature of 20° C:

Table 4.3-1: Attenuation due to water vapor on the Blacksburg to OLYMPUS path.		
Frequency	Relative Humidity	
	50%	100%
20 GHz	1.07 dB	2.24 dB
30 GHz	0.74 dB	1.40 dB

If the increase in relative humidity is due to the storm, then there will be an increase in path attenuation of 1.17 dB at 20 GHz and 0.66 dB at 30 GHz. If the ULPC algorithm cannot distinguish between rain and water vapor attenuation, it will scale the 1.17 dB of additional 20 GHz attenuation by a factor of approximately 1.97. This will result in an estimate of 2.34 dB of additional 30 GHz attenuation. In actuality, the 30 GHz attenuation will have increased by only 0.66 dB, and the result is an overcompensation of 1.68 dB. This is a potentially large error.

Figure 4.3-1 shows an event where the 20 GH attenuation briefly exceeds 30 GHz at low levels. This condition is probably due to dominance of water vapor attenuation over rain attenuation.
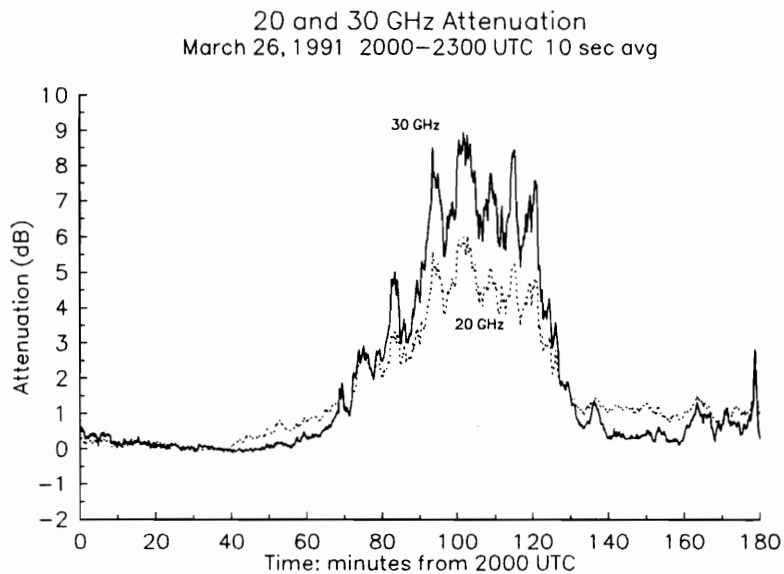
Figure 4.3-1: March 26, 1991 event showing greater attenuation at 20 GHz than at 30 GHz at low attenuation due to water vapor attenuation.

Water vapor attenuation depends on a number of factors and their change during a storm is difficult to quantify. We decided to ignore this source of error for our initial tests and it does not appear that this assumption introduced significant errors in practice. Ihara and Furuhama [8] made the same assumption with no apparent ill effect.

4.3.2 Scintillations

Scintillations represent a different problem. Scintillations scale with the ratio of $(f_2)/(f_1)^{7/12}$ where f_2 and f_1 are the frequencies of interest [9]. This results in a scaling ratio from 20 to 30 GHz of approximately 1.27. The rain fade scaling factor of 1.97 will have a tendency to increase the errors due to scintillations.

The Comsat ULPC experiments described in Section 2.2 were reasonably successful in counteracting the effects of scintillation. This was possible because Comsat used the same antenna for both the 14 GHz uplink and 11 GHz downlink. The only delay in the system was that of the controller and one earth-to-satellite round trip time, so the scintillations on the downlink are still correlated with uplink scintillations. The 20 and 30 GHz antennas for the Virginia Tech OLYMPUS experiment are not co-located, so the up and downlink scintillations in our data are not correlated.

Delay in the control system can also decorrelate scintillations so that it is not possible for the ULPC to compensate for them. Systems which have some type of centrally arbitrated power control may experience delays on the order of seconds, so it was desired to investigate the effect of delay. If it is not possible to compensate for the scintillations, the 20 GHz signal can be smoothed or filtered so the ULPC follows the fade envelope. This should reduce the errors caused by scintillations, but filtering may introduce its own errors due to filter delay so it is desirable to investigate the effects of delay.

4.4 DEVELOPING AN ULPC ALGORITHM

4.4-1 Estimator/Predictor Model for ULPC

The availability of fade data in sampled form, the work of Manning described in Section 2.3, and the desire to smooth the data to reduce the effect of scintillations suggest that some kind of digital filter could be implemented as an ULPC algorithm. A generalized model with output $y(t)$ driven by input $u(t)$ is given by [10]:

$$A(q)y(t) = \frac{B(q)}{F(q)}q^{-k}u(t) + \frac{C(q)}{D(q)}e(t) \tag{4.4-1}$$

where A, B, C, D, and F are polynomials in the delay operator q^{-1}:

$$A(q) = 1 + a_1 q^{-1} + ... + a_n q^{-n}$$

$$B(q) = b_0 + b_1 q^{-1} + ... + b_m q^{-m}$$

$$C(q) = 1 + c_1 q^{-1} + ... + c_p q^{-p}$$

$$D(q) = 1 + d_1 q^{-1} + ... + d_r q^{-r}$$

$$F(q) = 1 + f_1 q^{-1} + ... + f_s q^{-s}$$

The order of the polynomials is given by n, m, p, r, and s respectively and $e(t)$ is assumed to white noise with variance λ. The output $y(t)$ is the estimated or predicted value of 30 GHz attenuation when driven by the input $u(t)$ which can be either 20 GHz attenuation from the downlink or 30 GHz attenuation obtained from a 30 GHz uplink beacon. The parameter k is the number of delays between the input and the output. By selecting k it is possible simulate system delay. Obviously setting $k = 0$ for the 30 GHz uplink beacon case makes little sense.

The Output Error (OE) form of (4.4-1) can be obtained by setting $A = C = D = 1$

to obtain [10]:

$$y(t) = \frac{B(q)}{F(q)} q^{-k} u(t) + e(t) \qquad (4.4\text{-}2)$$

This form is intuitively attractive because it is possible to select $B(q)$ and $F(q)$ so that the effect of disturbance $e(t)$ can be minimized. Solving for the b's and f's is a system identification problem and the Matlab System Identification Tool Box [11] function "oe" will solve (4.4-2) for these parameters given the input $u(t)$, the output $y(t)$, the polynomial orders m and s, and the delay k. The function oe seeks the b and f values which produce the minimum squared error (MSE) for the system given the delays.

4.4-2 Choosing Model Parameters

It is necessary to choose the polynomial order: m and s. The estimation/prediction should improve as the order is increased at the cost of increasing algorithm complexity. Setting $s = 0$ results in a finite impulse response (FIR) filter and an infinite impulse response (IIR) filter results for any value of s other than zero. The linear phase properties of the FIR filter are not needed in this case, and IIR filters generally produce better amplitude performance for a given number of parameters if the startup transients can be tolerated [12]. The simplest IIR filter would result from $s = 1$.

As the order of m is increased, more of the past is used to predict the future. For the same input/output data, increasing the order should reduce MSE. Figure 4.4-1 is plot of error versus order, m, with $s = 1$ for the November 5-6, 1990 event. 20 GHz scaled to 30 GHz was chosen for Figure 4.4-1 so that delay parameter, k, can be set to zero. The error in Figure 4.4-1 was calculated using the Matlab "compare" function [13]. Figure 4.4-1 shows that the error drops slowly as the order is increased but there appears little to be gained for $m > 1$. This also suggests that the event's past history is of little additional value and it tends to confirm Manning's Markov assumptions and the conclusion that fade slope is not a useful parameter for ULPC.

The simplicity of a lower order algorithm is attractive and there is little performance advantage in higher orders so $m = 0$ and $s = 1$ was chosen. With this choice (4.4-2) reduces to the same form as Manning's model described in Section 2.3. This will permit future performance comparisons when data are published for this algorithm.

The input/output delay, k, can be chosen to simulate the system delay. Delays of 0, 1, 5, 10, and 20 seconds were chosen. The zero second delay is an estimator
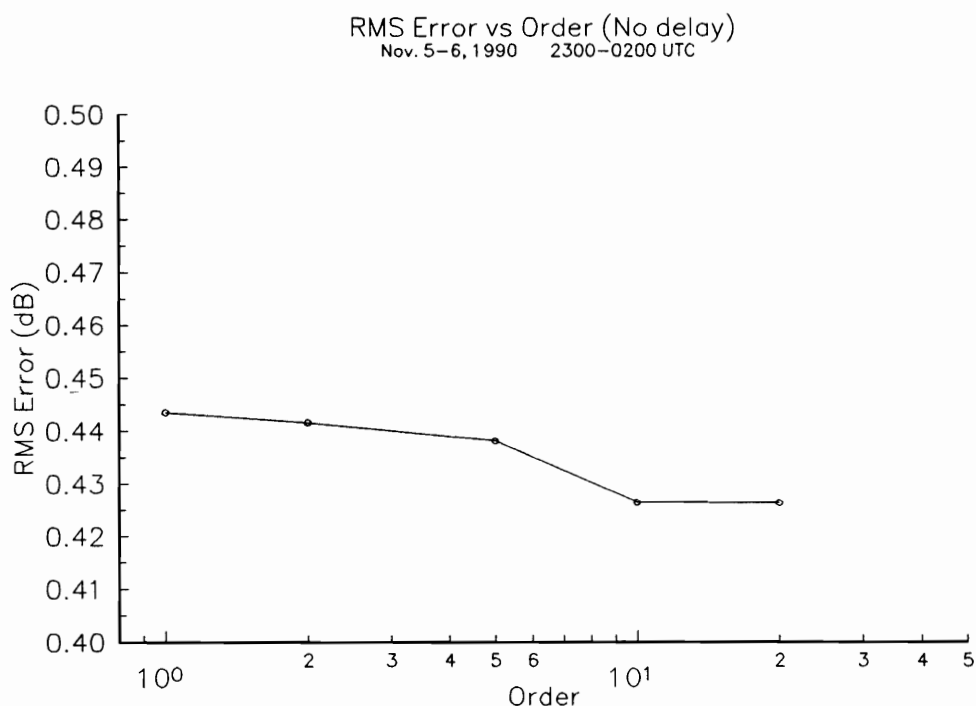
Figure 4.4-1: Model error versus model order for the November 5-6 1990 event. 20 GHz scaled to 30 GHz with no delay.

of the present value and other delays represent predictors for future values. A one second delay represents a typical minimum value for an ULPC system that operates on telemetry or is centrally arbitrated. The longer delays were chosen to investigate how fast the algorithm deteriorates with time. Figure 4.4-2 plots error versus delay for the November. 5-6 event for a simple delay with no filtering and with filtering using $m = 0$ and $s = 1$. In this case, the 30 GHz

predicting 30 GHz was used so the effect of decorrelation with time could be observed. The optimum b's and f's were obtained with Matlab function oe for each delay.

As expected, the error increases quickly with delay up to about 0.5 second. This is due to the decorrelation of the scintillations. Also as expected, the filtering improves the performance. The error performance is relatively constant from 0.5 second up to about 10 seconds of delay which suggests that the underlying fade process is a very low frequency phenomenon.

Error vs Delay Time
Nov. 5−6, 1990 2300−0200 UTC
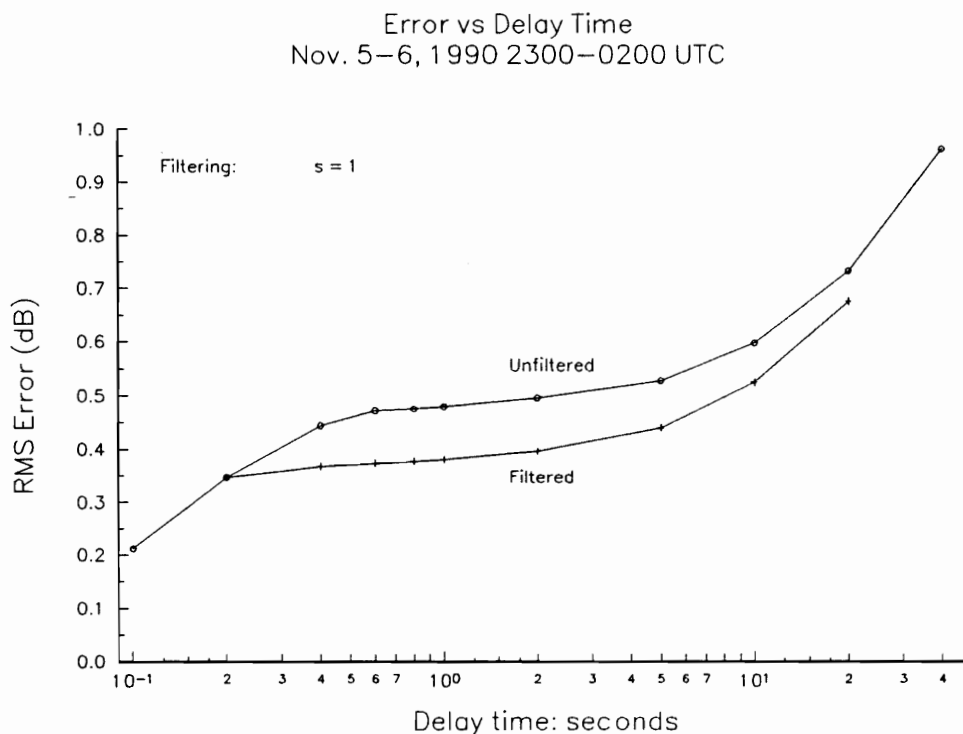
Figure 4.4-2: RMS error versus delay for 30 GHz predicting 30 GHz.

The final algorithm is given by:

$$\widehat{A}_{30}(t\,|\,t-k) = fA_{30}(t-1) + bA_{20}(t-k) + e(t) \qquad (4.4\text{-}3)$$

with the error $e(t) = \widehat{A}_{30}(t\,|\,t-k) - A_{30}(t)$

$A_{30}(t)$ is the actual value of 30 GHz attenuation at time t, $\widehat{A}_{30}(t\,|\,t-k)$ is the estimate of 30 GHz attenuation at time t obtained from the value of the 20 GHz attenuation at time $t-k$ and the previous value of A_{30} which is $A_{30}(t-1)$. When $k=0$, the present value of A_{20} and the previous value of A_{30} are used to generate the current estimate $\widehat{A}_{30}$. In this case, (4.4-3) reduces to:

$$\widehat{A}_{30}(t) = fA_{30}(t-1) + bA_{20}(t) + e(t) \qquad (4.4\text{-}4)$$

with the error $e(t) = \widehat{A}_{30}(t) - A_{30}(t)$.

In operation the actual values of 30 GHz attenuation, A_{30}, are not available so it is necessary to predict or estimate the present 30 GHz attenuation from the previous <u>estimate</u>. Driving the algorithm with the previous estimate, it is possible to write (4.4-4) as:

$$\widehat{A}_{30}(t) = f[f\widehat{A}_{30}(t-2) + bA_{20}(t-1)] + bA_{20}(t) + e(t) \qquad (4.4\text{-}5)$$

$$= f^2\widehat{A}_{30}(t-2) + fbA_{20}(t-1) + bA_{20}(t) + e(t)$$

$$= f^2[f\widehat{A}_{30}(t-3) + bA_{20}(t-2)] + fbA_{20}(t-1) + bA_{20}(t) + e(t)$$

$$= f^3\widehat{A}_{30}(t-3) + f^2bA_{20}(t-2) + fbA_{20}(t-1) + bA_{20}(t) + e(t)$$

$$= f^3[f\widehat{A}_{30}(t-4) + bA_{20}(t-3)] +$$

$$f^2bA_{20}(t-2) + fbA_{20}(t-1) + bA_{20}(t) + e(t)$$

$$= f^4 \widehat{A}_{30}(t-4) + f^3 b A_{20}(t-3) +$$

$$f^2 b A_{20}(t-2) + f b A_{20}(t-1) + b A_{20}(t) + e(t)$$

$$= f^j \widehat{A}_{30}(t-j) + f^{j-1} b A_{20}(t-j+1) + \ldots$$

$$+ f^2 b A_{20}(t-2) + f b A_{20}(t-1) + b A_{20}(t) + e(t)$$

If the initial value of $\widehat{A}_{30}(t-j)$ is set zero then (4.4-5) can be written as:

$$\widehat{A}_{30}(t) = b \sum_{i=1}^{\infty} f^i A_{20}(t-i)$$

$$= b \sum_{i=1}^{\infty} f^i q^{-i} A_{20}(t)$$

$$= \frac{b}{1 - fq^{-1}} A_{20}(t) \tag{4.4-6}$$

Equation (4.4-6) is the same as (4.4-2) above with $y(t) = \widehat{A}_{30}(t)$ and $u(t) = A_{20}(t)$. In the same way it can be shown that the predictor form of (4.4-5) is:

$$\widehat{A}_{30}(t \mid t-n) \;\; = bq^{-k} \sum_{i=1}^{\infty} f^i A_{20}(t-i)$$

$$= bq^{-k} \sum_{i=1}^{\infty} f^i q^{-i} A_{20}(t)$$

$$= \frac{q^{-k} b}{1 - fq^{-1}} A_{20}(t) \tag{4.4-7}$$

where k is the number of delays in the prediction.

The analysis that leads to (4.4-6) and (4.4-7) assumes that the entire time history from $t = -\infty$ is available. This is not the case since the event begins at some time t_o and it is necessary to set all values of A_{20} and $\widehat{A}_{30}$ to zero for all time prior to t_o. An examination of (4.4-5) reveals that the $\widehat{A}_{30}$ term dies off exponentially. The actual value for f is approximately 0.9 so the error introduced by setting the initial value of $\widehat{A}_{30} = 0$ becomes less than 1% after 50 or so samples. This represents only 5 seconds of data so the error introduced by this assumption is negligible.

As previously noted (4.4-6) and (4.4-7) form a single pole low pass filter. The scaling factor or "DC" gain can be obtained by setting $q^{-1} = 1$ with the result:

$$\text{Scale Factor} = \frac{b}{1 - f} \tag{4.4-8}$$

The 3 dB bandwidth can be obtain by setting $q = e^{j\omega T}$ where T is the sampling interval, in the case of the OLYMPUS data $T = 0.1$ sec, and solving for the value of ω where the magnitude of (4.4-8) or (4.4-9) equals $1/\sqrt{2}$. The result is:

$$\text{BW (Hz)} = \frac{1}{2\pi T} \arccos\left(\frac{-f^2 + 4f - 1}{2f}\right) \tag{4.4-9}$$

Figure 4.4-3 is a gain/phase versus frequency plot of the composite average 1 second predictor. See Section 4.4-1 for a description of the composite average.

Amplitude and Phase Response
Composite one sec delay 20/30 GHz predictor filter
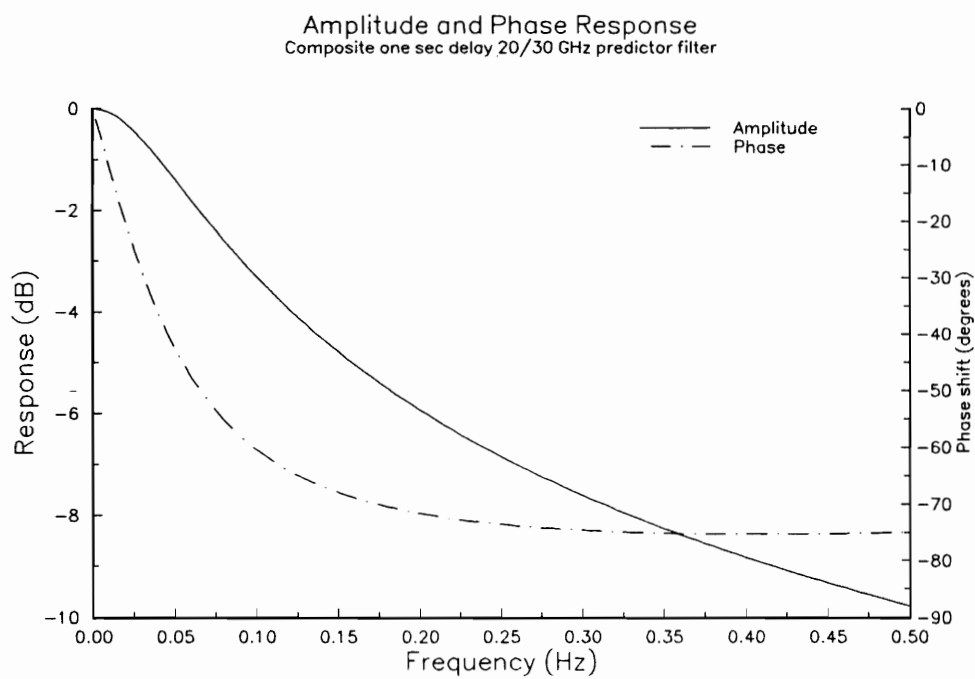
Figure 4.4-3: Gain/Phase plot for one second predictor.

4.5 TESTING THE ULPC ALGORITHM

4.5-1 Event Choice and Data Preparation

At the time this work began (summer of 1991), November 1990 and January to May 1991 data from the OLYMPUS experiment were available. The OLYMPUS satellite experienced operational difficulties and lost orbital stabilization on May 29, 1991. At the time of this failure, we decided to use the available data because the future of OLYMPUS was in serious doubt. Almost miraculously, the spacecraft was restored to operational status early in August of 1991.

The data collected from the experiment accumulates at approximately 0.6 megabyte/hour in an MS-DOS readable format. This is a massive amount of data and most of it represents relatively uninteresting clear air periods. The November 1990 and January to May 1991 data set was examined for "interesting events." Events for analysis were chosen on the basis of the following criteria:

- The events should be less than about four hours long. This way the data could be processed with MS-DOS type computers and stored on high density floppy disks. This limitation prevented the examination of long term receiver drift, diurnal, and atmospheric attenuation effects.

- The events should have relatively well defined starts and/or ends. The clear air reference levels were determined manually.

- The events should be "representative." The chosen events range from 3-4 dB events to intense thunderstorm events with attenuations greater than the measurement range of the receivers (38 dB).

The data set contains 26 events and 66 hours of data. No attempt was made to be exhaustive but the data set does represent a wide variety of events representing the conditions during winter, spring, and early summer in Blacksburg. Table 4.5-8 lists the chosen events.

The event data is taken from edited OLYMPUS data files [14]. The editing process marks those portions of data which are calibration marks, i.e. waveguide attenuator and noise diode radiometer calibrations, and out-of-lock periods. While data can be restored for some of these periods by interpolation, only actually measured beacon data were used for this work.

In addition, only those data which represented 30 GHz fades greater than 1 dB and less than 12 dB were used. Conditioning on 30 GHz fade may be somewhat unrealistic. In an actual system, the 30 GHz fade level is what is being estimated/predicted but conditioning on fades greater than 0.5 dB at 20 GHz would increase the effect of scintillations. In practice, this conditioning will be determined by system margins and the above conditioning was chosen in the absence of any firm data on system margins.

The analysis in Section 4.2 raises a number of questions that need to be addressed in order to produce a practical algorithm. Among them are: how will the scaling value vary from storm to storm? Is there some "optimum" scaling factor and what is lost by departing from this value? What is the effect of introducing delay into the algorithm to simulate control delays? How much filtering is "optimum"?

The Matlab function "oe" was run on each event using the 20 GHz attenuation to estimate or predict 30 GHz attenuation with delays of 0, 1, 5, 10, and 20 seconds. This simulates the output error model described above. The result is a value for f and b that is optimum in the MSE sense for each particular event and for each delay. These values of f and b should represent the best performance that is possible for the event. Table 4.5-1 lists f and b with the resulting scale factor and filter bandwidth for the November 5-6, 1990 2300-0200 UTC event.

A time weighted average of scaling factor and bandwidth was obtained for the entire event set. Table 4.5-2 contains these composite scale factors and bandwidths. The composite scale factor is approximately 1.93 for the no delay case. This is very close to the 1.97 statistical scale factor obtained by the CCIR

method of (4.2-1). Table 4.5-2 also contains the resulting composite values of f and b. Compare the composite results in Table 4.5-2 with the optimum scale factors and bandwidths for November 5-6 listed in Table 4.5-1.

Table 4.5-1: Optimum scaling factor, filter bandwidths, and filter parameters for 20 GHz scaled to 30 GHz for November 5-6, 1990 2300-0200 UTC event.

Delay (sec)	f	b	scale factor	BW(Hz)
			DC gain	
	20 GHz scaling to 30 GHz			
0	0.93478388	0.138450120	2.1229	0.10737
1	0.97001592	0.063647015	2.1227	0.04845
5	0.96810264	0.067591551	2.1190	0.05160
10	0.96701703	0.069715792	2.1137	0.05338
20	0.96500584	0.073617339	2.1037	0.05670

Table 4.5-2: Time weighted average composite scaling factor, filter bandwidth, and filter parameters for 20 GHz scaled to 30 GHz.

Delay (sec)	f	b	scale factor	BW(Hz)
			DC gain	
	20 GHz scaling to 30 GHz			
0	0.964469	0.068712	1.933824	0.057585
1	0.953196	0.090608	1.935922	0.076304
5	0.968684	0.060393	1.928515	0.050642
10	0.963156	0.070908	1.924546	0.059754
20	0.957177	0.082155	1.918475	0.069668

Karasawa and Matsudo [15] report that rain fades can be separated from scintillations by the use of 0.004 Hz lowpass filter. Depending on the event, the optimum filter bandwidths produced by the process described above range from 0.006 to 0.25 Hz. The weighted average bandwidth is 0.06-0.08 Hz. This is roughly a factor of 10 greater than that reported by Karasawa and Matsudo. What this work shows is that filters considerably broader than 0.004 Hz can be

used to separate rain fades from scintillations in some events. The broader filters have less delay and thus are more desirable for adaptive control.

4.5.2 ULPC Algorithm Tested on the November 5-6, 1990 Event

Once the optimum and composite scale factors and bandwidths were calculated, the ULPC algorithm was implemented on each event in the data set.

Figure 4.5-1 is the 30 GHz attenuation less than 12 dB for the November 5-6, 1990 2300-0200 UTC event. Figure 4.5-2 is the ULPC algorithm error for this event with the one second delay composite filter/scaler. A summery of algorithm performance for the entire event set is contained in Appendix 1.

Table 4.5-3 tabulates the overall algorithm performance when the 20 GHz downlink attenuation is scaled to the 30 GHz uplink for the November 5-6, 1990 event with composite filtering but no delay.

ULPC is activated when the 30 GHz attenuation exceeds 1 dB. Effectively there is 1 dB of 30 GHz margin. The control time is the length of time during which the ULPC can compensate for the uplink fade and it is assumed that the ULPC can compensate for 30 GHz fades up to 12 dB. This is somewhat greater than the 10 dB dynamic range limitation discussed in Section 4.2-3 but 12 dB was chosen to examine algorithm performance at fade extremes. A link outage will result when the 30 GHz attenuation exceeds 12 dB. A measure of improvement due to ULPC can be calculated from:

$$\text{Improvement} = \frac{\text{Time 1 dB} < \text{atten} < 12 \text{ dB}}{\text{Total time atten} > 1 \text{ dB}} \ 100\% \qquad (4.5\text{-}1)$$

Figure 4.5-2 plots the algorithm's error performance. It shows that the error is close to zero mean. Thus, the primary source of error is the scintillations. This also means that the scaling factor is relatively constant during the event. In addition, the difference between the value of the composite scaling factor and the value of the optimum scaling factor comparatively is small. This can be

confirmed by examining Tables 4.5-1 and 4.5-2.

Table 4.5-4 contains a more detailed look at algorithm performance. The RMS error is listed for various delays when the algorithm is implemented with CCIR scaling and no filtering, with scaling and filtering using the composite filter, and with scaling and filtering that are optimum for the event.

Table 4.5-4 also contains an error distribution which gives a measure of the algorithm's tendency to under or over predict. The various columns of Table 4.5-4 tabulate the number of 0.1 second periods where the difference between the 30 GHz attenuation estimate and the actual 30 GHz attenuation, $\widehat{A}_{30} - A_{30}$, falls within the specified error bin. Obviously, the less the spread, the lower the error.

Table 4.5-3: Outage improvement due to ULPC power control
for November 5-6, 1990 2300-0200 UTC.

20 GHz downlink estimating 30 GHz uplink with composite filtering and no delay
Control activated for uplink attenuation between 1 and 12 dB.
30 GHz attenuation greater than 12 dB results in an outage.

Total Time	Control Time	Outage Time	Improvement
Atten > 1 dB	1 dB < Atten < 12 dB	Atten > 12 dB	
(hr:min:sec)	(hr:min:sec)	(min:sec)	
2:39:10.5	2:23:56.4	15:14.1	90.43 %

30 GHz Attenuation
Nov. 5—6, 1990 2300—0200 UTC
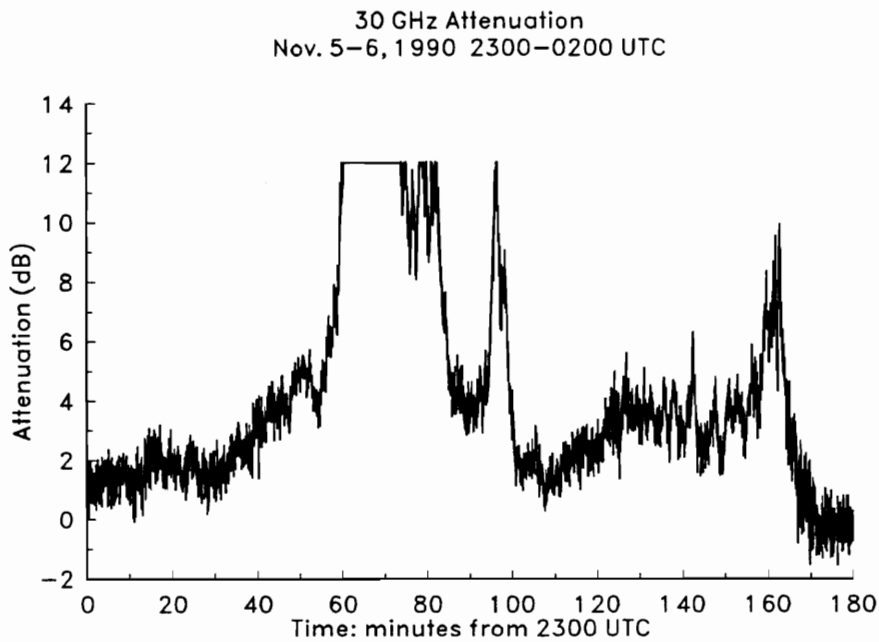
Figure 4.5-1: 30 GHz attenuation less than 12 dB for the November 5-6, 1990
event. Attenuation greater than 12 dB represents an outage.

Control Error: 20 GHz scaled to 30 GHz
Nov. 5—6, 1990 2300—0200 UTC
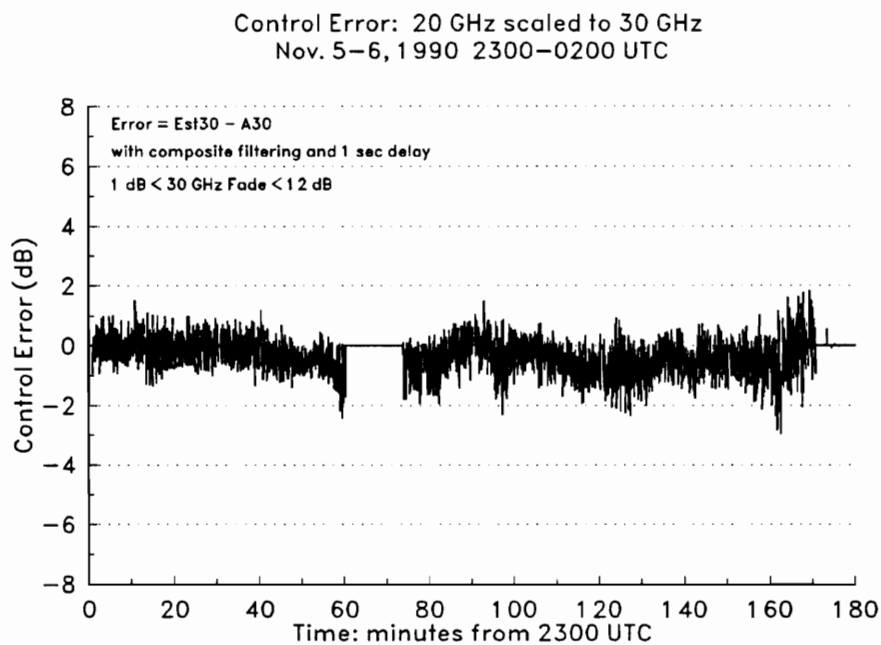
Figure 4.5-2: Control error: 20 GHz scaled to 30 GHz for November 5-6, 1990.

Table 4.5-4: Error distribution for ULPC driven by scaled
20 GHz downlink attenuation.

Delay sec	RMS Error	Error < 0 results from over prediction						Error > results from under prediction						
		Error bins: number of 0.1 sec period between dB limits												
		<-6	-6≤-5	-5≤-4	-4≤-3	-3≤-2	-2≤-1	-1≤1	1≤2	2≤3	3≤4	4≤5	5≤6	≥6
		(dB)	20 GHz CCIR scaled to 30 GHz: scale ratio = 1.97											
0	0.75	0	0	9	52	832	12051	71536	1799	81	4	0	0	0
1	0.75	0	0	3	46	772	11693	70921	1943	114	13	5	0	0
		20 GHz filtered, scaled to 30 GHz: Composite												
0	0.61	0	0	0	5	133	8287	77893	46	0	0	0	0	0
1	0.65	0	0	2	5	244	9537	75373	299	10	0	0	0	0
5	0.69	0	0	4	26	534	10911	72880	525	9	0	0	0	0
10	0.74	0	0	6	88	930	12063	70696	826	34	1	0	0	0
20	0.84	0	3	41	277	1714	13228	66570	1820	169	12	0	0	0
		20 GHz filtered, scaled to 30 GHz: Optimum												
0	0.44	0	0	0	0	15	1788	83885	675	1	0	0	0	0
1	0.51	0	0	0	3	48	2878	80908	1608	24	1	0	0	0
5	0.57	0	0	0	9	93	3785	78343	2563	96	0	0	0	0
10	0.64	0	0	0	26	263	5063	75491	3505	283	13	0	0	0
20	0.74	0	0	12	95	606	7187	70257	4866	681	119	11	0	0

4.5.3 Uplink Beacon ULPC

In February and March of 1992, the World Administrative Radio Conference (WARC-92) met in Torremolinos, Spain. It made a new allocation between 27.5 and 30 GHz for spacecraft uplink beacons [16]. This spectrum had been reserved for earth to space links. The OLYMPUS 30 GHz beacon at 29.656 GHz and the ACTS 27.505 GHz beacons fall in this new allocation.

This new beacon allocation permits uplink 30 GHz ULPC beacons on future K_A band satellites.   Such beacons should permit more accurate power control because there is no frequency scaling error if attenuation is measured at the uplink frequency. Since 30 GHz beacon attenuation in the WARC-92 allocation is already available from the OLYMPUS experiment program, it was possible for us to test this hypothesis.

The technique used in Section 4.5.1 for scaling downlink data was applied to the

measured uplink attenuation. The same event set was used and the Matlab function "oe" was run on each event. 30 GHz attenuation data was used to predict 30 GHz attenuation with delays of 1, 5, 10, and 20 seconds. For obvious reasons, the estimation case with no delay was deleted. The result is a value for f and b that is optimum in the MSE sense for each event and each delay. These values of f and b should represent the best performance that is possible for each particular event. Table 4.5-5 contains the optimum scaler and filter for the November 5-6, 1990, 2300-0200 UTC event.

A time weighted average for the scaling factor and the bandwidth was obtained for the entire event set. Table 4.5-6 contains the resulting composite scale factors and bandwidths with the corresponding filter parameters f and b. The scale factor is approximately 1.0 as expected. The bandwidths of these filters are approximately a factor of two greater than that of the filters used in scaling 20 GHz to 30 GHz. This may permit slightly faster response from uplink beacon driven ULPC but we did not feel the difference was significant.

The algorithm was run on the entire event set and the results for the November 5-6, 1990 are shown here. Table 4.5-3 still describes the outage performance. It is identical to the downlink scaled case because the same 1dB 30 GHz fade criteria was applied in testing 30 GHz uplink beacon driven ULPC. Figure 4.5-3 is a plot of the error performance. Because the scaling factor is always approximately 1.0, the error will always be zero mean for uplink beacon driven ULPC. Table 4.5-7 contains the error performance for both the composite and optimum filtering cases for the chosen delays.

Examining the RMS error in Table 4.5-7 reveals that there is little difference between the optimum and the composite filtering. In addition, the uplink beacon driven ULPC performance is consistently better than the scaled downlink ULPC performance listed in Table 4.5-4.

Table 4.5-5: Optimum scaling factor, filter bandwidths, and filter parameters for 30 GHz predicting 30 GHz for the November 5-6, 1990 2300-0200 UTC event.

Delay (sec)	f	b	scale factor DC gain	BW(Hz)
1	0.94618938	0.053760354	0.999067	0.08806
5	0.93548754	0.064361910	0.997666	0.10618
10	0.92603685	0.073636558	0.995584	0.12236
20	0.93164289	0.067673649	0.990002	0.11274

Table 4.5-6: Composite filter parameters
Time weighted average scaling factor, filter bandwidth, and filter parameters for 30 GHz prediction 30 GHz for entire data set.

Delay (sec)	f	b	scale factor DC gain	BW(Hz)
30 GHz predicting 30 GHz				
1	0.913108	0.086802	0.998965	0.144773
5	0.944366	0.055533	0.998182	0.091128
10	0.933525	0.066190	0.995710	0.109523
20	0.921405	0.078053	0.993109	0.130350

Control Error: 30 GHz predicting 30 GHz
Nov. 5-6, 1990 2300-0200 UTC
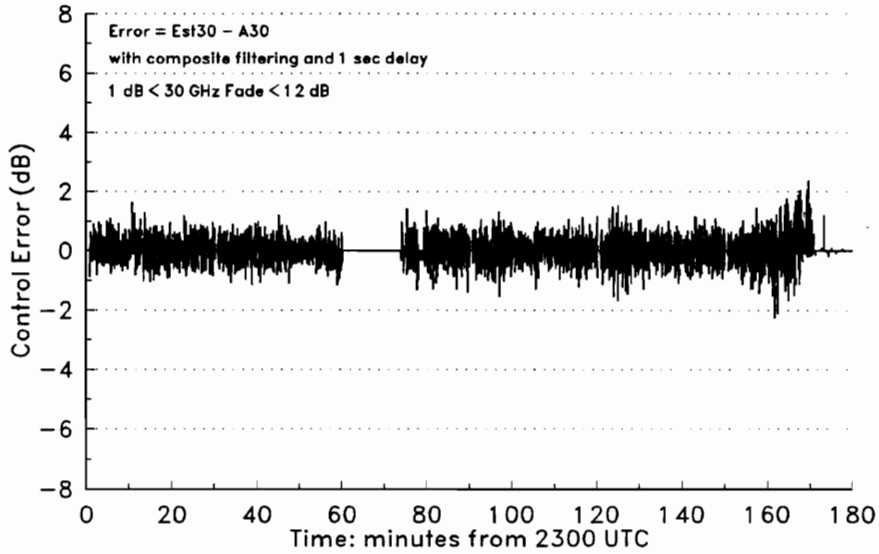
Figure 4.5-3: Control error: 30 GHz predicting 30 GHz for November 5-6, 1990. Event attenuation is plotted in Figure 4.5-1.

Table 4.5-7: Error distribution for ULPC driven by
30 GHz uplink beacon attenuation.

Delay sec	RMS Error	Error < 0 results from over prediction							Error > results from under prediction						
		Error bins: number of 0.1 sec period between dB limits													
		<-6	-6≤-5	-5≤-4	-4≤-3	-3≤-2	-2≤-1	-1≤1	1≤2	2≤3	3≤4	4≤5	5≤6	≥6
	(dB)	30 GHz predicting 30 GHz: Composite												
1	0.40	0	0	0	0	16	728	83774	951	35	6	0	0	0
5	0.46	0	0	0	0	31	1295	81981	1714	62	2	0	0	0
10	0.53	0	0	0	12	125	2326	79656	2723	180	3	0	0	0
20	0.68	0	0	7	59	576	3997	74670	4660	579	67	0	0	0
		30 GHz predicting 30 GHz: Optimum												
1	0.40	0	0	0	0	15	701	83819	933	36	6	0	0	0
5	0.46	0	0	0	0	32	1315	81995	1681	60	2	0	0	0
10	0.53	0	0	0	12	124	2336	79641	2732	177	3	0	0	0
20	0.68	0	0	7	69	608	4090	74689	4545	544	63	0	0	0

4.5.4 Overall Algorithm Performance

Table 4.5-8 contains the RMS error with one second delay for all the events in the data set. Using this table, it is possible to compare the performance of downlink scaled attenuation ULPC and uplink attenuation driven ULPC with either optimum or composite scaling and filtering.

The optimum scaling and filtering is almost always as good or better than the composite. This should be the case if the "optimum" is truly optimum. The May 6, 1991 event seems to be an exception. The RMS error with composite filtering for the May 6, 1991 event with 5, 10, and 20 second delays is slightly lower than the "optimum" case! Claiming to have found the absolute "optimum" when working with real data can be a somewhat hazardous occupation.

The Matlab "oe" function is iterative and it was run until further improvement was less than 0.01%. However given the severity of this event and the iterative nature of oe, it is difficult to know if the "optimum" values are truly optimum. Another possible explanation might be found in the manner in which the outage points are handled in the delayed cases. Those points with greater than 12 dB attenuation were simply removed from the data processed by Matlab. In the ULPC algorithm, any point with an estimated or predicted attenuation greater than 12 dB was counted as an outage point even if the actual attenuation did not exceed 12 dB. In any event, the difference is small and the May 6th event was the only one to show this quirk.

A weighted average error for the entire event set was calculated for each of the various scaling and filtering options and it is tabulated at the bottom of Table 4.5-8. The unfiltered scaling with the CCIR factor produced the poorest performance with 1.13 dB RMS error for the event set. The composite scaling with filtering improved algorithm performance to 1.02 dB RMS. This is a worthwhile improvement.

Since the scaling factor for the CCIR scaling without filtering is 1.97 and the composite scaling factor with filtering is 1.93, it is possible to compare these two

Table 4.5-8: Summery of RMS error (dB) with 1 second delay.

| Event Date | Time (UTC) | 20 GHz scaled to 30 GHz | | | 30 GHz predicting 30 GHz | | Error Type |
		CCIR scaling (dB)	Composite filter (dB)	Optimum filter (dB)	Composite filter (dB)	Optimum filter (dB)	
Nov. 5-6, 1990	2300-0200	0.75	0.65	0.51	0.40	0.40	1
Nov. 10, 1990	1100-1300	0.85	0.62	0.55	0.62	0.56	3
Nov.17,1990	0500-0700	0.43	0.36	0.35	0.36	0.35	1
Nov. 23, 1990	0700-0900	1.18	1.11	0.59	0.21	0.20	2
Nov. 28, 1990	2000-2100	1.24	0.88	0.86	0.93	0.90	2
Jan. 7, 1991	1500-1600	0.62	0.70	0.39	0.23	0.23	3
Jan. 8, 1991	2200-2400	0.67	0.49	0.48	0.34	0.32	3
Jan. 20, 1991	0500-0900	1.42	1.32	0.35	0.14	0.14	2
Feb.6, 1991	1100-1500	0.84	0.73	0.28	0.18	0.18	2
Feb. 7, 1991	0600-1000	0.76	0.69	0.68	0.44	0.43	1
Mar. 3, 1991	2100-2400	0.70	0.56	0.52	0.35	0.34	1
Mar 7, 1991	0000-0300	1.92	1.95	1.55	0.32	0.32	2
Mar. 22, 1991	1100-1300	0.91	0.76	0.49	0.47	0.47	2
Mar. 26, 1991	2000-2300	1.98	1.83	0.57	0.22	0.22	2
Apr. 5, 1991	1300-1500	0.60	0.55	0.51	0.22	0.22	3
Apr. 8, 1991	2000-2300	0.79	0.75	0.60	0.55	0.54	3
Apr. 9, 1991	0400-0600	0.74	0.77	0.48	0.49	0.49	3
Apr. 9-10,1991	2200-0200	1.66	1.56	1.46	0.80	0.79	3
Apr. 15, 1991	0800-1000	1.19	1.11	1.09	0.48	0.48	3
Apr. 24, 1991	1200-1500	0.94	0.75	0.72	0.69	0.67	1
Apr. 30, 1991	0200-0400	1.95	1.82	1.17	0.35	0.34	3
May 6, 1991	1700-1900	1.51	1.02	1.00	1.18	1.16	1
May 12, 1991	1900-2200	1.74	1.57	1.48	0.61	0.61	3
May 14, 1991	2000-2200	1.50	1.24	0.98	0.74	0.74	1
May 19, 1991	1300-1600	0.91	0.96	0.33	0.20	0.20	3
May 21, 1991	0700-0900	0.83	0.79	0.53	0.33	0.28	1

Weighed mean RMS error: 1.1286   1.0170   0.7214   0.4394   0.4288 (dB)

Error Type: 1: Error primarily due to failure to follow scintillations

2: Error primarily caused by bias due to incorrect scaling factor.
The optimum and composite scaling factors are
significantly different.

3: Error primarily due to variation in scale factor during event

cases to assess the value of filtering. In all events except for January 7th, March 7th, and April 9th, filtering improved algorithm performance. Nevertheless, the CCIR derived scale factor with no filtering is only marginally better for these three events.

The 0.72 dB RMS error for the optimum scaling and filtering is clearly better than the composite scaling and filtering. The average performance of 1.02 dB for the composite shows that there is a penalty to be paid for the convenience of a single valued algorithm. In the absence of a breakthrough which will allow real time characterization of each storm, it appears that this penalty must be endured.

If better ULPC performance is desired, prediction using the uplink beacon clearly has the edge. The composite filtered 30 GHz uplink beacon ULPC resulted in only 0.44 dB of RMS error. The optimum filter resulted in only a marginal increase in performance to 0.43 dB RMS, so finding the optimum filter for the 30 GHz uplink beacon is not as critical as in the scaling case. The use of an uplink beacon does not always guarantee better performance, however. An examination of the composite scaling performance for the November 10, November 17, November 28, and May 6 events reveals that 20 GHz scaled to 30 GHz performed as well or better than the uplink beacon driven algorithm.

The last column in Table 4.5-8 lists the error type for 20 GHz scaled to 30 GHz. Examination of the plots of control error shows there are basically three different sources of error for the composite scaling and filtering case. As noted for November 5-6, 1990 event in Figure 4.5-2 above, the majority of error is due to scintillations.

Some events will show a clear bias when the composite scale factor is much removed from the optimum. These events are designated type "2" in Table 4.5-8. Such an event is shown in Figure 4.5-4. The optimum scale factor for this event is 1.31, and it had the lowest scale factor of any event in the data set. The composite scale factor is 1.93, so using this factor will result in the algorithm over predicting the attenuation. The March 7, 1991 event has an optimum

scaling factor of 2.5 which is the highest factor of any event in the set. The composite algorithm under predicted for this event. This can be seen in Figure 4.5-5 which is a plot of the control error for the March 7, 1991 event.

Figure 4.5-6 plots the average scaling factor versus 20 GHz attenuation for all of the event time between January 1991 and May 1991. Figure 4.5-6 shows that scaling factor is less than approximately 2.5 for 90% of the time and it is less than approximately 1.5 for only 10% of the time. Thus, the maximum and minimum scale factors of 2.5 and 1.31 represent the maximum and minimum not only for the chosen event set, but the entire period as well. Figure 4.5-6 also shows that the scale factors tend to decrease as the attenuation increases. This is consistent with the analysis in Section 4.2.

Finally, in some events the scale factor changes during the event. The scaling factor is not constant during the event. An example of the effect is the April 15, 1991 event in Figure 4.5-7. This event is designated type "3" in Table 4.5-8. The optimum scale factor for this event is 1.85 which is not far removed from the 1.93 composite scale factor, but during part of the event the composite scaling under predicted and during another part of the event it over predicted.

This change during the event suggests that the analysis of Section 4.2 may be somewhat simplistic in implying that the drop size distribution does not change for attenuations less than 6 dB at 20 GHz. However, these changes do not appear to be great enough to prevent downlink scaled attenuation from driving an ULPC algorithm successfully.

Control Error: 20 GHz scaled to 30 GHz
Jan. 20, 1991   0500−0900 UTC

Error = Est30 − A30

with composite filtering and 1 sec delay

1 dB < 30 GHz Fade < 1 2 dB

Control Error (dB)

Time: minutes from 0500 UTC
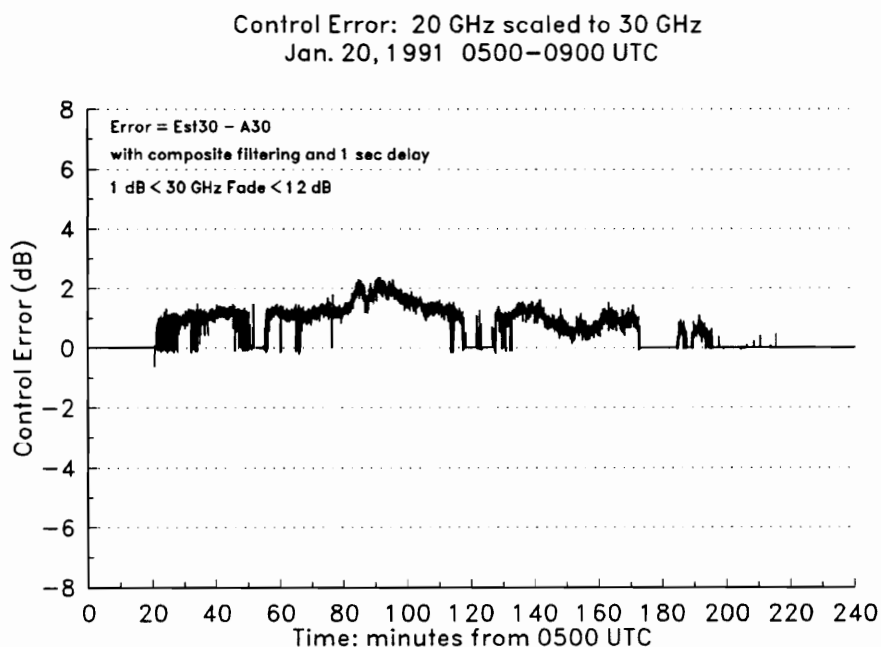
Figure 4.5-4: Control error for the January 20, 1991 event. The bias toward over prediction is a result of the using the composite scale factor of 1.93 rather than the optimum scale factor of 1.31, the lowest scale factor in the event set.

Control Error: 20 GHz scaled to 30 GHz
Mar. 7, 1991   0000–0300 UTC

Error = Est30 − A30
with composite filtering and 1 sec delay
1 dB < 30 GHz Fade < 1 2 dB
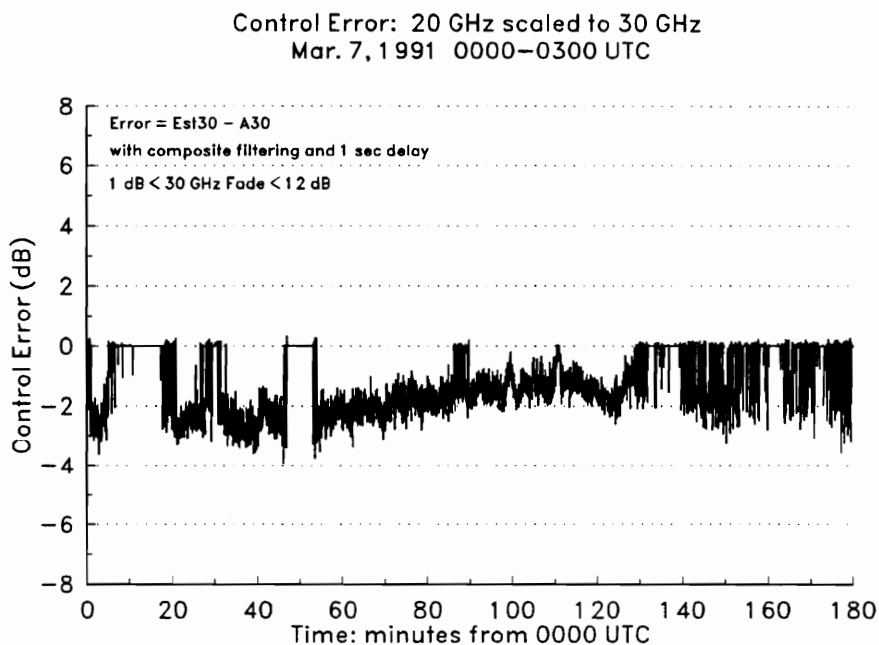
Figure 4.5-5: Control error for the March 7, 1991 event. The bias toward under prediction is a result of the using the composite scale factor of 1.93 rather than the optimum scale factor of 2.50, the highest scale factor of in the event set.

30 GHz / 20 GHz Attenuation Ratio
Occurences for January to May 1991
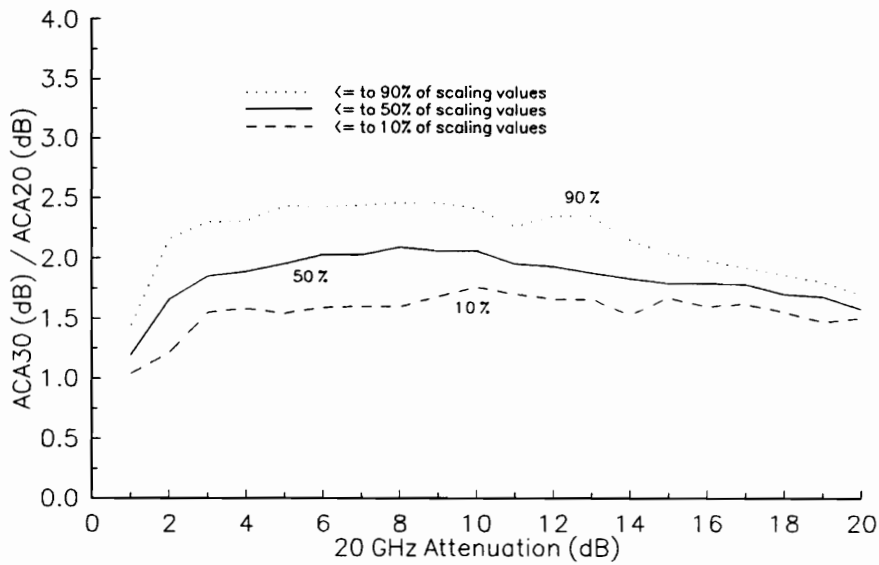
Figure 4.5-6: Average scaling factor versus 20 GHz attenuation for the entire period from January 1991 to May 1991.

Control Error: 20 GHz scaled to 30 GHz
April 15, 1991 0800–1000 UTC
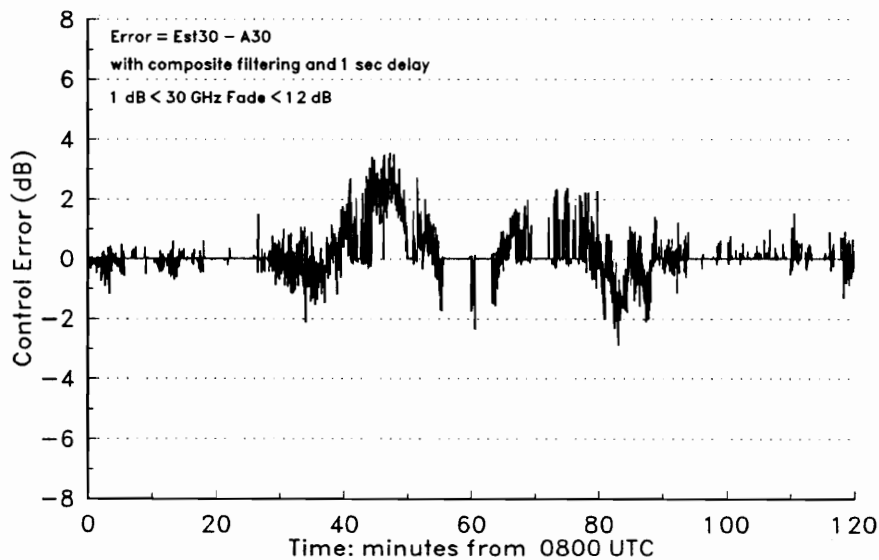
Figure 4.5-7: April 15, 1991 event showing scale factor change during the event.

4.5.5 Step Control of ULPC Algorithm

The ULPC algorithms described by (4.4-6) and (4.4-7) provide a continuous estimate/prediction for uplink attenuation. In an actual system it may not be possible or desirable to vary the uplink transmitter power continuously.

Radio frequency step attenuators are available in a wide variety of configurations and a computer controlled step attenuator in a transmitter intermediate frequency stage would be a convenient and inexpensive method for implementing power control. Such a system, however, will not be as accurate as continuous control. How much is lost by using step control?

This question was investigated by rounding the estimate/prediction to an integer dB value before the error was calculated. This simulates a power control system operating with a step attenuator having 1 dB steps.

Step control produces RMS errors identical to those of Tables 4.5-4 and 4.5-7 for the continuous control case. There is a slight change in the error distribution but there appears to be no performance penalty for using step control.

4.5.6 Summary and Conclusions of the ULPC experiment

The observed variations in scaling factor appear to be due to changes in the drop size distribution during a storm, but ULPC can be implemented with scaled downlink attenuation data if the dynamic range of the power control is limited to approximately 10 dB. The observed scaling factor for a number of events is relatively constant for most storms, but there appears to be significant differences in real time scaling factor from storm to storm despite the fact that the average observed scaling factor of 1.93 agrees closely with the 1.97 CCIR derived statistical scaling factor.

Water vapor and oxygen attenuation do not appear to be significant factors, although this bears additional study due to the potentially large error caused by water vapor attenuation. Because of the separate antennas used in the Virginia

Tech OLYMPUS experiment, it was not possible to compensate for scintillations. This is not a significant limitation because scintillations become decorrelated as ULPC control delay increases. Since it was not possible to compensate for scintillations, a simple IIR lowpass smoothing filter was implemented.

Twenty six events totaling 66 hours of attenuation data were examined. Optimum scaling factors and filter bandwidths were calculated for each event and a time weighted average scale factor and bandwidth were calculated for the event set.

Filtering improved the algorithm performance in almost all cases but there was some loss of performance due to use of the composite scaling factor. The type of error varied from event to event. Some events suffered more from incorrect scaling while scintillation was a major source of error in others.

In addition to scaled downlink attenuation data, a simulated 30 GHz uplink beacon was used to drive the ULPC algorithm. The 30 GHz beacon driven ULPC offers significantly better performance than scaled downlink attenuation driven ULPC.

4.6 REFERENCES

[1] Boithias, Lucien, "Similitue en frequence pour l'affaiblissement par la pluie," Ann. Telecommun., 44, No. 3-4, 1986, pp. 186-191.

[2] "Attenuation by Hydrometeors, in Particular Precipitation, and Other Atmospheric Particles," CCIR Report 721-3, Propagation in Non-Ionized Media, Vol. 5, ITU, Geneva, 1990.

[3] Ortgies, G, F. Rucker, F. Dintelmann, "Some Aspects of Attenuation Frequency Scaling," Proceedings of the URSI Commission F symposium on Microwave Propagation, London, Ontario, Canada, June 1991, p. 450.

[4]   Olsen, Roderic L, David V. Rodgers, and Daniel B. Hodge, "The aR^b Relation in the Calculation of Rain Attenuation," <u>IEEE</u> <u>Transactions</u> <u>on</u> <u>Antennas</u> <u>and</u> <u>Propagation</u>, Vol. AP-26, No. 2, March 1978, pp 318-329.

[5]   J. Joss, J.C. Thams, and A. Waldvogel, "The variation of raindrop size distributions at Locarno," <u>Proceedings</u> <u>of</u> <u>the</u> <u>International</u> <u>Conference</u> <u>on</u> <u>Cloud</u> <u>Physics</u>, 1968, pp. 369-373.

[6] Battan, Louis J., <u>Radar</u> <u>Observation</u> <u>of</u> <u>the</u> <u>Atmosphere</u>, The University of Chicago Press, Chicago, 1973, pp. 90-92.

[7]   "Attenuation by Atmospheric Gasses", <u>Propagation</u> <u>in</u> <u>Non-Ionized</u> <u>Media</u>, CCIR Report 719-3, Vol. 5, ITU, Geneva, 1990.

[8]   Ihara, T. and Y. Furuhama, "Frequency scaling of rain attenuation at centimeter and millimeter waves using a path-averaged drop size distribution," <u>Radio</u> <u>Science</u>, Vol. 23, No. 3, May 1988, pp. 1365-1372.

[9]   "Effects of Small-Scale Spatial or Temporal Variations of Refraction on Radiowave Propagation", <u>Propagation</u> <u>in</u> <u>Non-Ionized</u> <u>Media</u>, CCIR Report 881, Vol. 5, ITU, Dubrovnik, 1986.

[10] Ljung, Lennart, <u>System</u> <u>Identification:</u> <u>Theory</u> <u>for</u> <u>the</u> <u>User</u>, Prentice-Hall, Inc., Englewood Cliffs, NJ, 1987, Chapter 3.

[11] Ljung, Lennart, <u>System</u> <u>Identification</u> <u>Toolbox:</u> <u>MATLAB</u> <u>Users</u> <u>Guide</u>, The MathWorks, Inc., Natick, MA, 1992, pp. 2-63 - 2.-65.

[12] Jackson, Leland B., <u>Digital</u> <u>Filters</u> <u>and</u> <u>Signal</u> <u>Processing</u>, Kluwer Academic Publishers, Boston, 1986.

[13] Ljung, Lennart, <u>System</u> <u>Identification</u> <u>Toolbox:</u> <u>MATLAB</u> <u>Users</u> <u>Guide</u>, The MathWorks, Inc., Natick, MA, 1992, pp. 2-27 - 2.-28.

[14]   Sylvester, William R., Jr., "Olympus Propagation Data Preprocessing Software,"   Virginia Tech Report EESATCOM Report 91-6, JPL Contract #958435, November 1991, pp. 19-22.

[15] Karasawa, Yoshio and Takashi Matsudo, "Characteristics of Fading on Low-Elevation Angle Earth-Space Paths with concurrent Rain Attenuation and Scintillation," IEEE Transactions on Antennas and Propagation, Vol. AP-39, No. 5, May 1991, pp. 657-661.

[16] Flock, W. L. and E. K. Smith, "WARC 92 and Some Thoughts as to its Impact on the NASA Propagation Program," and A. O. Heyward, "Allocations by the 1992 World Administrative Radio Conference," Proceedings of the Sixteen NASA Propagation Experimenters Meeting (NAPEX XVI) and the Advanced Communications Technology Satellite (ACTS) Propagation Studies Miniworkshop, Houston, Texas, May 29-30, 1992, pp. 116-131.

CHAPTER 5:   NON-LINEAR MODELS AND ADDITIONAL TOPICS

5.1 INTRODUCTION: DEAD ENDS AND NEW PATHS

It has been said that the function of basic research is to determine that blind alleys are blind [1]. This work has had its share of blind alleys. The purpose of this chapter is to mark some of those blind paths and suggest some new ones to explore.

It is possible to scale attenuation from two different frequencies to estimate attenuation at a third. We investigated this "two-frequency" scaling as well as scaling which employed a non-linear relation. Neither algorithm showed much promise. A non-linear neural net algorithm was investigated. It showed more promise, but implementation difficulties must be overcome before its full potential can be explored. This is an area for additional work.

The ACTS program offers additional research opportunities. A real time ULPC test has been proposed for ACTS, and the ACTS propagation terminal offers the opportunity to revisit radiometer driven ULPC.

Two system calibration ideas are proposed to overcome the problem of long term baseline drift in open-loop ULPC systems.

5.2 NON-LINEAR AND TWO-FREQUENCY ALGORITHMS

5.2.1 Two-Frequency Scaling Algorithms

Throughout this work "one-frequency" frequency scaling has been employed. Attenuation at one frequency is scaled to another, but there is some evidence that "two-frequency" scaling may result in greater accuracy [2]. Such a scaler has the form:

$$\widehat{A}_{30} = \alpha + \beta A_{20} + \gamma A_{12} \tag{5.2-1}$$

Where $\widehat{A}_{30}$ is the estimate of 30 GHz attenuation given the 12.5 GHz attenuation, A_{12}, and the 20 GHz attenuation, A_{20}. β and γ are the scaling coefficients. α is an offset, and typically $\alpha = 0$. This is simple scaling with no filtering.

The simultaneously measured values of 12.5, 20, and 30 GHz attenuation available from the OLYMPUS experiment were used to test this algorithm. One hour of data beginning at 0000 UTC on November 6, 1990 was used for the test. Coefficients α, β, and γ were obtained by linear regression. The results are listed in Table 5.2-1. Note that $\alpha \neq 0$ because there is a fixed offset in the original data. If the clear air reference levels are subtracted from the data then $\alpha \approx 0$. This test and the data preparation are described in more detail in [3].

Table 5.2-1 shows that there is little performance advantage with two-frequency scaling. This is not inconsistent with the work reported in [2]. In addition, the 12.5/20/30 GHz attenuation data are unique to OLYMPUS, so we decided that the two-frequency scaling algorithm was not worth developing.

Table 5.2-1: Performance of one and two frequency linear and non-linear scalers

Type Beacon	α	β	γ	RMS error (dB)
Linear 20	-92.1	2.093	0	0.86
Linear 20, 12	-126.4	1.870	0.617	0.85
Log 20	-5.59	2.26	0	0.91
Log 20, 12	-7.47	2.05	0.64	0.90

5.2.2 Non-Linear Scaling Based on aR^b Relationships

Commonly used estimators of attenuation are not linear. They are based on the assumption of a homogeneous rainfall with a known drop size distribution (DSD). Attenuation can be approximated from this DSD and the rain rate [4]:

$$A_i = a_i \, R^{b_i} \, L \tag{5.2-2}$$

where R is the effective rain rate, L is the effective path length, and a_i and b_i are parameters determined by curve fitting at the frequency i. The analysis in Section 4.2 is based on relationships similar to (5.2-2).

Using (5.2-2) a one-frequency scaling relation can be obtained:

$$\widehat{A}_{30} = a_{30} \left(\frac{A_{20}}{a_{20}} \right)^{b_{30}/b_{20}} \tag{5.2-3}$$

The same technique can be used to scale two frequencies. This is known as the method of Hogg [2][5]:

$$\widehat{A}_{30} = a_{30} \left(\frac{A_{20}a_{12}}{A_{12}a_{20}} \right)^{b_{30} - b_{20}/b_{20} - b_{12}} \tag{5.2-4}$$

The estimates of (5.2-3) and (5.2-4) are of the general form:

$$\widehat{A}_{30} = c \, A_{20}^a \, A_{12}^b \tag{5.2-5}$$

Equation (5.2-5) can be expressing in logarithmic form as:

$$\ln(\widehat{A}_{30}) = \ln(c) + a \ln(A_{20}) + b \ln(A_{12}) \tag{5.2-6}$$

$$= \alpha + \beta \ln(A_{20}) + \gamma \ln(A_{12})$$

This is linear relation and linear regression techniques can be used to obtain α, β, and γ for a minimum squared error estimate for $\ln(\widehat{A}_{30})$. This can be exponentiated to obtain $\widehat{A}_{30}$. It should be noted that (5.2-6) does not give a minimum squared error estimate for $\widehat{A}_{30}$.

The estimator of (5.2-6) was tested with the same data test used to test the linear estimator of (5.2-1). Table 5.2-1 tabulates the result. The non-linear estimators did not perform as well as the linear estimators and two frequency non-linear scaling offers no significant advantage over one frequency non-linear scaling. Both the log and linear estimators were tested on several more of the cataloged November 1990 events but in no instance was the non-linear estimator better than the linear one and further work was abandoned.

5.3 NEURAL NETWORKS FOR ATTENUATION ESTIMATION

5.3.1 Introduction to Neural Networks

It is clear that there is no well defined relationship between 20 and 30 GHz attenuation. Simple scaling and filtering were chosen more for their ease of implementation rather than their accurate description of the physical phenomenon. The question remains: is there a better relationship? Neural networks were investigated in an effort to find such a relationship.

Neural networks are loosely patterned after the central nervous system of living organisms. They are algorithms for cognitive tasks such as learning and optimization. The neural net can be "taught" the relationship between inputs and outputs even if this relationship is not explicitly known, and it could be taught the relationship between 20 and 30 GHz attenuation from the available data. A neural net can take the form shown in Figure 5.3-1 [2].
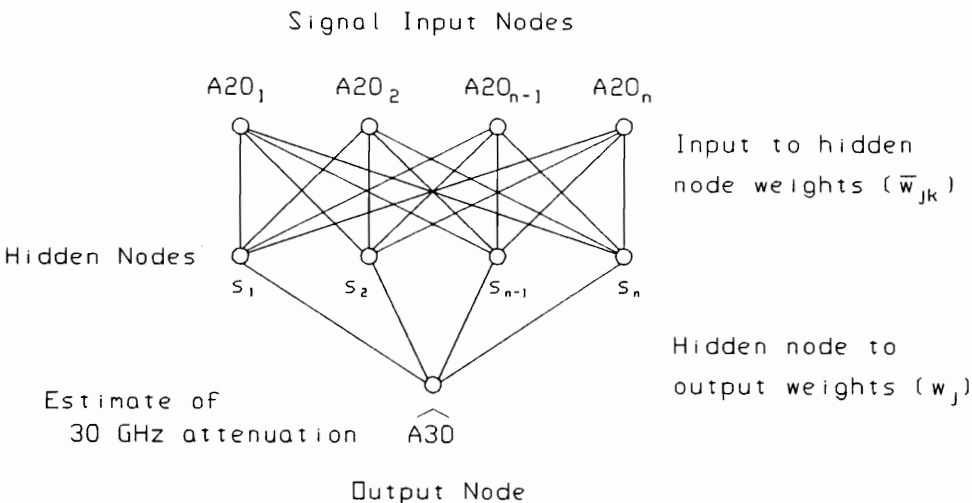
Figure 5.3-1: Neural net structure.

The output, $\widehat{A}30$, which is an estimate of the the 30 GHz attenuation is given by:

$$\widehat{A}30 = f_1(h) \qquad h = \sum_j w_j s_j - \theta \qquad (5.3\text{-}1)$$

w_j : j^{th} hidden to output node connection weights
s_j : strength of jth hidden node
θ : adjustable threshold
$f_1(h)$: hidden to output node function

The weights can be thought of as gains or scaling factors. The function $f_1(h)$ was chosen to be a linear function so $\widehat{A}30$ is a linear combination of hidden node s_j values, thus:

$$\widehat{S}30 = \sum_j w_j s_j - \theta \qquad (5.3\text{-}2)$$

The value of s_j which is the output of the jth hidden node is given by:

$$s_j = f_2(\overline{h}_j) \quad \overline{h}_j = \sum_k \overline{w}_{jk} S20_k - \overline{\theta}_j \qquad (5.3\text{-}3)$$

$S20_k$: value of 20 GHz attenuation at input node k
$\overline{w}_{jk}$: weight or gain from the kth input node to the jth hidden node
$\overline{\theta}_j$: j^{th} hidden node adjustable threshold
$f_2(\overline{h}_j)$: nonlinear "squashing" function

The function f_2 can be any nonlinear function. Historically, a number of common functions have been used [6]:

$$f_2(h) = \text{sgn}[h] \qquad (5.3\text{-}4)$$

$$f_2(h) = \frac{1}{(1 + e^{-2\beta h})} \qquad (5.3\text{-}5)$$

$$f_2(h) = \tanh(\beta h) \qquad (5.3\text{-}6)$$

Function (5.3-4) is a discrete state function where $f_2 = +1$ for $h > 0$ and $f_2 = -1$ for $h < 0$. Both (5.3-5) and (5.3-6) are continuous functions. Equation (5.3-5) is referred to as the Fermi function and its output ranges from zero to $+1$ for inputs from $-\infty$ to ∞, while (5.3-6) is an odd function whose output ranges from -1 to $+1$ for inputs from $-\infty$ to ∞.

A measure of the net's performance can be obtained by summing the squared error for all the values of 30 GHz attenuation:

$$D[w_j,\ \theta,\ \overline{w}_{jk},\ \overline{\theta}_j] = \tfrac{1}{2}\sum_\mu [A30_\mu - \widehat{A}30_\mu]^2 \tag{5.3-7}$$

where μ is all the possible values of actual 30 GHz attenuation, $A30$. The object is to choose the values of w_j, θ, $\overline{w}_{jk}$, $\overline{\theta}_j$ so that D is minimized. This is the familiar minimum squared error criteria.

$D[w_j,\ \theta,\ \overline{w}_{jk},\ \overline{\theta}_j]$ forms a multidimensional surface which ideally should have a global minimum. One way to find the minimum would be to apply Newton's method to (5.3-7), but Newton's method is computationally intense. The simpler method of steepest descent can be employed instead. A parameter, x_n, is adjusted for minimum squared error according to:

$$x_{n+1} = x_n - \epsilon \nabla f(x_n) \tag{5.3-8}$$

where ϵ is a "gain" or learning rate parameter. The choice of the learning rate parameter is somewhat subjective. It should not be so large that the correction for x_n causes it to overshoot the desired value. The result is the value of x will oscillate. On the other hand, ϵ should not be so small that x never converges to a final value.

It is a fairly easy task to obtain the gradient of (5.3-7) so the method of steepest descent was employed. A correction δ for the weights w_j is given by:

$$\delta w_j = -\epsilon \frac{\partial D}{\partial w_j} = \epsilon \sum_\mu [\widehat{S}30_\mu - f_1(h_\mu)]\, f_1'(h_\mu)\, \frac{\partial h_\mu}{\partial w_j} \tag{5.3-9}$$

Before proceeding, it is possible to simplify (5.3-9) by noting that:

$$[\widehat{S}30_\mu - f_1(h_\mu)] = \triangle_\mu = \text{Error}$$

and due to the choice of $f_1(h)$ in (5.3-2):

$$f_1'(h_\mu) = 1$$

$$\frac{\partial h_\mu}{\partial w_j} = s_j$$

so (5.3-9) becomes:

$$\delta w_j = \epsilon \sum_\mu \triangle_\mu s_j \qquad (5.3\text{-}10)$$

In the same way a correction can be applied to the threshold, θ:

$$\delta\theta = -\epsilon\frac{\partial D}{\partial\theta} = \epsilon \sum_\mu [\widehat{S}30_\mu - f_1(h_\mu)] \, f_1'(h_\mu) \, \frac{\partial h_\mu}{\partial\theta_j} \qquad (5.3\text{-}11)$$

Noting from (5.3-2) that $\frac{\partial h_\mu}{\partial\theta} = 1$, then (5.3-11) becomes:

$$\delta\theta = \epsilon \sum_\mu \triangle_\mu \qquad (5.3\text{-}12)$$

The correction for the $\overline{w}_{jk}$ weight is given by:

$$\delta\overline{w}_{jk} = -\epsilon \, \frac{\partial D}{\partial\overline{w}_{jk}} = \epsilon \sum_\mu [\widehat{S}30_\mu - f_1(h_\mu)] \, f_1'(h_\mu) \, \frac{\partial h_\mu}{\partial s_j} \, \frac{\partial s_j}{\partial\overline{w}_{jk}}$$

$$= \epsilon \sum_\mu \triangle_\mu \, w_j \, f_2'(\overline{h}_j) \, S20_k \qquad (5.3\text{-}13)$$

and the correction for the threshold $\overline{\theta}_j$ is:

$$\delta\overline{\theta}_j = -\epsilon \frac{\partial D}{\partial \overline{\theta}_j} = \epsilon \sum_{\mu} [\widehat{S}30_{\mu} - f_1(h_{\mu})] \, f_1'(h_{\mu}) \, \frac{\partial h_{\mu}}{\partial s_j} \frac{\partial s_j}{\partial \overline{\theta}_j}$$

$$= -\epsilon \sum_{\mu} \Delta_{\mu} \, w_j \, f_2'(\overline{h}_j) \tag{5.3-14}$$

One now "teaches" the net by starting with an initial estimate for the weights and the thresholds, calculating the error between the net estimate and the actual 30 GHz attenuation, and then correcting the weights according to (5.3-10) and (5.3-13) until the error function D goes to zero. The same is done with thresholds θ and $\overline{\theta}_j$ with (5.3-12) and (5.3-14) if the thresholds are used. This process is referred to as error back propagation.

The one serious limitation with this process is that there is no guarantee that unique values exist for the weights or thresholds. There is no guarantee that the net will converge to any set of weights or offsets. The choice of initial values and learning rates must be made arbitrarily and if convergence does occur, it is usually slow. "Teaching" the net tends to be computationally intense.

5.3.2 Test Net

Using the principles outlined in Section 5.3.1, a test net was implemented. Tanh(h) was chosen for $f_2(h)$ because it is a continuous function with a continuous derivative and its ± 1 output can easily be scaled to any level. Appendix 2 contains a program listing and operating instructions for this test net.

It has already been determined that $A30 \simeq 2 \times A20$, so a test data file of 200 points of $0 \leq A20 \leq 14$ dB and $A30 = 2 \times A20$ was created to test the net. The data was circulated through the net in the learning mode 100 times. Each pass through the net should result in lower error, so RMS error was monitored during learning in order to insure convergence. After "learning," the net weights were fixed and the data were run through the net in the operating mode. The resulting

Figure 5.3-2. Figure 5.3-2 shows that the net can learn the input/output relationship and, as expected, increasing the number of nodes decreased the RMS error.

It should be noted that this simple result required quite a bit of "tweaking" in order to obtain reliable convergence. The learning rate was set empirically and convergence is fairly sensitive to the learning rate. The learning rate for the $\overline{w}_{jk}$ weights need to be much smaller than learning rate for the w_j weights. The thresholds θ and $\overline{\theta}_j$ were not needed and so they were removed to reduce the computation required.

Choosing the initial values of $\overline{w}_{jk}$ and w_j randomly between 0 and 1 did not assure convergence. Weights $\overline{w}_{jk}$ were scaled by 0.1 and weights w_j were scaled by 5 in order to obtain reliable convergence.

The net was then tested on real fade data and the results were less than satisfying. While the RMS error decreased in the learning mode with each pass through the data, very large errors occurred in the operating mode. This suggests that the net did not actually converge globally.

The data were run through the net in the learning mode in the same sequence each time. This results in the values for the weights at any given point being a function of the last 100 or so values of $A20$ rather than by all the values of $A20$. A local convergence is obtained but not a global convergence for the entire data set.

The neural net idea was set aside at this point in order to pursue the scaling filter work described in Chapter 4. However, further discussion of the problems encountered revealed that they are quite common in neural net applications. This suggests that we may still be on the rising slope of the learning curve and more work may be worthwhile.
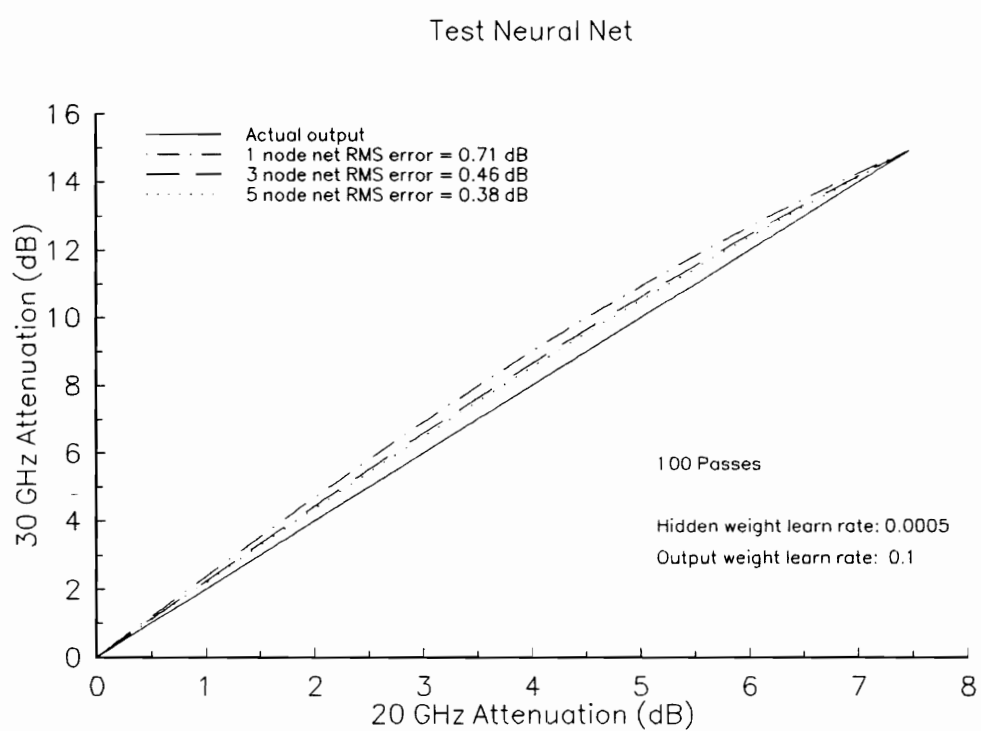
Figure 5.3-2: Test Neural Net.

There are two areas for additional work with neural nets. The global-local convergence problem can be addressed by sequencing the data through the net randomly during the learning mode. Secondly, we already know that attenuation at 30 GHz is approximate twice the attenuation at 20 GHz. The neural net can be modified to incorporate this insight. Figure 5.3-3 is such a net. The net supplies correction to a fixed gain linear scaler. The dynamic range of the net is reduced and this should result in better convergence.

Signal Input Nodes

Input to hidden node weights ($\overline{w}_{jk}$) $\longrightarrow$

Hidden Nodes

Hidden node to output weights (w_j)

$A20_1$ $A20_2$ $A20_3$

S_1 S_2 S_3

Fixed Gain Scaling

$\widehat{A30}$

Output Node

Estimate of 30 GHz attenuation
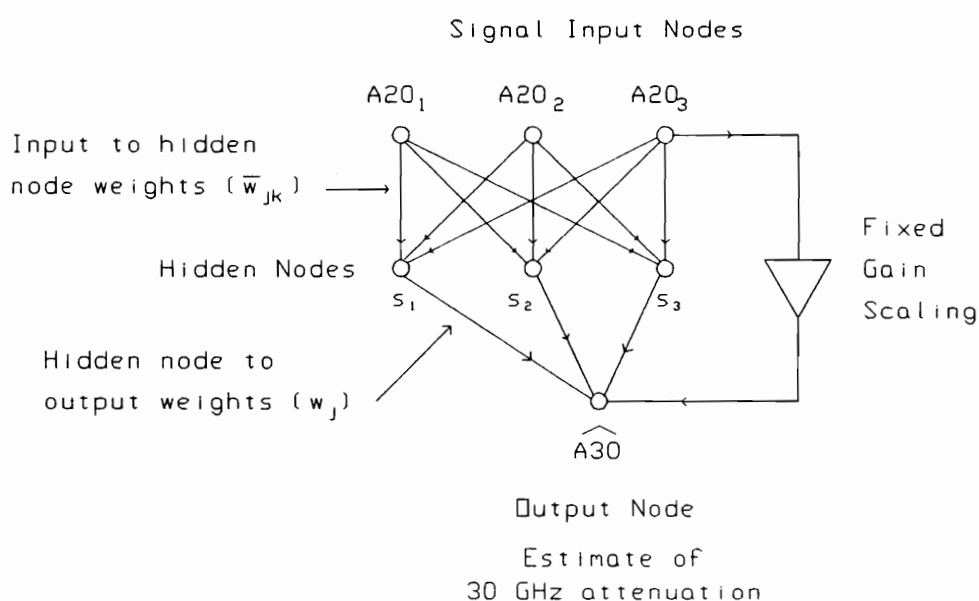
Figure 5.3-3: Combination linear scaling and neural net.

5.4 AREAS FOR ADDITIONAL WORK

5.4.1 Long Term Tests

The work presented here applies to isolated fade events. In order to have a working ULPC algorithm, it is necessary to connect the events in time. Long

term ULPC requires accurate clear air baseline setting, and possibly diurnal removal and correction for non-rain attenuations. The impact of these impairments will be determined by the desired "tightness" of control.

Seasonal and long term variations of scaling ratio need to be investigated. Are there significant site-to-site differences? Will storms in Olympia, Washington produce significantly different real time scaling ratios than storms in Miami, Florida? If such variations exist, can they be related to easily measured weather data? One of the objectives of the ACTS experiment program is to place propagation terminals in various different climate areas of the United States. Data from these terminals could be used to address these questions.

The two frequency scaling described above suggests that there may be no advantage to using two beacons, but some insight into the stability of the scaling factor may be obtained by examining the scaling ratio from 12.5 GHz to 20 GHz and 12.5 GHz to 30 GHz.

5.4.2 Additional Attenuation Impairments

Diurnal variations are a result of the daily shifts of a satellite in its orbit. The magnitude of these variations depends on satellite station keeping as well as on the satellite and the ground station antenna patterns. The station keeping for OLYMPUS has been fairly tight and our antenna beamwidth is relatively broad so the OLYMPUS spacecraft exhibited diurnal variations less than ±1 dB peak to peak per day as observed from Virginia Tech before North-South station keeping was abandoned in May 1992. Systems which employ narrow beam antennas and/or experience poor satellite station keeping may require correction for diurnal variations.

A relative straightforward technique to remove the diurnal variations was developed as part of the OLYMPUS experiment program [7]. The technique requires both radiometer and beacon attenuation measurements. Both measurements are available from the OLYMPUS experiment. The radiometer measurement, although limited in dynamic range, contains attenuation due to

atmospheric gases and rain but does not contain the diurnal effects. The beacon measurement contains attenuation due to atmospheric gases and rain as well as the diurnal effects. Adding the beacon and radiometer measurement results in attenuation with respect to free space and diurnal effects. Since free space attenuation does not vary with time, and assuming that the satellite beacon power is constant, the variations in attenuation that remain are due to the diurnal effects. These variations are gradual so a polynomial curve fit was developed to predict it. An area for further study would be to investigate the possibility of automating this process as part of a ULPC algorithm.

Figure 4.3-1 showed the effect of excess attenuation due to water vapor. The attenuation due to atmospheric gases, particularly water vapor was ignored, in the work presented in Chapter 4. Conditioning ULPC on 1 dB of 30 GHz attenuation reduces the effect of water vapor attenuation because this attenuation is greater at 20 GHz than at 30 GHz. It was noted in Section 4.4.1 that this conditioning is unrealistic because, if 20 GHz is being used to estimate/predict 30 GHz, the actual value of 30 GHz attenuation is unknown. It maybe possible to use some combination of 20 GHz signal, 20 GHz radiometer, 30 GHz signal, and 30 GHz radiometer to separate out diurnal, rain, and gaseous attenuation effects. Each could be weighted appropriately and applied to the ULPC algorithm. Is such a process possible and will it result in control accuracy which is worth the additional complexity and cost?

5.4.3 Radiometers for ULPC

Radiometer attenuation measurements are limited to approximately 10 dB, but this is compatible with the dynamic range of ULPC. Comsat investigated radiometer driven ULPC with less than satisfactory results [8]. The limitations of radiometer measurement may be overcome with a radiometer that employs the same antenna as used for the communications or beacon signal. Both the OLYMPUS terminal and the ACTS propagation terminal presently in development have a radiometer that shares a single antenna with the beacon receiver. In addition, the ACTS terminal antenna is used for both the uplink and downlink beacons.

In practice, a downlink radiometer could share the expensive microwave electronics with the signal receiver. This technique was successfully employed in the OLYMPUS experiment program and it is being incorporated into the ACTS program.

Will co-located radiometers work for ULPC? Are simple radiometers stable enough for ULPC? Does radiometer attenuation scale in the same manner as beacon measured attenuation? Given the slower response of radiometers, what kind of signal processing is necessary? These are all questions for further study. The OLYMPUS and particularly the ACTS experiment programs offer an excellent opportunity the revisit the question of radiometer driven ULPC.

5.4.4 ACTS Experiments

Based in part on this initial work, the Virginia Tech SATCOM Group proposed an ULPC experiment utilizing the ACTS satellite and the ACTS propagation terminal (APT) [9]. ACTS carries a 20.185 GHz and a 27.505 GHz beacon, and the APT is specially designed to receive these beacons and collect data for propagation measurement. The APT also has 20 and 27 GHz total power radiometers which share a single common antenna with the 20 and 27 GHz beacon receivers.

The proposed ULPC experiment employs an additional 27 GHz receiver, a programmable step attenuator, and an ULPC controller. Figure 5.4-1 is a block diagram of the experiment. The controller estimates the 30 GHz uplink attenuation from either the 20 GHz downlink beacon or the 27 GHz uplink beacon and sets the value of the step attenuator. If the attenuation estimate is correct, the output of the controlled 27 GHz recover will remain constant. The data acquisition system records the result.

Such a system can implement real time control and control from either the 20 or the 27 GHz beacon and/or the radiometers can be accomplished with simple changes in software.
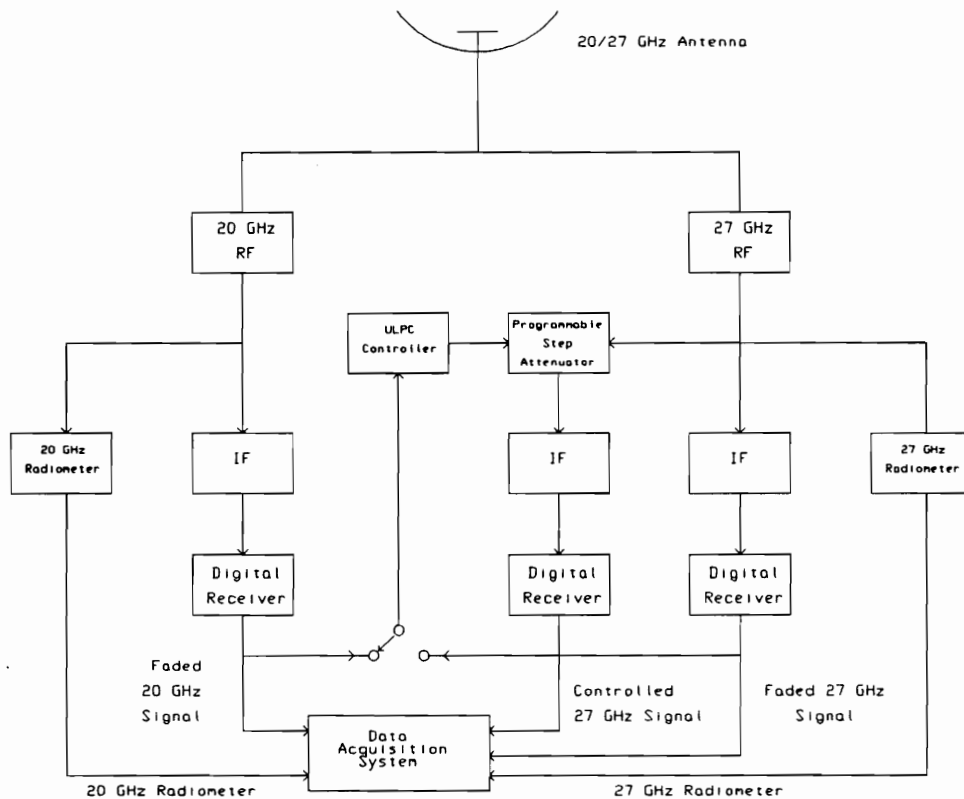
Figure 5.4-1: Proposed ULPC ACTS experiment.

5.4.5 OLYMPUS Simulator

If a less ambitious project is desired, the OLYMPUS data base could be used for a similar long term ULPC experiment.   The OLYMPUS data base represents over two years of fade data collected simultaneously at 12.5/20/30 GHz.   It should be possible to write a computer simulation for ULPC using this data. While the ACTS ULPC experiment will permit real time operation and the shared antenna of the 20 and 30 GHz receiver is an advantage, many of the same objectives of the ACTS ULPC experiment could be accomplished with an OLYMPUS data driven ULPC simulator.

5.4.6 Semi-Closed Loop Experiment

An enduring problem for open loop ULPC is setting the clear air base line. Open-loop control cannot distinguish between a fade and a shift in the baseline. Baseline shift can be due to a number of factors. Gain variations in the receiver due to aging and temperature are major causes. Ground terminal antenna mispointing can also produce a shift in the baseline. The Comsat work reported in [10] attempted to address this problem with very long term prediction.

A semi-closed loop system might overcome this problem. The central control station telemeters back to each remote station its received signal strength. The remote station would use this value to adjust its nominal transmitter power. This way each remote station maintains its assigned signal strength. This adjustment can be done every few days or weeks depending on system stability. If it is not desirable to automatically correct a terminal, it can be flagged as being potentially out of adjustment and service personnel can be alerted.

This measurement cannot be done either when there is attenuation on the central control downlink or when a particular remote station has engaged its ULPC. The remote station can flag its use of ULPC and control station downlink impairment could be determined by an operator at the control station.

The central control station could also use the satellite downlink to calibrate the remote stations. Each station would periodically receive a test tone or test message from the central control and the received signal strength is compared against a reference value. The receiver gain can be readjusted to reestablish this reference. Again this measurement must be done during clear air periods.

A semi-closed loop system could also be used to impose some order on a large number of terminals. It seems unlikely that a system with a large number of simple independent terminals with ULPC would stay correctly adjusted for long. Periodic monitoring of each terminal by central control could flag terminals whose initial adjustment is incorrect or that drift out of adjustment.

5.5 CONCLUSION

This work by no means presents a definitive ULPC algorithm. Given the variable nature of rain storms, such an algorithm probably does not exist. This work does suggest a workable ULPC scenario. Given a 10 dB dynamic range limitation, scaling of attenuation from the 20 GHz downlink to the 30 GHz uplink is a viable ULPC scheme. Uplink beacon ULPC is required if the ultimate in control accuracy is desired, but the additional terminal expense of a 30 GHz beacon receiver must be traded against better control. WARC-92 provided frequency allocations for such beacons so they can be incorporated in new systems.

Simple non-linear scaling does not appear to offer any advantage and the limited work reported here suggests that it offers poorer performance than linear scaling. The neural net algorithm is intriguing if for no other reason than it is a new and untried technique.

Radiometer driven or supported ULPC needs to be explored.

The question of control accuracy and threshold must be addressed by the system designers. Is ± 1 dB or ± 3 dB control good enough? How much margin is available? These are system questions and they impact on the choice of ULPC algorithms. Certain system configurations such as system calibration or semi-closed loop operation can possibly be used to support ULPC.

The data collected as part of the OLYMPUS program and the ACTS experiment program offer opportunities to explore additional ULPC questions. With some of the initial questions explored here, ACTS offers the unique opportunity to do on line ULPC.

5.6 REFERENCES

[1] Wall plaque in Dr. Tim Pratt's office.

[2] Kheirallah, H. N., and R. L. Olsen, "Comparison of one- and two-frequency technique of frequency scaling of rain attenuation statistics'" Electronics Letters, Vol. 18, No. 2, 21 January, 1982, pp. 51-53.

[3] Stutzman Warren L., et al., "Communications and Propagation Experiment Using the OLYMPUS Spacecraft: Report on the First Year of Data Collection," Virginia Tech Report EESATCOM 91-4, JPL Contract #958435, October 1991, pp. 201-224.

[4] Olsen, Roderic L., David V. Rogers, and Daniel B. Hodge, "The aR^b Relation in the Calculation of Rain Attenuation," IEEE Transactions on Antennas and Propagation, Vol. AP-26, No. 2, March 1978, pp. 318-329.

[5] Ihara, T. and Y. Furuhama, "Frequency scaling of rain attenuation at centimeter and millimeter waves using a path-averaged drop size distribution," Radio Science, Vol. 23, No. 3, May 1988, pp. 1365-1372.

[6] Müller, B. and J. Reinhardt, Neural Networks, An Introduction, Springer-Verlag, New York, 1991.

[7] Stutzman Warren L., et al., "Communications and Propagation Experiment Using the OLYMPUS Spacecraft: Report on the First Year of Data Collection," Virginia Tech Report EESATCOM 91-4, JPL Contract #958435, October 1991, pp. 36-47.

[8] Lin, K. T., C. Zaks, and D. V. Rogers, " Ku-Band Up-Link Power Control Development," Comsat Technical Memorandum CL-13-87, November 12, 1987.

[9] An ACTS Propagation Experiment with Emphasis on Adaptive Control. Research proposal submitted to National Aeronautics and Space Administration, Lewis Research Center by Warren L. Stutzman, Timothy Pratt, and Ahmad Safaai-Jazi, February 7, 1992.

[10] Dissanayake, Asoka, and Chaim Zaks, "Up-Link Power Control Developments at Comsat Laboratories," Comsat Technical Note STD/92-005, February, 1992.

APPENDIX 1: EVENT CATALOG AND UPLINK POWER CONTROL ALGORITHM PERFORMANCE

A1.1 EVENT CATALOG

Table A1.1-1 Catalog of events used in data analysis

Event Date	Time (UTC)	Clear Air Reference (dB)		Approx. Peak Fade (dB)	
		20 GHz	30 GHz	20 GHz	30GHz
Nov. 5,6, 1990	2300-0200	72.70	72.70	32.0	> 40.0
Nov. 10, 1990	1100-1300	72.40	71.60	15.0	32.0
Nov.17,1990	0500-0700	73.10	72.10	2.7	5.0
Nov. 23, 1990	0700-0900	73.50	72.00	2.8	6.0
Nov. 28, 1990	2000-2100	73.30	71.80	5.0	9.0
Jan. 7, 1991	1500-1600	70.40	70.00	5.3	11.0
Jan. 8, 1991	2200-2400	70.30	70.80	3.0	6.0
Jan. 20, 1991	0500-0900	70.40	70.60	4.0	6.0
Feb.6, 1991	1100-1500	70.20	69.90	7.0	12.0
Feb. 7, 1991	0600-1000	70.40	69.70	9.0	20.0
Mar. 3, 1991	2100-2400	69.80	69.10	8.0	16.5
Mar 7, 1991	0000-0300	69.10	69.80	10.0	23.0
Mar. 22, 1991	1100-1300	70.00	68.80	14.0	28.0
Mar. 26, 1991	2000-2300	70.50	70.20	5.5	9.0
April 5, 1991	1300-1500	69.90	70.10	3.5	5.5
April 8, 1991	2000-2300	69.70	68.30	14.0	26.0
April 9, 1991	0400-0600	69.20	68.30	28.0	> 40.0
April 9, 10,1991	2200-0200	70.10	68.70	9.5	27.6
April 15, 1991	0800-1000	69.50	69.50	14.0	29.0
April 24, 1991	1200-1500	71.20	70.80	6.0	13.0
April 30, 1991	0200-0400	69.60	68.30	23.0	> 40.0
May 6, 1991	1700-1900	70.10	69.50	38.0	> 40.0
May 12, 1991	1900-2200	69.10	68.50	28.0	> 40.0
May 14, 1991	2000-2200	69.30	68.90	4.0	8.0
May 19, 1991	1300-1600	69.50	69.10	7.0	18.0
May 21, 1991	0700-0900	69.60	68.20	4.0	8.5

Total time: 66 hours

A1.2.1: November 5,6, 1990 2300-0200 UTC Event
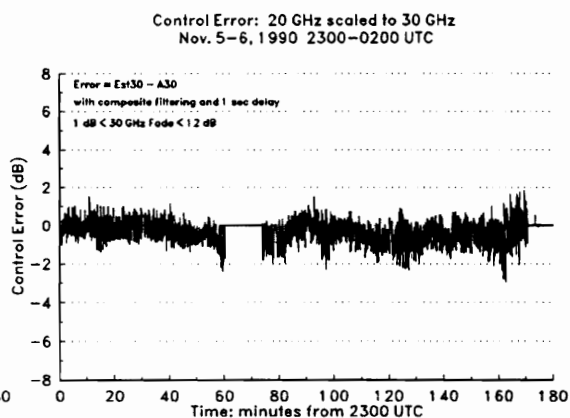
Figure A1.2.1-1

Figure A1.2.1-2

Table A1.2.1: RMS error and optimum scaling factor and filter bandwidth
for November 5-6, 1990 2300-0200 UTC

Delay sec	RMS Error (dB)	Scale Factor	Bandwidth (Hz)
		20 GHz CCIR scaled to 30 GHz: scale ratio = 1.97	
0	0.75		
1	0.75		
		20 GHz filtered, scaled to 30 GHz: Composite	
0	0.61		
1	0.65		
5	0.69		
10	0.74		
20	0.84		
		20 GHz filtered, scaled to 30 GHz: Optimum	
0	0.44	2.1229	0.10737
1	0.51	2.1227	0.04845
5	0.57	2.1190	0.05160
10	0.64	2.1137	0.05338
20	0.74	2.1037	0.05670
		30 GHz predicting 30 GHz: Composite	
1	0.40		
5	0.46		
10	0.53		
20	0.68		
		30 GHz predicting 30 GHz: Optimum	
1	0.40	0.999067	0.08806
5	0.46	0.997666	0.10618
10	0.53	0.995584	0.12236
20	0.68	0.990002	0.11274

114

A1.2.2: November 10, 1990 1100-1300 UTC Event
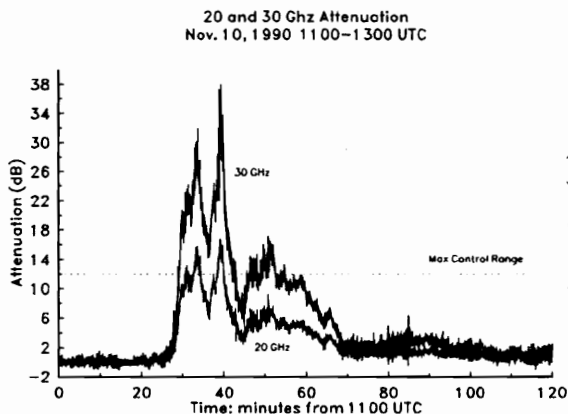
Figure A1.2.2-1
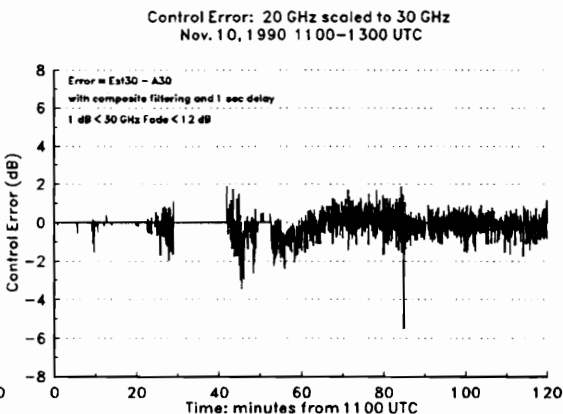
Figure A1.2.2-2

Table A1.2.2: RMS error and optimum scaling factor and filter bandwidth
for November 10, 1990 1100-1300 UTC

Delay sec	RMS Error	Scale Factor	Bandwidth (Hz)
	(dB)	20 GHz CCIR scaled to 30 GHz: scale ratio = 1.97	
0	1.05		
1	0.85		
		20 GHz filtered, scaled to 30 GHz: Composite	
0	0.68		
1	0.62		
5	0.75		
10	0.79		
20	0.88		
		20 GHz filtered, scaled to 30 GHz: Optimum	
0	0.60	2.042046	0.030708
1	0.55	2.041140	0.072426
5	0.68	2.039552	0.024460
10	0.72	2.035716	0.026956
20	0.82	2.017693	0.027380
		30 GHz predicting 30 GHz: Composite	
1	0.60		
5	0.60		
10	0.64		
20	0.73		
		30 GHz predicting 30 GHz: Optimum	
1	0.56	0.999160	0.038755
5	0.59	0.998515	0.051372
10	0.63	0.997476	0.061734
20	0.72	0.986654	0.055180

A1.2.3: November 17, 1990 0500-0700 UTC Event

20 and 30 Ghz Attenuation
Nov. 17, 1990 0500-0700 UTC

Figure A1.2.3-1

Control Error: 20 GHz scaled to 30 GHz
Nov. 17, 1990 0500-0700 UTC

Error = Est30 − A30
with composite filtering and 1 sec delay
1 dB < 30 GHz Fade < 12 dB

Figure A1.2.3-2

Table A1.2.3: RMS error and optimum scaling factor and filter bandwidth
for November 17, 1990 0500-0700 UTC

Delay sec	RMS Error	Scale Factor	Bandwidth (Hz)
	(dB)	20 GHz CCIR scaled to 30 GHz: scale ratio = 1.97	
0	0.54		
1	0.43		
		20 GHz filtered, scaled to 30 GHz: Composite	
0	0.31		
1	0.36		
5	0.40		
10	0.43		
20	0.48		
		20 GHz filtered, scaled to 30 GHz: Optimum	
0	0.30	1.874962	0.065624
1	0.35	1.876102	0.030419
5	0.39	1.874042	0.021869
10	0.41	1.870121	0.026677
20	0.46	1.865560	0.023551
		30 GHz predicting 30 GHz: Composite	
1	0.36		
5	0.37		
10	0.40		
20	0.45		
		30 GHz predicting 30 GHz: Optimum	
1	0.35	0.998604	0.039599
5	0.37	0.997681	0.043251
10	0.39	0.997566	0.047684
20	0.45	0.992421	0.055371

116

A1.2.4: November 23, 1990 0700-0900 UTC Event

20 and 30 Ghz Attenuation
Nov. 23, 1990 0700-0900 UTC

Figure A1.2.4-1

Control Error: 20 GHz scaled to 30 GHz
Nov. 23, 1990 0500-0700 UTC

Figure A1.2.4-2

Table A1.2.4: RMS error and optimum scaling factor and filter bandwidth
for November 23, 1990 0500-0700 UTC

Delay sec	RMS Error	Scale Factor	Bandwidth (Hz)
	(dB)	20 GHz CCIR scaled to 30 GHz: scale ratio = 1.97	
0	1.16		
1	1.18		
		20 GHz filtered, scaled to 30 GHz: Composite	
0	1.06		
1	1.11		
5	1.10		
10	1.10		
20	1.11		
		20 GHz filtered, scaled to 30 GHz: Optimum	
0	0.59	1.302450	0.078632
1	0.59	1.421256	0.042090
5	0.61	1.329180	0.035015
10	0.61	1.350040	0.022379
20	0.61	1.418505	0.053910
		30 GHz predicting 30 GHz: Composite	
1	0.21		
5	0.22		
10	0.23		
20	0.28		
		30 GHz predicting 30 GHz: Optimum	
1	0.20	0.999550	0.050090
5	0.22	0.999151	0.059270
10	0.23	0.996467	0.068256
20	0.20	0.993384	0.080298

A1.2.5: November 28, 1990 2000-2100 UTC Event
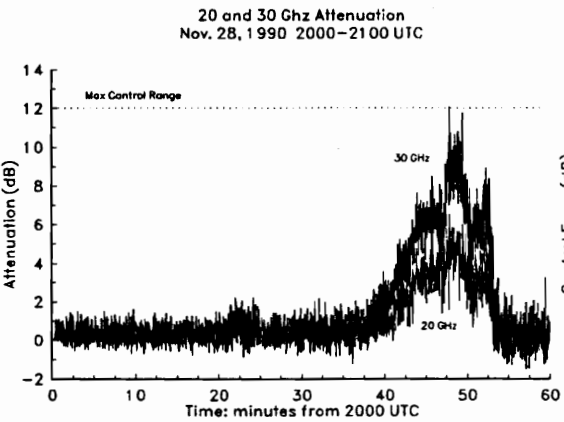
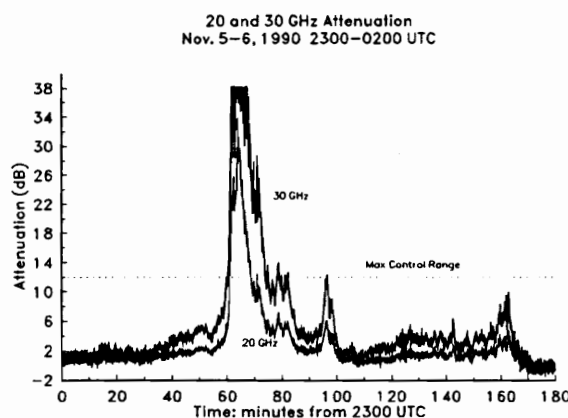

Figure A1.2.5-1
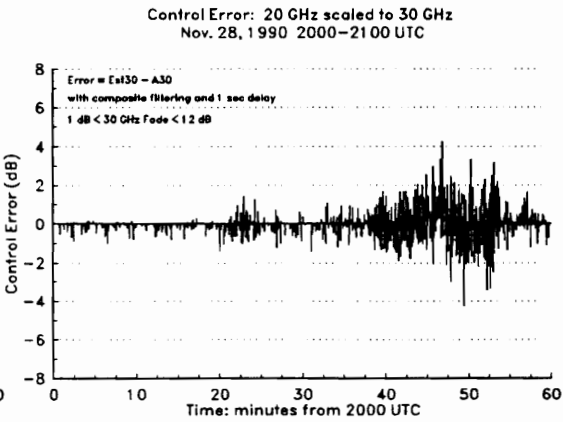
Figure A1.2.5-2

Table A1.2.5: RMS error and optimum scaling factor and filter bandwidth
for November 28, 1990 2000-2100 UTC

Delay	RMS	Scale	Bandwidth
sec	Error	Factor	(Hz)
	(dB)	20 GHz CCIR scaled to 30 GHz: scale ratio = 1.97		
0	1.54		
1	1.24		
		20 GHz filtered, scaled to 30 GHz: Composite		
0	0.91		
1	0.88		
5	0.92		
10	0.94		
20	1.08		
		20 GHz filtered, scaled to 30 GHz: Optimum		
0	0.90	1.924017	0.030981
1	0.86	1.923630	0.020094
5	0.90	1.925753	0.021399
10	0.93	1.917050	0.030007
20	1.06	1.906495	0.031164
		30 GHz predicting 30 GHz: Composite		
1	0.93		
5	0.93		
10	0.99		
20	1.11		
		30 GHz predicting 30 GHz: Optimum		
1	0.90	0.998454	0.038388
5	0.93	0.997492	0.057666
10	0.98	0.996573	0.069057
20	1.11	0.989877	0.083481

118

## A1.2.6: January 7, 1991 1500-1600 UTC Event
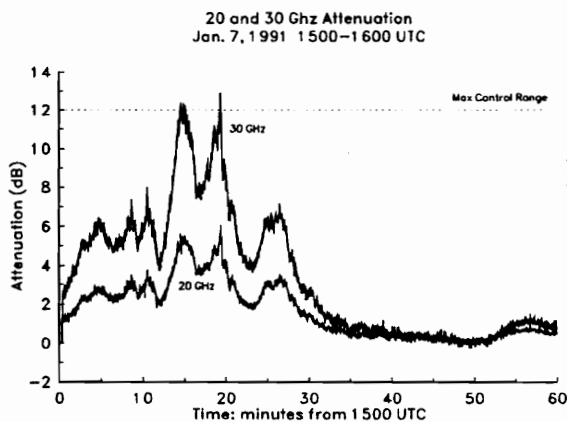
Figure A1.2.6-1
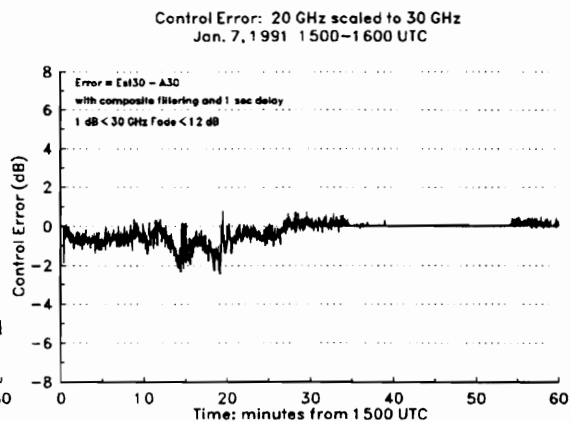
Figure A1.2.6-2

Table A1.2.6: RMS error and optimum scaling factor and filter bandwidth
for January 7, 1991 1500-1600 UTC

Delay sec	RMS Error	Scale Factor	Bandwidth (Hz)
	(dB)	20 GHz CCIR scaled to 30 GHz: scale ratio = 1.97	
0	0.62		
1	0.62		
		20 GHz filtered, scaled to 30 GHz: Composite	
0	0.70		
1	0.70		
5	0.77		
10	0.84		
20	0.97		
		20 GHz filtered, scaled to 30 GHz: Optimum	
0	0.36	2.143261	0.127429
1	0.39	2.142680	0.135187
5	0.47	2.140041	0.160950
10	0.58	2.136041	0.188555
20	0.77	2.128388	0.225177
		30 GHz predicting 30 GHz: Composite	
1	0.23		
5	0.34		
10	0.46		
20	0.66		
		30 GHz predicting 30 GHz: Optimum	
1	0.23	0.999599	0.187994
5	0.32	0.999758	0.269255
10	0.44	0.999864	0.349309
20	0.65	0.997252	0.446068

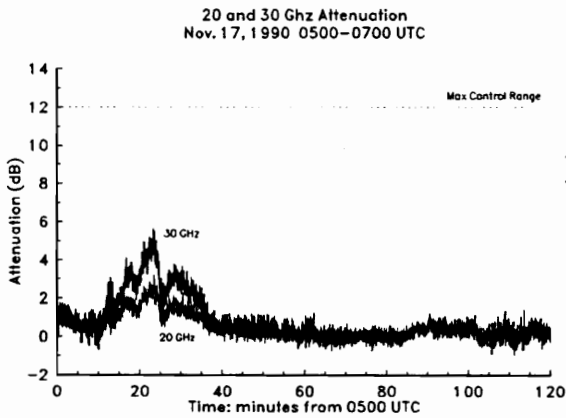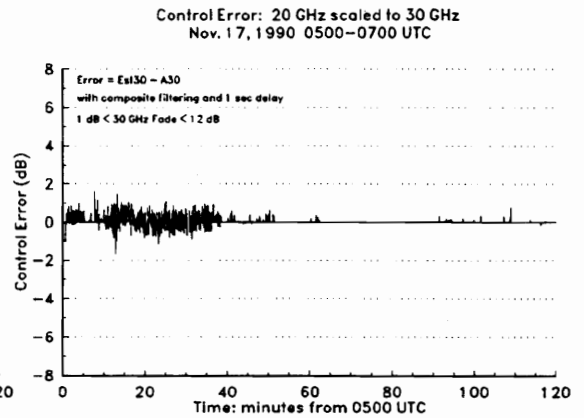## A1.2.7: January 8, 1991 2200-2400 UTC Event
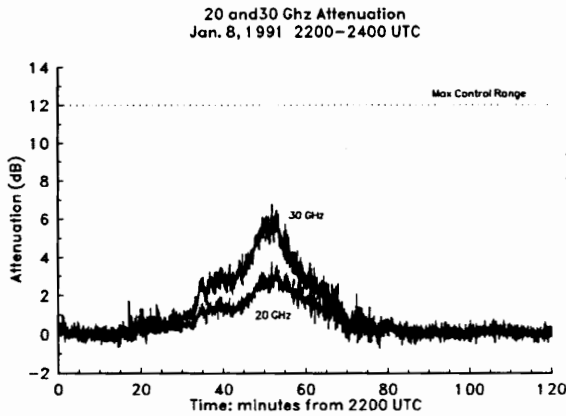
Figure A1.2.7-1

Figure A1.2.7-2

Table A1.2.7: RMS error and optimum scaling factor and filter bandwidth
for January 8, 1991 2200-2400 UTC

Delay sec	RMS Error	Scale Factor	Bandwidth (Hz)
	(dB)	20 GHz CCIR scaled to 30 GHz: scale ratio = 1.97	
0	0.66		
1	0.67		
		20 GHz filtered, scaled to 30 GHz: Composite	
0	0.49		
1	0.49		
5	0.54		
10	0.56		
20	0.60		
		20 GHz filtered, scaled to 30 GHz: Optimum	
0	0.48	1.890319	0.036296
1	0.48	1.887907	0.045317
5	0.53	1.884944	0.027647
10	0.55	1.884001	0.028840
20	0.59	1.879192	0.032370
		30 GHz predicting 30 GHz: Composite	
1	0.34		
5	0.34		
10	0.36		
20	0.39		
		30 GHz predicting 30 GHz: Optimum	
1	0.32	0.999448	0.025914
5	0.33	0.999149	0.030416
10	0.35	0.998432	0.036454
20	0.38	0.997831	0.045017

A1.2.8: January 20, 1991 0500-0900 UTC Event

20 and 30 Ghz Attenuation
Jan. 20, 1991 0500-0900 UTC

Control Error: 20 GHz scaled to 30 GHz
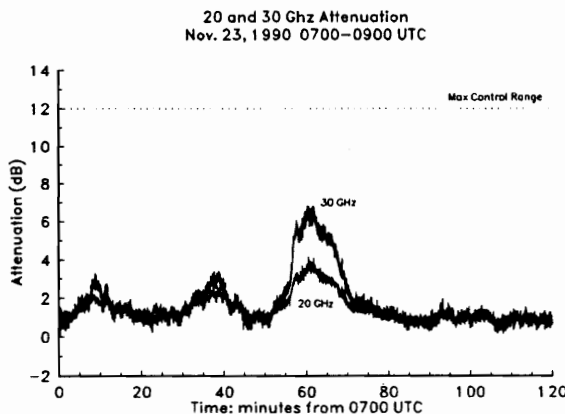**Jan. 20, 1991 0500-0900 UTC**
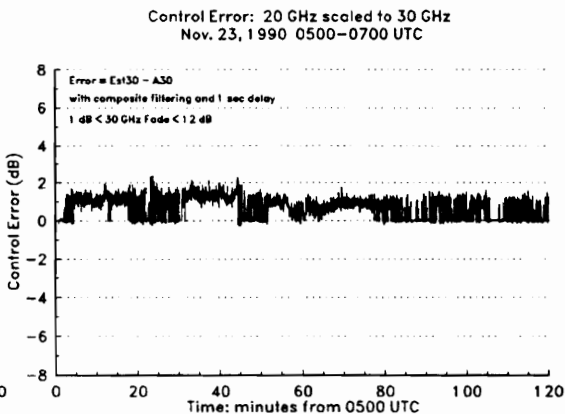

Figure A1.2.8-1

Figure A1.2.8-2

Table A1.2.8: RMS error and optimum scaling factor and filter bandwidth
for January 20, 1991 0500-0900 UTC

Delay sec	RMS Error	Scale Factor	Bandwidth (Hz)
	(dB)	20 GHz CCIR scaled to 30 GHz: scale ratio = 1.97	
0	1.41		
1	1.42		
		20 GHz filtered, scaled to 30 GHz: Composite	
0	1.31		
1	1.32		
5	1.31		
10	1.31		
20	1.31		
		20 GHz filtered, scaled to 30 GHz: Optimum	
0	0.34	1.313125	0.062341
1	0.35	1.308821	0.102977
5	0.36	1.305056	0.069841
10	0.37	1.311801	0.095776
20	0.40	1.296133	0.090915
		30 GHz predicting 30 GHz: Composite	
1	0.14		
5	0.16		
10	0.18		
20	0.23		
		30 GHz predicting 30 GHz: Optimum	
1	0.14	0.999742	0.0657450
5	0.16	0.999339	0.0871101
10	0.18	0.998213	0.1095183
20	0.23	0.997339	0.1538353

121

A1.2.9: February 6, 1991 1100-1500 UTC Event

20 and 30 Ghz Attenuation
Feb. 6, 1991 1100-1500 UTC

Figure A1.2.9-1

Control Error: 20 GHz scaled to 30 GHz
Feb. 6, 1991 1100-1500 UTC

Figure A1.2.9-2

Table A1.2.9: RMS error and optimum scaling factor and filter bandwidth
for February 6, 1991 1100-1500 UTC

Delay sec	RMS Error	Scale Factor	Bandwidth (Hz)
	(dB)	20 GHz CCIR scaled to 30 GHz: scale ratio = 1.97	
0	0.86		
1	0.84		
		20 GHz filtered, scaled to 30 GHz: Composite	
0	0.73		
1	0.73		
5	0.73		
10	0.74		
20	0.78		
		20 GHz filtered, scaled to 30 GHz: Optimum	
0	0.28	1.677520	0.096078
1	0.28	1.677032	0.160506
5	0.31	1.674332	0.092244
10	0.35	1.673465	0.116368
20	0.43	1.668483	0.162431
		30 GHz predicting 30 GHz: Composite	
1	0.18		
5	0.21		
10	0.26		
20	0.36		
		30 GHz predicting 30 GHz: Optimum	
1	0.18	0.999815	0.092354
5	0.21	0.999381	0.130202
10	0.25	0.998993	0.174639
20	0.35	0.995891	0.225756

122

## A1.2.10: February 7, 1991 0600-1000 UTC Event
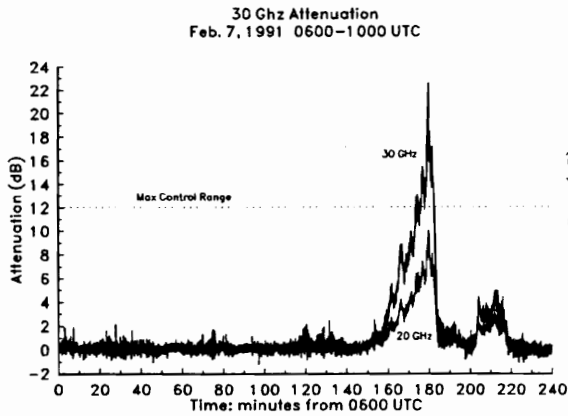
Figure A1.2.10-1
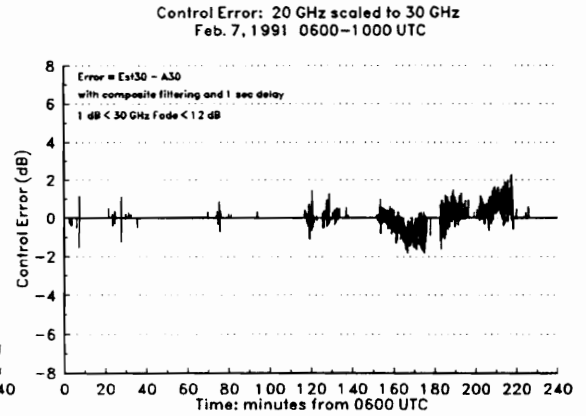
Figure A1.2.10-2

Table A1.2.10: RMS error and optimum scaling factor and filter bandwidth
for February 7, 1991 0600-1000 UTC

| Delay | RMS | Scale | Bandwidth |
sec	Error	Factor	(Hz)
	(dB)	20 GHz CCIR scaled to 30 GHz: scale ratio = 1.97	
0	0.85		
1	0.76		
		20 GHz filtered, scaled to 30 GHz: Composite	
0	0.68		
1	0.69		
5	0.75		
10	0.80		
20	0.92		
		20 GHz filtered, scaled to 30 GHz: Optimum	
0	0.66	1.985409	0.046509
1	0.68	1.985101	0.055588
5	0.74	1.980777	0.044653
10	0.79	1.973080	0.055490
20	0.92	1.963346	0.068181
		30 GHz predicting 30 GHz: Composite	
1	0.44		
5	0.47		
10	0.53		
20	0.69		
		30 GHz predicting 30 GHz: Optimum	
1	0.43	0.999257	0.061499
5	0.47	1.000668	0.077445
10	0.53	0.998062	0.105129
20	0.69	1.004359	0.112007

123

## A1.2.11: March 3, 1991 2100-2400 UTC Event
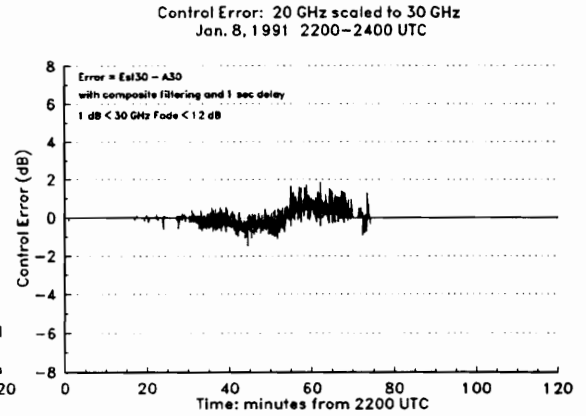

Figure A1.2.11-1

Figure A1.2.11-2

Table A1.2.11: RMS error and optimum scaling factor and filter bandwidth
for March 3, 1991 2100-2400 UTC

Delay sec	RMS Error	Scale Factor	Bandwidth (Hz)
	(dB)	20 GHz CCIR scaled to 30 GHz: scale ratio = 1.97	
0	0.73		
1	0.70		
		20 GHz filtered, scaled to 30 GHz: Composite	
0	0.53		
1	0.56		
5	0.57		
10	0.60		
20	0.67		
		20 GHz filtered, scaled to 30 GHz: Optimum	
0	0.50	1.862704	0.035486
1	0.52	1.865502	0.029548
5	0.55	1.864499	0.034076
10	0.58	1.863065	0.039579
20	0.66	1.859719	0.053268
		30 GHz predicting 30 GHz: Composite	
1	0.35		
5	0.38		
10	0.44		
20	0.55		
		30 GHz predicting 30 GHz: Optimum	
1	0.34	0.999385	0.072809
5	0.38	0.999028	0.088911
10	0.44	0.998037	0.098180
20	0.55	0.996212	0.121902

124

A1.2.12: March 7, 1991 0000-0300 UTC Event

20 and 30 Ghz Attenuation
Mar. 7, 1991 0000-0300 UTC

Figure A1.2.12-1
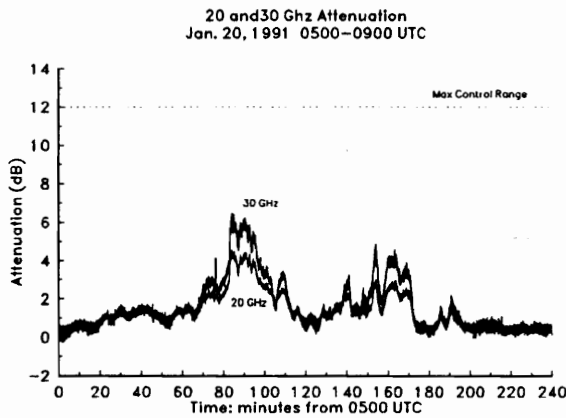

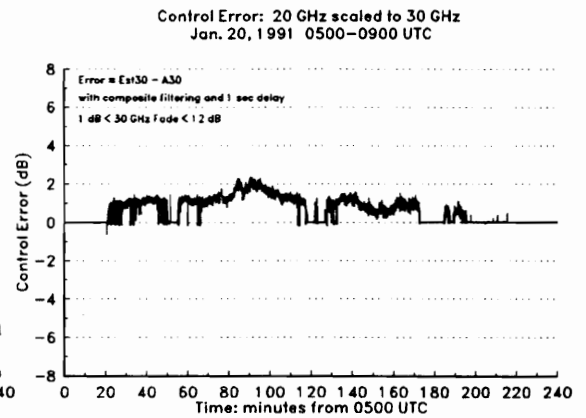Control Error: 20 GHz scaled to 30 GHz
Mar. 7, 1991 0000-0300 UTC

Figure A1.2.12-2

Table A1.2.12: RMS error and optimum scaling factor and filter bandwidth
for March 7, 1991 0000-0300 UTC

Delay sec	RMS Error	Scale Factor	Bandwidth (Hz)
	(dB)	20 GHz CCIR scaled to 30 GHz: scale ratio = 1.97	
0	1.96		
1	1.92		
		20 GHz filtered, scaled to 30 GHz: Composite	
0	1.98		
1	1.95		
5	1.97		
10	1.99		
20	2.04		
		20 GHz filtered, scaled to 30 GHz: Optimum	
0	1.59	2.532589	0.057142
1	1.55	2.512622	0.043736
5	1.57	2.525136	0.063103
10	1.60	2.513592	0.075862
20	1.69	2.489027	0.083499
		30 GHz predicting 30 GHz: Composite	
1	0.32		
5	0.37		
10	0.46		
20	0.63		
		30 GHz predicting 30 GHz: Optimum	
1	0.32	0.999565	0.096561
5	0.37	0.998786	0.141453
10	0.45	0.997474	0.173186
20	0.63	0.993263	0.204031

125

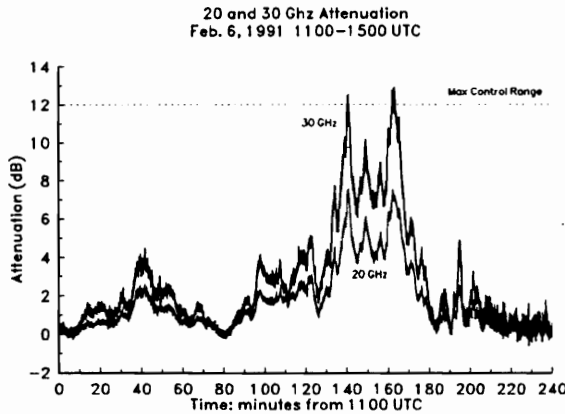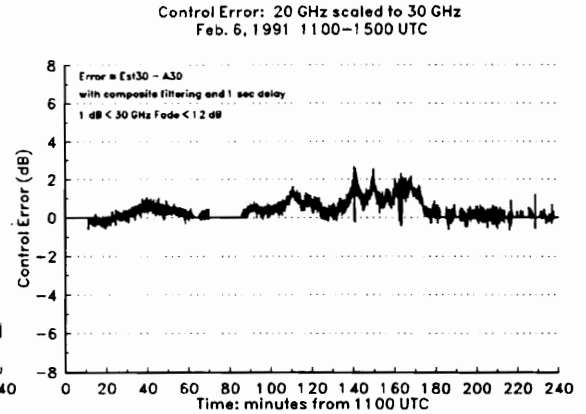## A1.2.13: March 22, 1991 1100-1300 UTC Event

Figure A1.2.13-1

Figure A1.2.13-2

Table A1.2.13: RMS error and optimum scaling factor and filter bandwidth
for March 22, 1991 1100-1300 UTC

Delay sec	RMS Error	Scale Factor	Bandwidth (Hz)
	(dB)	20 GHz CCIR scaled to 30 GHz: scale ratio = 1.97	
0	1.03		
1	0.91		
		20 GHz filtered, scaled to 30 GHz: Composite	
0	0.73		
1	0.76		
5	0.87		
10	0.99		
20	1.25		
		20 GHz filtered, scaled to 30 GHz: Optimum	
0	0.46	1.752288	0.079355
1	0.49	1.751393	0.120908
5	0.64	1.746803	0.102417
10	0.78	1.743463	0.126131
20	1.08	1.724278	0.160712
		30 GHz predicting 30 GHz: Composite	
1	0.47		
5	0.59		
10	0.75		
20	1.07		
		30 GHz predicting 30 GHz: Optimum	
1	0.47	0.999056	0.124237
5	0.58	0.997628	0.188491
10	0.74	0.993563	0.243242
20	1.06	0.993310	0.280678

A1.2.14: March 26, 1991 2000-2300 UTC Event

20 and 30 Ghz Attenuation
Mar. 26, 1991 2000-2300 UTC

Control Error: 20 GHz scaled to 30 GHz
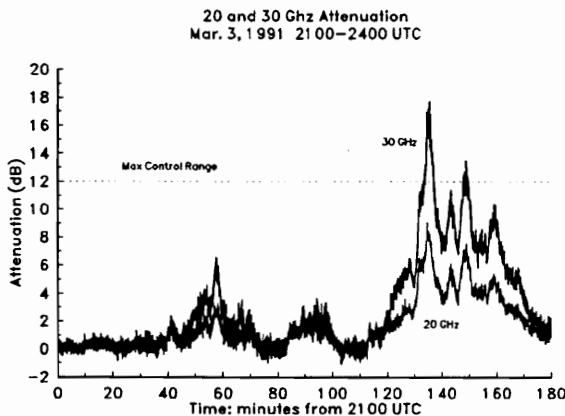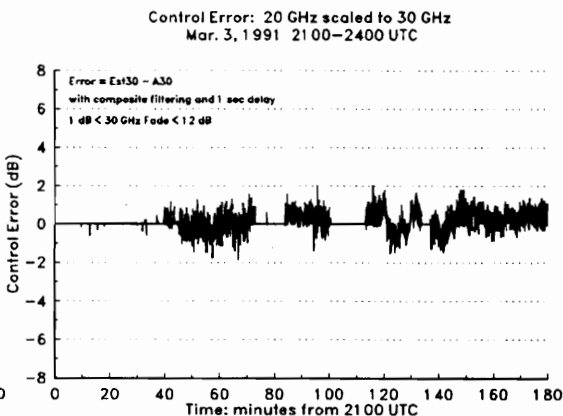Mar. 26, 1991 2000-2300 UTC

Figure A1.2.14-1

Figure A1.2.14-2

Table A1.2.14: RMS error and optimum scaling factor and filter bandwidth
for March 26, 1991 2000-2300 UTC

Delay sec	RMS Error	Scale Factor	Bandwidth (Hz)
	(dB)	20 GHz CCIR scaled to 30 GHz: scale ratio = 1.97	
0	1.97		
1	1.98		
		20 GHz filtered, scaled to 30 GHz: Composite	
0	1.81		
1	1.83		
5	1.82		
10	1.82		
20	1.85		
		20 GHz filtered, scaled to 30 GHz: Optimum	
0	0.54	1.438577	0.091783
1	0.57	1.436934	0.115899
5	0.60	1.436074	0.129726
10	0.64	1.435354	0.154440
20	0.72	1.432472	0.152199
		30 GHz predicting 30 GHz: Composite	
1	0.22		
5	0.30		
10	0.38		
20	0.51		
		30 GHz predicting 30 GHz: Optimum	
1	0.22	0.999613	0.164877
5	0.30	0.998987	0.192370
10	0.38	0.997850	0.202738
20	0.51	0.995666	0.224290

127

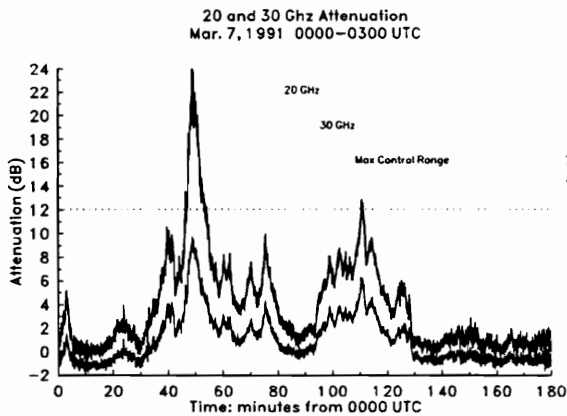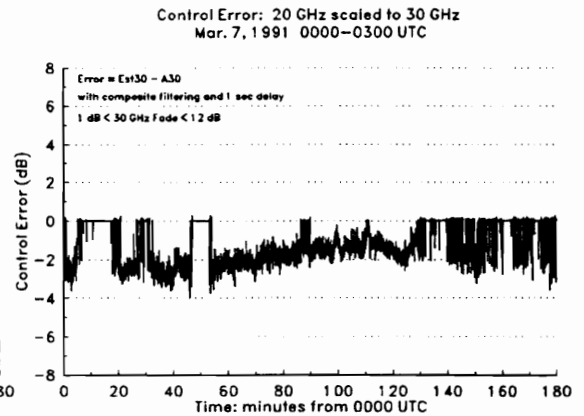## A1.2.15: April 5, 1991 1300-1500 UTC Event
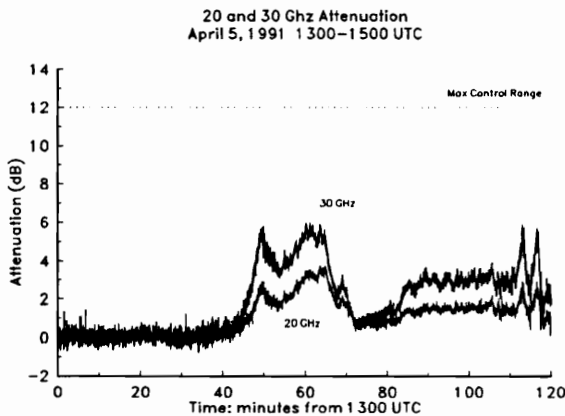
Figure A1.2.15-1

Figure A1.2.15-2

Table A1.2.15: RMS error and optimum scaling factor and filter bandwidth
for April 5, 1991 1300-1500 UTC

Delay sec	RMS Error	Scale Factor	Bandwidth (Hz)
	(dB)	20 GHz CCIR scaled to 30 GHz: scale ratio = 1.97	
0	0.63		
1	0.60		
		20 GHz filtered, scaled to 30 GHz: Composite	
0	0.54		
1	0.55		
5	0.59		
10	0.62		
20	0.68		
		20 GHz filtered, scaled to 30 GHz: Optimum	
0	0.51	1.860198	0.072758
1	0.51	1.857808	0.138135
5	0.56	1.817733	0.049708
10	0.59	1.815058	0.057179
20	0.65	1.808639	0.069942
		30 GHz predicting 30 GHz: Composite	
1	0.22		
5	0.26		
10	0.30		
20	0.39		
		30 GHz predicting 30 GHz: Optimum	
1	0.22	0.999289	0.077613
5	0.26	0.999025	0.066932
10	0.30	0.998863	0.079885
20	0.39	0.997837	0.103054

128

A1.2.16: April 8, 1991 2000-2300 UTC Event

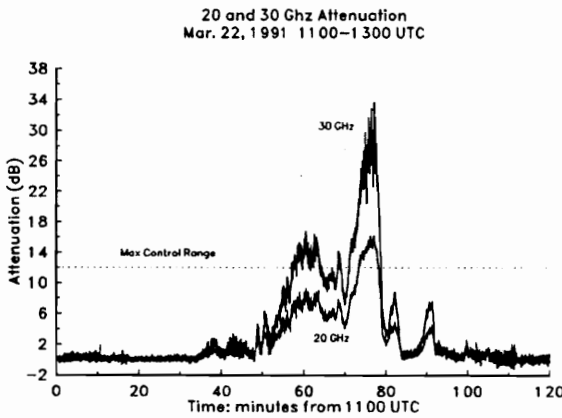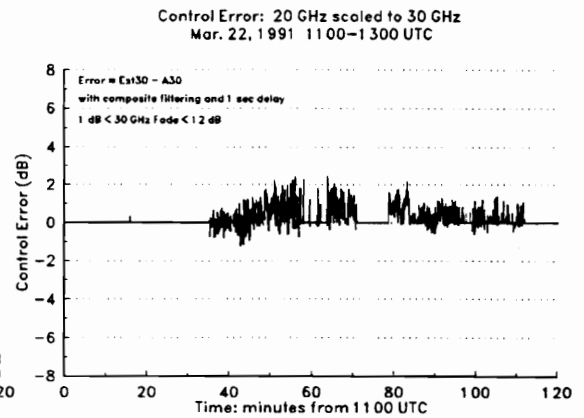Figure A1.2.16-1   Figure A1.2.16-2

Table A1.2.16: RMS error and optimum scaling factor and filter bandwidth
for April 8, 1991 2000-2300 UTC

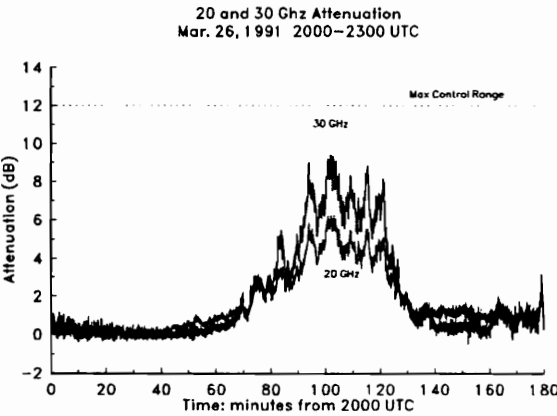| Delay sec	RMS Error	Scale Factor	Bandwidth (Hz)
	(dB)	20 GHz CCIR scaled to 30 GHz: scale ratio = 1.97	
0	0.98		
1	0.79		
		20 GHz filtered, scaled to 30 GHz: Composite	
0	0.74		
1	0.75		
5	0.87		
10	0.97		
20	1.14		
		20 GHz filtered, scaled to 30 GHz: Optimum	
0	0.57	2.092794	0.058306
1	0.60	2.091665	0.076510
5	0.74	2.086886	0.047120
10	0.86	2.080473	0.050760
20	1.06	2.067938	0.057235
		30 GHz predicting 30 GHz: Composite	
1	0.55		
5	0.62		
10	0.73		
20	0.94		
		30 GHz predicting 30 GHz: Optimum	
1	0.54	0.998933	0.077010
5	0.62	0.997007	0.096403
10	0.73	0.993115	0.106694
20	0.94	0.989800	0.134615

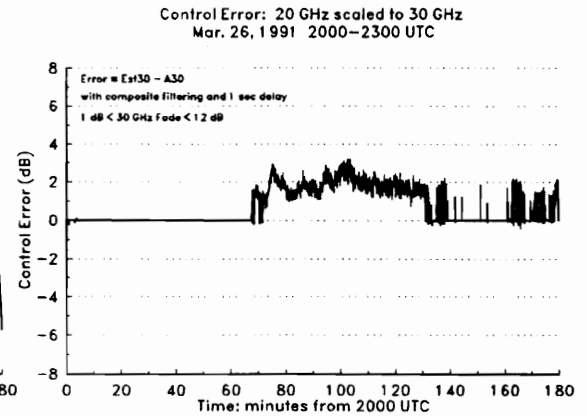## A1.2.17: April 9, 1991 0400-0600 UTC Event

Figure A1.2.17-1

Figure A1.2.17-2

Table A1.2.17: RMS error and optimum scaling factor and filter bandwidth
for April 9, 1991 0400-0600 UTC

Delay sec	RMS Error	Scale Factor	Bandwidth (Hz)
	(dB)	20 GHz CCIR scaled to 30 GHz: scale ratio = 1.97	
0	0.94		
1	0.74		
		20 GHz filtered, scaled to 30 GHz: Composite	
0	0.79		
1	0.77		
5	0.88		
10	0.97		
20	1.18		
		20 GHz filtered, scaled to 30 GHz: Optimum	
0	0.48	2.207527	0.057736
1	0.48	2.208946	0.083948
5	0.67	2.195874	0.051895
10	0.80	2.185382	0.078381
20	1.07	2.156444	0.085962
		30 GHz predicting 30 GHz: Composite	
1	0.49		
5	0.61		
10	0.74		
20	1.02		
		30 GHz predicting 30 GHz: Optimum	
1	0.49	0.998659	0.118178
5	0.60	0.996147	0.161068
10	0.74	0.988754	0.159912
20	1.00	0.979756	0.299425

A1.2.18: April 9-10, 1991 2200-0200 UTC Event

20 and 30 Ghz Attenuation
April 9-10, 1991 2200-0200 UTC

Figure A1.2.18-1

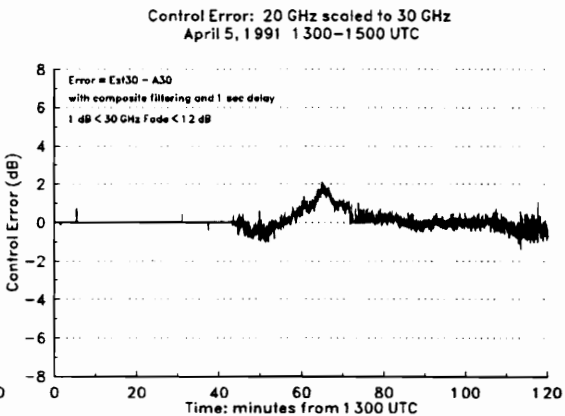Control Error: 20 GHz scaled to 30 GHz
April 9-10, 1991 2200-0200 UTC

Figure A1.2.18-2

Table A1.2.18: RMS error and optimum scaling factor and filter bandwidth
for April 9-10, 1991 2200-0200 UTC

Delay sec	RMS Error	Scale Factor	Bandwidth (Hz)
	(dB)	20 GHz CCIR scaled to 30 GHz: scale ratio = 1.97	
0	1.84		
1	1.66		
		20 GHz filtered, scaled to 30 GHz: Composite	
0	1.59		
1	1.56		
5	1.63		
10	1.66		
20	1.74		
		20 GHz filtered, scaled to 30 GHz: Optimum	
0	1.47	2.092041	0.024963
1	1.46	2.090235	0.026981
5	1.52	2.104651	0.020091
10	1.55	2.089663	0.024192
20	1.64	2.080117	0.028068
		30 GHz predicting 30 GHz: Composite	
1	0.75		
5	0.80		
10	0.90		
20	1.08		
		30 GHz predicting 30 GHz: Optimum	
1	0.72	0.998685	0.051207
5	0.79	0.996927	0.065198
10	0.89	0.995408	0.068562
20	1.07	0.990968	0.075541

131

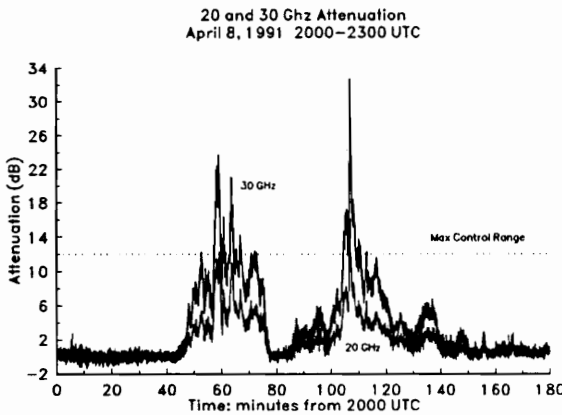## A1.2.19: April 15, 1991 0800-1000 UTC Event
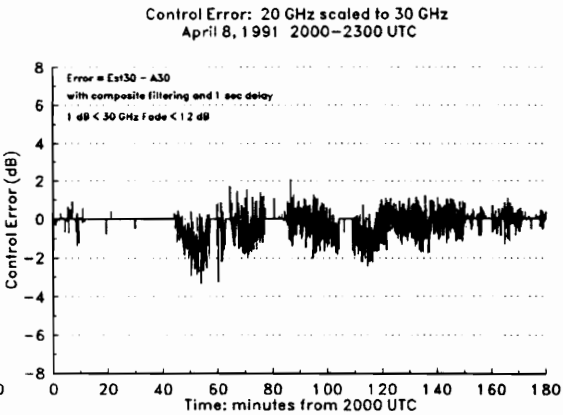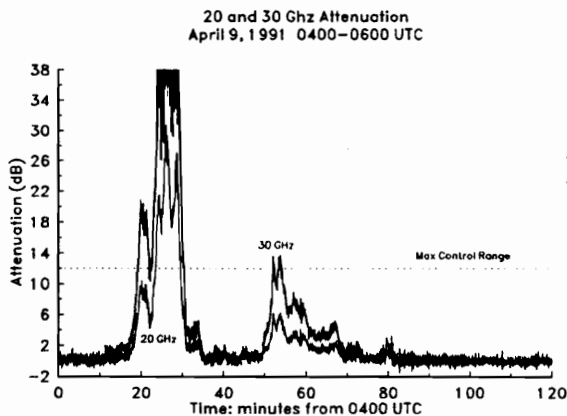

Figure A1.2.19-1

Figure A1.2.19-2

Table A1.2.19: RMS error and optimum scaling factor and filter bandwidth
for April 15, 1991 0800-1000 UTC

Delay sec	RMS Error	Scale Factor	Bandwidth (Hz)
	(dB)	20 GHz CCIR scaled to 30 GHz: scale ratio = 1.97	
0	1.24		
1	1.19		
		20 GHz filtered, scaled to 30 GHz: Composite	
0	1.06		
1	1.11		
5	1.17		
10	1.25		
20	1.41		
		20 GHz filtered, scaled to 30 GHz: Optimum	
0	1.05	1.882676	0.081314
1	1.09	1.846409	0.069489
5	1.14	1.847154	0.085879
10	1.22	1.829473	0.104247
20	1.37	1.804930	0.118902
		30 GHz predicting 30 GHz: Composite	
1	0.48		
5	0.65		
10	0.84		
20	1.13		
		30 GHz predicting 30 GHz: Optimum	
1	0.48	0.997463	0.159223
5	0.63	0.994478	0.242171
10	0.82	0.986136	0.309669
20	1.11	0.957364	0.280638

132

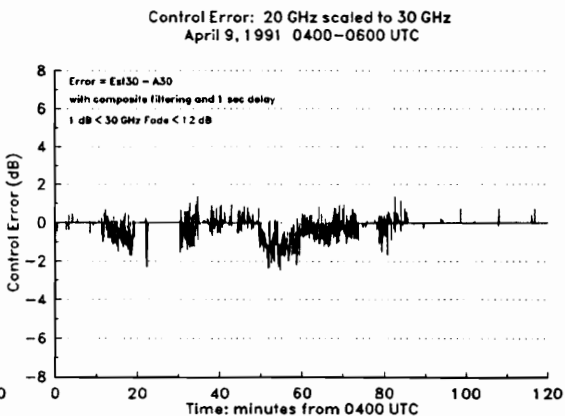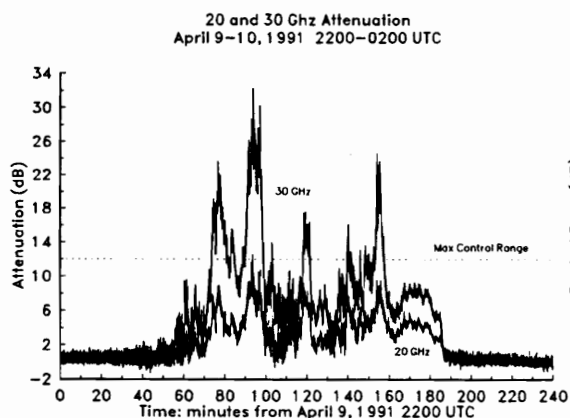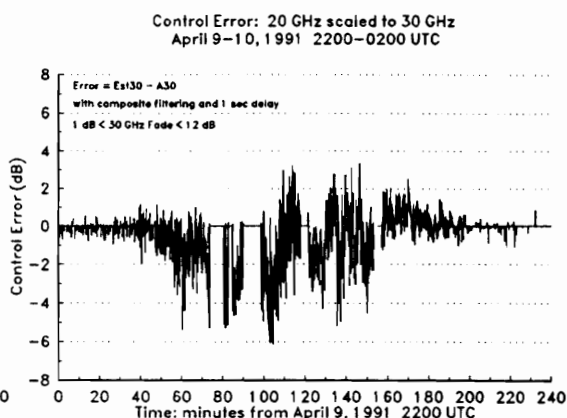## A1.2.20: April 24, 1991 1200-1500 UTC Event

Figure A1.2.20-1

Figure A1.2.20-2

Table A1.2.20: RMS error and optimum scaling factor and filter bandwidth
for April 24, 1991 1200-1500 UTC

Delay sec	RMS Error	Scale Factor	Bandwidth (Hz)
	(dB)	20 GHz CCIR scaled to 30 GHz: scale ratio = 1.97	
0	1.05		
1	0.94		
		20 GHz filtered, scaled to 30 GHz: Composite	
0	0.69		
1	0.75		
5	0.81		
10	0.86		
20	1.00		
		20 GHz filtered, scaled to 30 GHz: Optimum	
0	0.64	2.020728	0.026304
1	0.72	2.018311	0.027411
5	0.79	2.021664	0.031958
10	0.84	2.015440	0.038920
20	0.99	1.985381	0.048394
		30 GHz predicting 30 GHz: Composite	
1	0.69		
5	0.73		
10	0.80		
20	0.99		
		30 GHz predicting 30 GHz: Optimum	
1	0.67	0.998071	0.057633
5	0.73	0.991043	0.075035
10	0.80	0.990921	0.098460
20	0.98	0.983158	0.113593

133

A1.2.21: April 30, 1991 0200-0400 UTC Event

20 and 30 Ghz Attenuation
April 30, 1991 0200-0400 UTC

30 GHz

20 GHz

Max Control Range

Attenuation (dB)

Time: minutes from 0200 UTC

Figure A1.2.21-1

Control Error: 20 GHz scaled to 30 GHz
April 30, 1991 0200-0400 UTC

Error = Est30 − A30
with composite filtering and 1 sec delay
1 dB < 30 GHz Fade < 12 dB

Control Error (dB)

Time: minutes from 0200 UTC
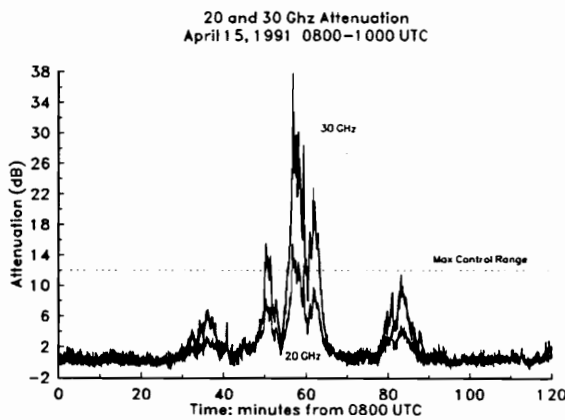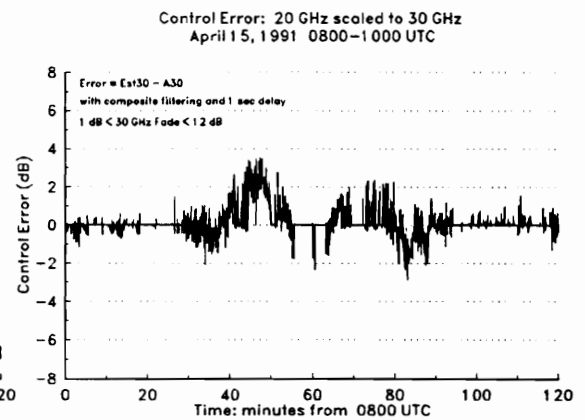
Figure A1.2.21-2

Table A1.2.21; RMS error and optimum scaling factor and filter bandwidth
for April 30, 1991 0200-0400 UTC

Delay sec	RMS Error	Scale Factor	Bandwidth (Hz)
	(dB)	20 GHz CCIR scaled to 30 GHz: scale ratio = 1.97	
0	1.99		
1	1.95		
		20 GHz filtered, scaled to 30 GHz: Composite	
0	1.82		
1	1.84		
5	1.85		
10	1.87		
20	1.92		
		20 GHz filtered, scaled to 30 GHz: Optimum	
0	1.16	1.549659	0.125247
1	1.17	1.546924	0.482425
5	1.21	1.526129	0.088804
10	1.24	1.522657	0.095536
20	1.30	1.517782	0.097725
		30 GHz predicting 30 GHz: Composite	
1	0.35		
5	0.38		
10	0.42		
20	0.51		
		30 GHz predicting 30 GHz: Optimum	
1	0.34	0.999597	0.061929
5	0.38	0.998761	0.064911
10	0.42	0.998057	0.078703
20	0.51	0.995033	0.090985

134

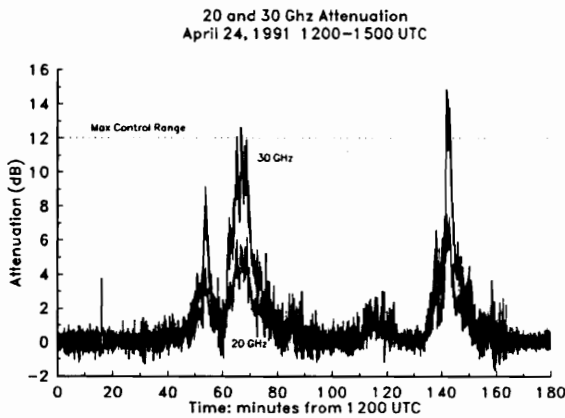## A1.2.22: May 6, 1991 1700-1900 UTC Event
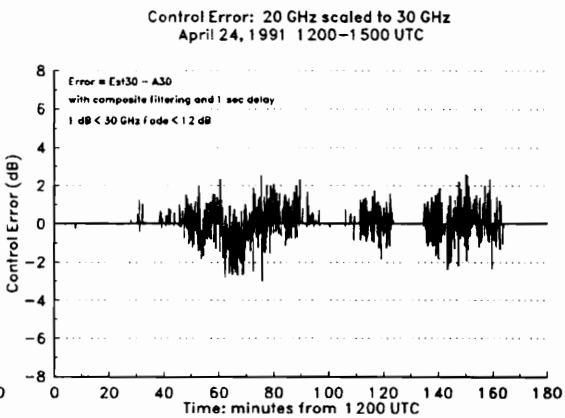

Figure A1.2.22-1

Figure A1.2.22-2

Table A1.2.22: RMS error and optimum scaling factor and filter bandwidth
for May 6, 1991 1700-1900 UTC

Delay sec	RMS Error	Scale Factor	Bandwidth (Hz)
	(dB)	20 GHz CCIR scaled to 30 GHz: scale ratio = 1.97	
0	1.83		
1	1.51		
		20 GHz filtered, scaled to 30 GHz: Composite	
0	1.03		
1	1.02		
5	1.09		
10	1.14		
20	1.29		
		20 GHz filtered, scaled to 30 GHz: Optimum	
0	1.02	2.004954	0.021520
1	1.00	1.983632	0.018609
5	1.10	2.016757	0.016541
10	1.13	1.954755	0.029968
20	1.33	2.041422	0.019383
		30 GHz predicting 30 GHz: Composite	
1	1.18		
5	1.21		
10	1.25		
20	1.39		
		30 GHz predicting 30 GHz: Optimum	
1	1.16	0.999839	0.052947
5	1.21	1.000534	0.062576
10	1.26	1.000192	0.073632
20	1.39	0.996303	0.092416

135

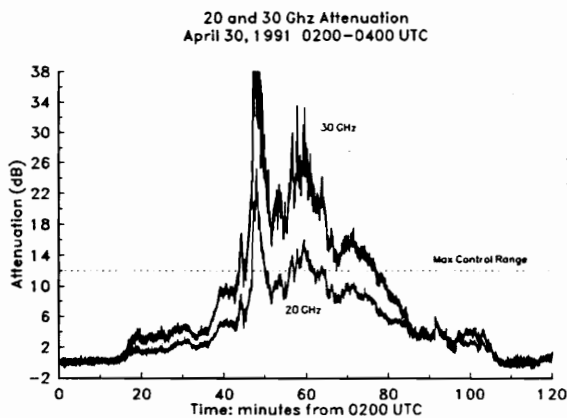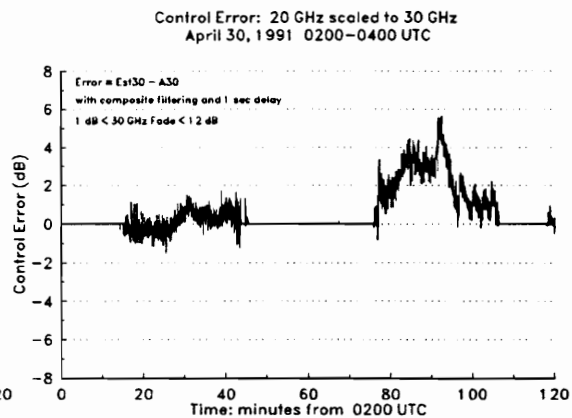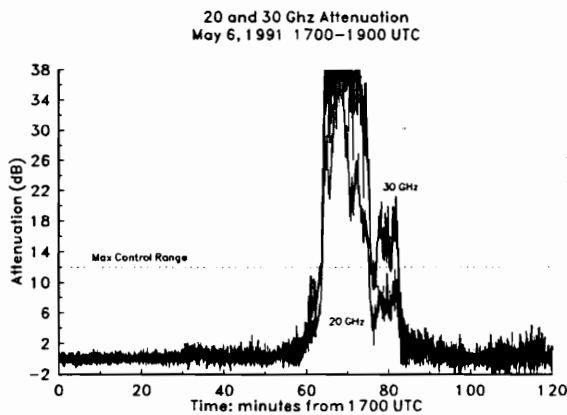## A1.2.23: May 12, 1991 1900-2200 UTC Event

Figure A1.2.23-1

Figure A1.2.23-2

Table A1.2.23: RMS error and optimum scaling factor and filter bandwidth
for May 12, 1991 1900-2200 UTC

Delay sec	RMS Error	Scale Factor	Bandwidth (Hz)
	(dB)	20 GHz CCIR scaled to 30 GHz: scale ratio = 1.97	
0	1.79		
1	1.74		
		20 GHz filtered, scaled to 30 GHz: Composite	
0	1.58		
1	1.57		
5	1.58		
10	1.63		
20	1.69		
		20 GHz filtered, scaled to 30 GHz: Optimum	
0	1.49	2.034110	0.011845
1	1.48	2.039333	0.014106
5	1.51	2.012717	0.009681
10	1.54	2.010512	0.009991
20	1.59	2.013772	0.012707
		30 GHz predicting 30 GHz: Composite	
1	0.61		
5	0.74		
10	0.78		
20	0.88		
		30 GHz predicting 30 GHz: Optimum	
1	0.61	0.998782	0.066522
5	0.71	0.998742	0.028002
10	0.75	0.998394	0.032635
20	0.85	0.996811	0.035735

A1.2.24: May 14, 1991 2000-2200 UTC Event

20 and 30 Ghz Attenuation
May 14, 1991 2000-2200 UTC

Figure A1.2.24-1

Control Error: 20 GHz scaled to 30 GHz
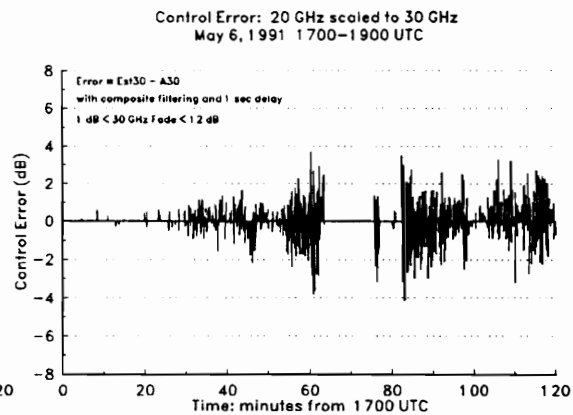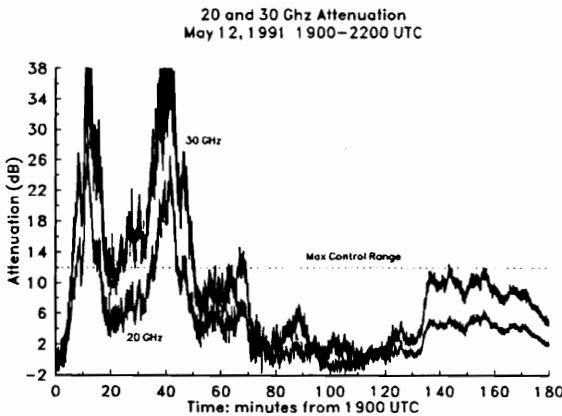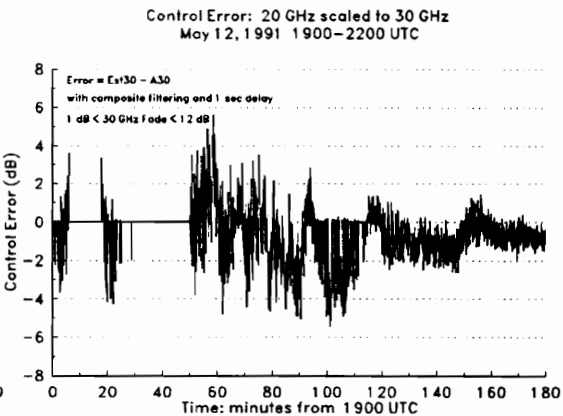May 14, 1991 2000-2200 UTC

Figure A1.2.24-2

Table A1.2.24: RMS error and optimum scaling factor and filter bandwidth
for May 14, 1991 2000-2200 UTC

Delay sec	RMS Error	Scale Factor	Bandwidth (Hz)
	(dB)	20 GHz CCIR scaled to 30 GHz: scale ratio = 1.97	
0	1.54		
1	1.50		
		20 GHz filtered, scaled to 30 GHz: Composite	
0	1.23		
1	1.24		
5	1.16		
10	1.17		
20	1.23		
		20 GHz filtered, scaled to 30 GHz: Optimum	
0	1.02	2.104737	0.006233
1	0.98	2.106360	0.006395
5	0.97	2.093754	0.006379
10	0.97	2.090248	0.006668
20	1.02	2.082350	0.007097
		30 GHz predicting 30 GHz: Composite	
1	0.74		
5	1.01		
10	1.03		
20	1.06		
		30 GHz predicting 30 GHz: Optimum	
1	0.74	0.9904763	0.072622
5	0.93	0.9941586	0.012176
10	0.95	0.9925211	0.013833
20	0.98	0.9925097	0.013732

137

A1.2.25: May 19, 1991 1300-1600 UTC Event

20 and 30 Ghz Attenuation
May 19, 1991 1300-1600 UTC

Figure A1.2.25-1

Control Error: 20 GHz scaled to 30 GHz
May 19, 1991 1300-1600 UTC

Figure A1.2.25-2

Table A1.2.25: RMS error and optimum scaling factor and filter bandwidth
for May 19, 1991 1300-1600 UTC

Delay sec	RMS Error	Scale Factor	Bandwidth (Hz)
	(dB)	20 GHz CCIR scaled to 30 GHz: scale ratio = 1.97	
0	0.92		
1	0.91		
		20 GHz filtered, scaled to 30 GHz: Composite	
0	0.97		
1	0.96		
5	0.99		
10	1.00		
20	1.02		
		20 GHz filtered, scaled to 30 GHz: Optimum	
0	0.33	2.358865	0.021220
1	0.33	2.360562	0.023334
5	0.36	2.357745	0.019543
10	0.39	2.356849	0.018263
20	0.43	2.347802	0.019595
		30 GHz predicting 30 GHz: Composite	
1	0.20		
5	0.26		
10	0.27		
20	0.31		
		30 GHz predicting 30 GHz: Optimum	
1	0.20	0.999520	0.318695
5	0.25	0.999440	0.032631
10	0.27	0.998828	0.037965
20	0.31	0.998586	0.051516

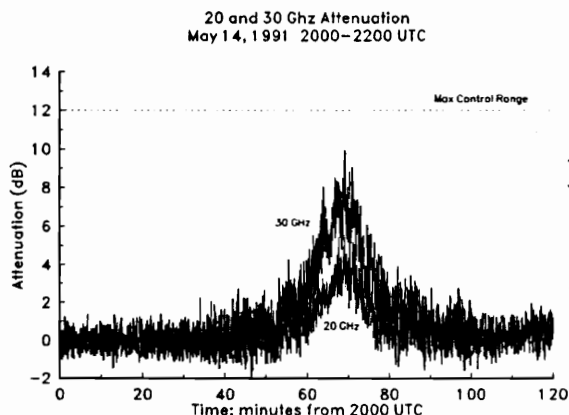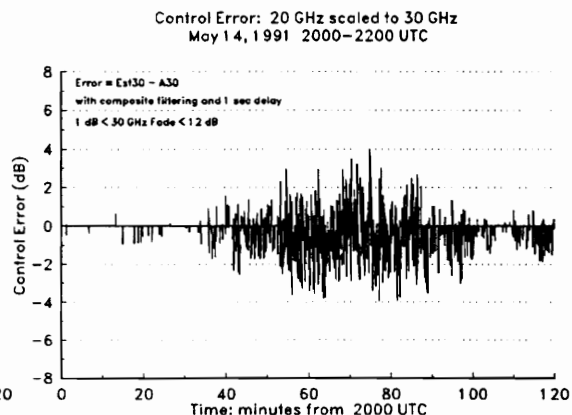138

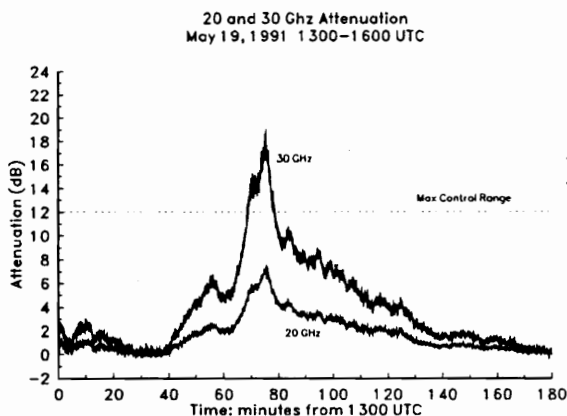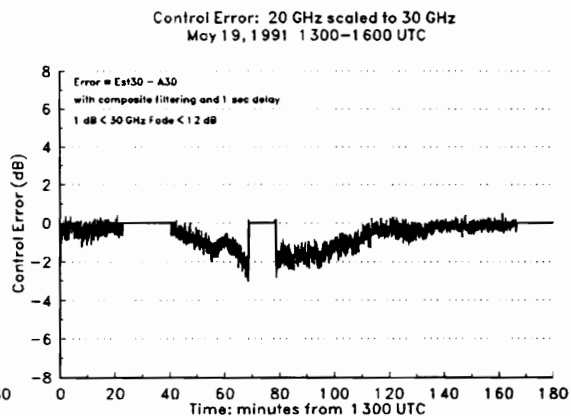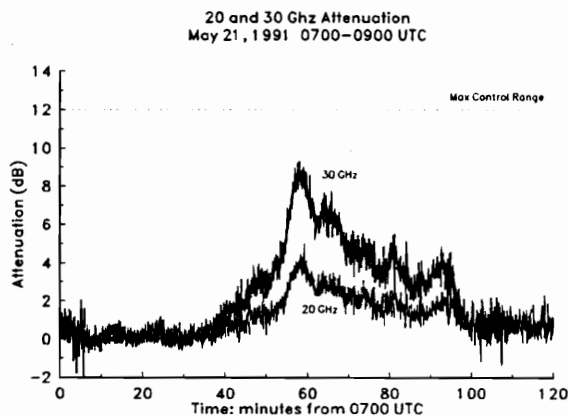## A1.2.26: May 21, 1991 0700-0900 UTC Event

Figure A1.2.26-1
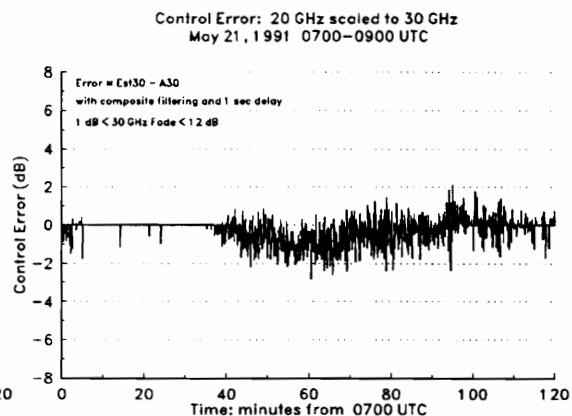
Figure A1.2.26-2

Table A1.2.26: RMS error and optimum scaling factor and filter bandwidth
for May 26, 1991 0700-0900 UTC

Delay sec	RMS Error (dB)	Scale Factor	Bandwidth (Hz)
		20 GHz CCIR scaled to 30 GHz: scale ratio = 1.97	
0	0.83		
1	0.83		
		20 GHz filtered, scaled to 30 GHz: Composite	
0	0.79		
1	0.81		
5	0.83		
10	0.87		
20	0.92		
		20 GHz filtered, scaled to 30 GHz: Optimum	
0	0.53	2.206220	0.012139
1	0.54	2.206642	0.011757
5	0.59	2.204098	0.0104638
10	0.62	2.202773	0.0101520
20	0.67	2.198540	0.0109752
		30 GHz predicting 30 GHz: Composite	
1	0.33		
5	0.52		
10	0.53		
20	0.55		
		30 GHz predicting 30 GHz: Optimum	
1	0.28	0.998172	1.5233618
5	0.47	0.998591	0.0131858
10	0.48	0.997538	0.0162827
20	0.50	0.997385	0.0196136

139

APPENDIX 2: NEURAL NET TEST PROGRAM

A2.1 USERS GUIDE

A2.1-1 Introduction

This appendix contains a listing of the program used to implement the simple neural net described in Section 5.3. The program is written in Turbo Pascal and it was complied and run on a MS-DOS type computer. The program is computationally intense and a math co-processor is recommended particularly if a large number of hidden nodes are used and/or the data files are large. Figure A2.1-1 shows the net implemented and Figure A2.1-2 is a flow diagram for the program.
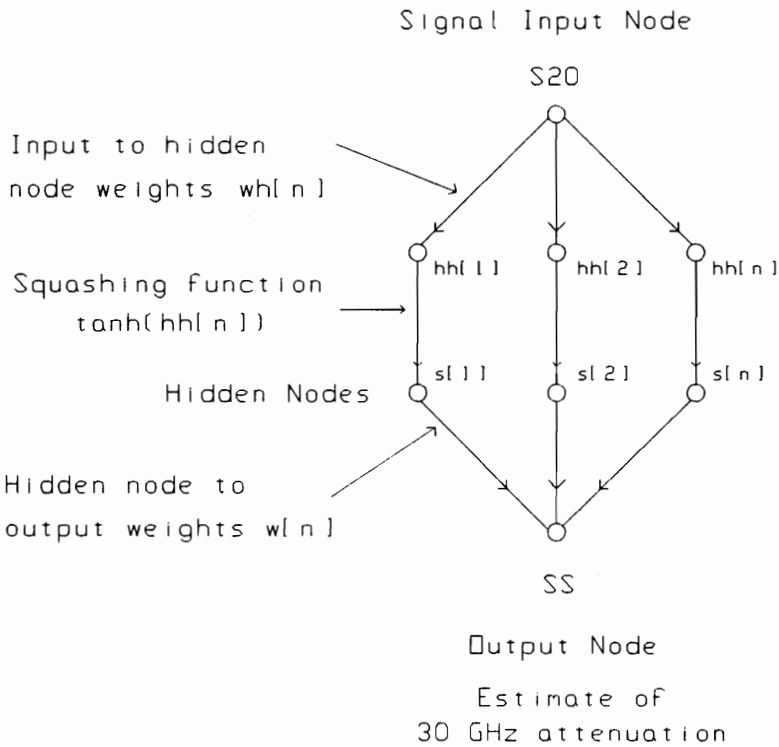

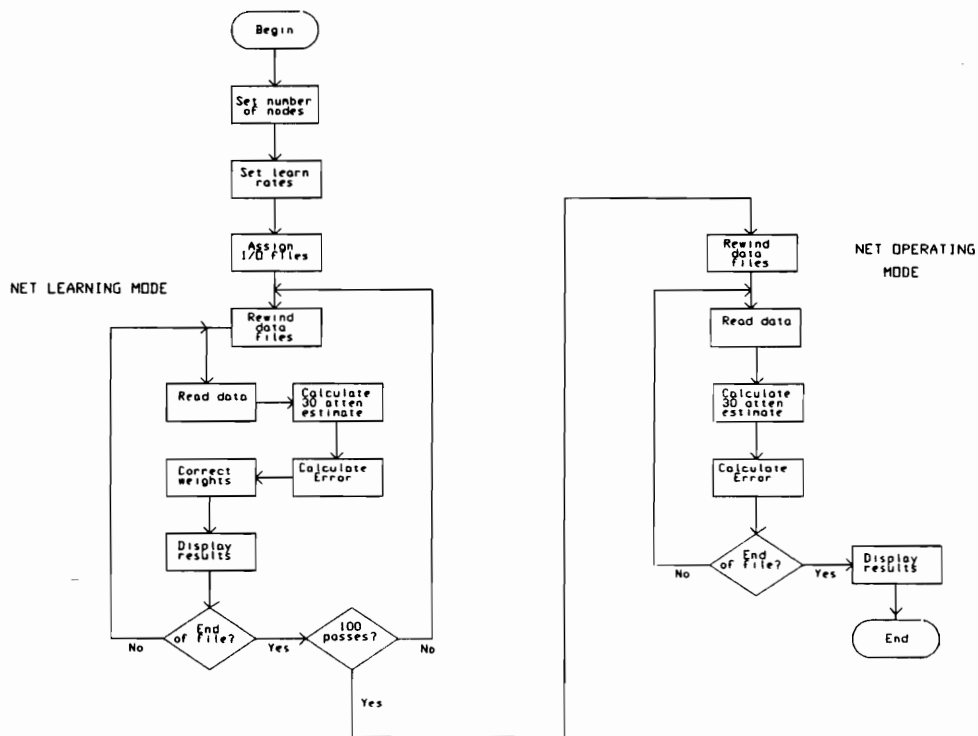Figure A2.1-1: Simple neural net implementation.

Figure A2.1-2: Flow block diagram for neural net program.

A2.1-2 Running the program

In order to run the program it is necessary to specify the number of hidden nodes, *Nhide*, and the learn rates, *LrateH* and *LrateO*. These parameters can be found a few lines below the BEGIN {Begin main program} statement.

Nhide specifies the number of hidden nodes in net. *LrateH* defines the learning rate for the $wh[n]$ weight correction. The wh weights are the gains from the input to the hidden nodes. In order to insure convergence, *LrateH* must be much smaller then *LrateO* which controls the learning rate for the output weights, $w[n]$. *LrateH* and *LrateO* can be found in the program immediately below *Nhide*.

It is necessary to specify two ASCII input files and an ASCII output file. The first input file contains the 20 GHz attenuation data. Its structure is given by (A2.1-1).

Time (real)   20 GHz attenuation (real)   20 GHz radiometer (integer) (A2.1-1)

The second file contains the 30 GHz attenuation data. Its structure is similar and it is given by:

Time (real)   20 GHz attenuation (real)   20 GHz radiometer (integer) (A2.1-2)

The time and attenuation data are real numbers and the radiometer data are integers. The radiometer data are not used in the program. If the program is used for further work it should be modified to accommodate the OLYMPUS data files.

Figure A2.1-3 is a typical program output during the learning mode. The program will display the weights and the hidden node values. The RMS and peak errors after each pass are also displayed. The weights and errors are updated after each pass through the data so the user can monitor convergence.

Figure A2.1-4 is a typical program output during the operating mode. The weights are displayed but not corrected. The RMS and peak error are a measure of net performance.

The output file contains the time, S20, the 20 GHz attenuation, S30, the 30 GHz attenuation, and SS, the net estimate of the 30 GHz attenuation. This file has the form:

Time, S20, S30, SS   (A2.1-3)

The input and output files are defined just below *LrateH* and *LrateO*.

Neural Output: Learning mode

Hidden node weights	0.077	0.079	0.077	0.076

Hidden node output	0.569	0.589	0.571	0.585
squashing f output	0.515	0.529	0.516	0.526

output weights		7.210	6.791	9.381	5.251

Pass # = 100   RMS Error = 0.093   Max Error = 0.215

Figure A2.1-3: Typical screen display when the program is running in the learning mode.

Neural Output: Operating mode

Hidden node weights	0.077	0.076	0.077	0.077
Hidden node output	0.575	0.564	0.574	0.575
squashing f output	0.519	0.511	0.518	0.519
output weights	7.963	5.512	8.507	6.843

RMS Error = 0.415   Max Error = 0.5841

Figure A2.1-4: Typical screen display with the program has finished in the operating mode.

A2.2 PROGRAM LISTING

Program   NonLinearNeuralNetTest ;

{Implements a simple nonlinear neural multi node net as test program }
{created 10/13/91 last edited: 11/11/92 }
var

```
data20,data30            : text[16384] ;   {20/30 GHz attenuation input files}
output                   : text[8192] ;    {output file}
time20,time30            : real ;          {time as read from 20/30 data file}
S20, S30                 : real ;          {20/30 atten as read from data file}
rad20,rad30              : integer ;       {20/30 radiometer (not used) }
wh                       : array [1..10] of real ;   {input to hidden node weights}
w                        : array [1..10] of real ;   {hidden node to output weights}
s                        : array [1..10] of real ;   {S20 * w intermediate values}
hh                       : array [1..10] of real ;   {hh = squashing f(s)}
SS                       : real ;          {SS = net output, 30 GHz attenuation estimate}
Error, Temp              : real ;          {Error = SS - Actual value of 30}
Nhide                    : integer ;       {Number of hidden nodes}
i, j, m, n               : integer ;       {counter indexes}
LrateH, LrateO           : real ;          {Learning rate hidden/output nodes}
SqSumError               : real ;          {Sum of squared error}

Function tanh(x:real) : real ;      {squashing function}
var temp : real ;
begin
 temp := exp(2.0 * x) ;
 tanh := (temp - 1.0) / (temp + 1.0) ;
end ;

Function sech(x:real) : real ;
begin
 sech := 2.0 / (exp(x) + exp(-x)) ;
end ;

Procedure Initialize ;
begin
 SqSumError := 0.0 ;  n := 0 ; Temp := 0.0 ;
 for j := 1 to Nhide do
 begin
    w[j] := random * 5.0 ;        {Initialize weights with random numbers}
    wh[j] := random * 0.1 ;
 end ;
 writeln('Neural Output: Learning mode') ;
 gotoxy(1,5) ; writeln('Hidden node weights') ;
 gotoxy(1,8) ; writeln('Hidden node output') ;
 gotoxy(1,9) ; writeln('squashing f output') ;
 gotoxy(1,11) ; writeln('output weights') ;
 writeln ;
end ;
```

```
Procedure Display ;   {write the weights and node values on the screen}
begin
  for j := 0 to Nhide-1 do
  begin
     gotoxy((j*7+22),5) ;  write(wh[j+1]:5:3) ;
     gotoxy((j*7+22),8) ;  write(hh[j+1]:5:3) ;
     gotoxy((j*7+22),9) ;  write(s[j+1]:5:3) ;
     gotoxy((j*7+22),11) ; write(w[j+1]:5:3) ;
  end ;
  writeln ;
end ;

BEGIN  {Begin main program}

clrscr ;
initialize ;

Nhide := 4 ;          {Set the number of hidden nodes}
LrateH := 0.00005 ;    {Learning rate for hidden nodes}
LrateO := 0.1 ;        {Learning rate for output nodes}
Assign(data20, '\turbo\net\testdat.20');      {Assign the data files to}
Assign(data30, '\turbo\net\testdat.30');      {actual files}
Assign(output, '\turbo\net\net2.txt') ;       {output file name}

{Teach the net}

for m := 1 to 100 do
begin
  Temp := 0.0 ; SqSumError := 0.0 ; n := 0 ;
  Reset(data20); Reset(data30);               {start from file beginning}


  Repeat
     read(data20,time20,S20,rad20) ;  {read time, atten, and radiometer data from 20}
     read(data30,time30,S30,rad30) ;  {read time, atten, and radiometer data from 30}
     SS := 0.0 ;                 {Begin with output estimate = 0}
     for j := 1 to Nhide do
     begin
        hh[j] := wh[j] * S20 ;      {Calculate effect of input on hidden node}
        s[j] := tanh(hh[j]) ;       {Apply nonlinear squashing function}
        SS := SS + w[j] * s[j] ;    {Calculate output from hidden node values}
     end ;
     Error := S30 - SS ;           {Error = Actual 30 - Estimated 30}

     {Correct weights}

     for j := 1 to Nhide do
     begin
        wh[j] := wh[j] + LrateH * Error * w[j] * sqr(sech(hh[j])) * S20 ;
                                                              {Correct hidden node
weights}
        w[j] := w[j] + LrateO * Error * s[j] ;  {Correct output weights}
```

146

```
    end ;

    SqSumError := SqSumError + sqr(Error) ;    {Sum of Error squared}
    if Abs(Error) > Temp then Temp := abs(Error) ;  {Find value of max error}

    n := n + 1 ;      {count the # of passes through the data}

  Until Eof(data20) ;
  Close(data20) ;  Close(data30) ;      {Close the data files}

  display ;                           {display the result of this pass}

  writeln('Pass # = ',m,'   RMS Error = ',sqrt(SqSumError/n):2:3,
          '   Max Error = ',Temp:2:3) ;              {display the error
                                              for this pass}
end ;

{Test the net with the learned values}

Temp := 0.0 ; SqSumError := 0.0 ; n := 0 ;
Reset(data20); Reset(data30);     {start from the beginning of data files}
rewrite(output) ;

Repeat
  read(data20,time20,S20,rad20) ;        {read the data}
  read(data30,time30,S30,rad30) ;
  SS := 0.0 ;
  for j := 1 to Nhide do
  begin
     s[j]  := tanh(wh[j] * S20) ;
     SS := SS + w[j] * s[j] ; {Calculate effect of hidden nodes on output}
  end ;
  Error := S30 - SS ;        {Target - Calculated}
  SqSumError := SqSumError + sqr(Error) ;
  if Abs(Error) > Temp then Temp := abs(Error) ;
  writeln(output,time20:3:3,' ',S20:3:3,' ',S30:3:3,' ',SS:3:3) ; {write results to a file}
   n := n+ 1 ;
Until Eof(data20) ;

Close(data20) ;  Close(data30) ;
close(output) ;

gotoxy(1,1); writeln('Neural Net Output: Operating mode') ;  {display results}
display ;                                   {from operating mode}

writeln('              RMS Error = ',sqrt(SqSumError/n):2:3,
                      '   Max Error = ',Temp:2:3) ;
END.  {End main program}
```
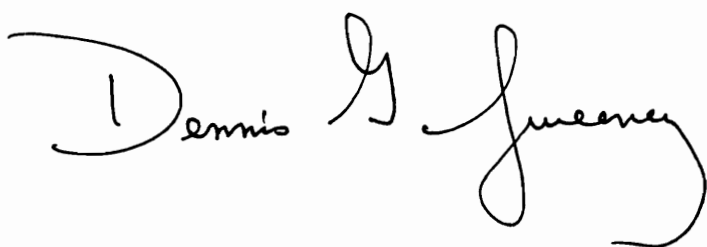
VITA

Dennis G. Sweeney is a native of Syracuse, New York who came to Lynchburg, Virginia in 1959. He obtained a Bachelor of Science in Electrical Engineering from Virginia Tech in 1971. His work experience includes a co-op experience with General Electric in Lynchburg, VA and experience as a research assistant at the National Radio Astronomy Observatory in Greenbank, WV. After graduation, he prepared for the Roman Catholic ministry, obtaining a Master of Arts in Religious Studies from Catholic University of America in Washington, DC in 1976. He served in a number of parish assignments until 1984 when he returned to Virginia Tech to pursue advanced studies in Electrical Engineering. He was awarded the M.S.E.E. degree in 1986. While at Tech he worked with the Satellite Communications Group on projects involving satellite slant path propagation at 12.5, 20, and 30 GHz. He designed and built receiving equipment for the 12.5, 20, and 30 GHz OLYMPUS satellite beacons, and he was involved in the design of the ACTS propagation terminal. He also taught undergraduate and graduate radio engineering courses at Va Tech. His research interests include satellite systems, radio propagation, and radio frequency and microwave hardware design. He successfully completed the requirements for the Ph.D. in Electrical Engineering in January of 1993.